Modelling illumination and resolution effects in seismic with a 2(3)D convolution method

by
Thomas Jarle Grimstad

Master of Science Thesis

Department of Earth Science
University of Bergen

November 20, 2018

Abstract

The aim of seismic modelling is to generate modelling cases with the highest degree of realism possible, where the benchmark is the expensive (expertise needed, extensive time-cost) finite-difference modelling method. A popular alternative is the much more efficient and simpler convolution modelling, where the standard is the 1D convolution method. However, this method only accounts for vertical resolution effects at best. Another alternative is a 2(3)D convolution modelling method, which estimates Point-Spread Functions (PSF) used to simulate a full 3D resolution and illumination effects in seismic imaging.

In this study, the main objective is to examine the effects that lateral resolution and limited illumination have on 2(3)D prestack depth-migrated seismic images using the PSF-based 2(3)D convolution method. Four modelling cases were considered; a steep wedge model, two outcrop models (Franklin Mountains, USA and Beckwith Plateau, USA), and finally a 3D reservoir model from an actual cave, Setergrotta (Norway), as a proxy for a paleokarst reservoir.

The results of the modelling cases revealed a relation between the vertical and lateral (horizontal) resolution, in addition to significant improvements in the modelled seismic after introducing lateral resolution and illumination effects. These effects caused a smoother and more realistic seismic than the 1D convolution, which struggled with complex structures. The differences were especially noticeable at the 3D Setergrotta model, where the lack of lateral resolution effects in the 1D convolution results caused highly unrealistic seismic.

Based on the modelling results, my conclusions are that the vertical and lateral resolution effects are not two independent entities, and should thus be modelled together. In addition, the results illustrated that 1D convolution modelling is not a sufficient modelling method in such complex models, and should be replaced with the 2(3)D convolution modelling method.

Acknowledgements

First and foremost, I must thank my main supervisor Isabelle Lecomte for continuous feedback, guidance and discussions during my time working on this thesis. I also express my gratitude towards Bent Ole Ruud and Tina Kaschwich for their feedback.

I would also like to thank NORSAR Innovation AS for the use of academic license to the modelling software SeisRoX and NORSAR-2D, FOPAK research group ("Forecasting of architecture, seismic characteristics and flow behaviour in paleokarst reservoirs") for the Setergrotta model and PhD candidate Kristian Jensen for letting me work with his MATLAB codes. Also, a big thanks to my fellow students during all these years, and especially Martin K. Johansen and Espen Friestad for their models, but most of all the good times!

Contents

Notation

Abbreviations

AI - Acoustic impedance

f - frequency

FOPAK - Forecasting of architecture, seismic characteristics and flow behaviour in paleokarst reservoirs (Project)

FD - Finite Difference

Fr - Fresnel zone

FT - Fourier Transform

GMS - Great McKelligon Sag

$\mathbf{I_{SR}}$ - illumination vector

K - Bulk modulus

$\mathbf{K_{sr}}$ - Scattering wavenumber vector

λ - Wavelength

μ - Shear modulus

$\mathbf{p_R}$ - Slowness vectors for the scattered wavefield

$\mathbf{p_S}$ - Slowness vectors for the incident wavefield

PSDM - Prestack Depth Migration

PSF - Point-Spread Function

45° max-dip PSF - Point-Spread Functions with a 45° maximum illumination range.

Perfect illumination PSF - a Point-Spread Function where all dips, from 0° to 90° are illuminated

r - Receiver point

RB - Ray based

RC - Reflection coefficient

ρ - Density

s - Source point

θ - Incident angle

$\theta_{\mathbf{SR}}$ - The opening angle between -$\mathbf{p_S}$ and $\mathbf{p_R}$

TWT - Two-way time

$\hat{u}_S$ - Unit vector perpendicular to the incident wave front from source s

$\hat{u}_R$ - Unit vector perpendicular to the scattered wave front towards receiver r

V - Velocity

Z - Depth

List of Figures

Chapter 1

Introduction

There are several methods used to model seismic data. The two dominating classes for modelling of 2(3)D geological structures are full-waveform and ray-based methods. However, in some applications such as interpretation, well calibration, seismic inversion, amplitude studies, such as amplitude versus offset (AVO), outcrop modelling, etc, using these methods may be difficult and time-consuming. An alternative to these methods is a simpler modelling called convolution modelling.

The standard and much used convolution modelling method is the 1D convolution modelling, which can predict vertical resolution effects in seismic images, but it can neither predict lateral resolution effects, nor account for lack of illumination. A solution to these limitations may be to use a more recent ray-based (RB) approach which allows extending the convolution approach to modelling of prestack depth migrated (PSDM) images. PSDM imaging is a necessity for proper modelling of complex structures, as it compensates for wave propagation in the overburden, which cannot be modelled with 1D convolution modelling (Lecomte, 2008).

The point spread function (PSF) based 2(3)D convolution method is an efficient modelling method which has more realistic illumination and resolution effects than the standard 1D convolution (Lecomte et al., 2015). Since we are able to model these effects, the 2(3)D convolution method will improve understanding of seismic images in complex areas.

In this thesis, I want to compare 1D convolution methods with the PSF based 2(3)D convolution method, especially studying lateral resolution effects, but also other resolution and illumination effects of seismic imaging. I will also explain and illustrate the modelling method for seismic interpreters who may use this method to generate synthetic seismic from reservoir models, outcrops etc., and its advantages over standard 1D convolution.

The seismic modelling used in this thesis works as a picture editing software in many ways, where we start with a model or a picture as input. Then we choose a filter to alter the features in that input image. In the following example the GNU Image Manipulation Program is used. To relate seismic imaging, I use an edge-detect algorithm to simulate what elastic waves are "detecting", i.e., rapid contrasts of impedance. To add the selective dip effects we have in seismic, where we usually better observe the horizontal layers than vertical, I chose the Sobel filter which covers detectability and partial illumination effects (Sobel and Feldman, 1968). As an example, I have chosen an outcrop from Book Cliffs, Utah, USA.

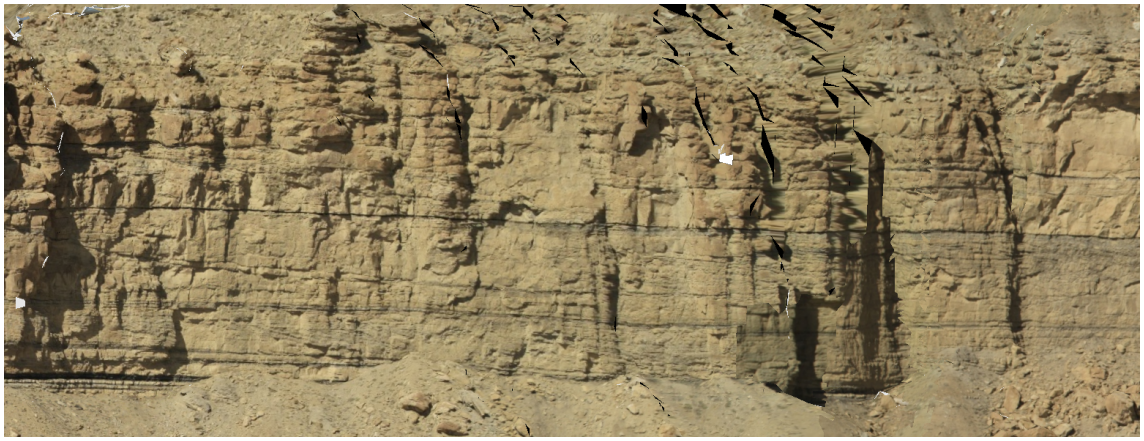

Figure 1.1: *Sedimentary outcrop from the Beckwith Plateu in Book Cliffs, Utah, USA. Approximately 100 m x 50 m. Courtesy of Friestad (2018).*

This geological outcrop shows mudstone, sandstone, silt layers and horizontal coal layers. Since this is only an edge-detect filter it will not have any science behind it, it merely highlights the colour differences, shown in Figure 1.2.

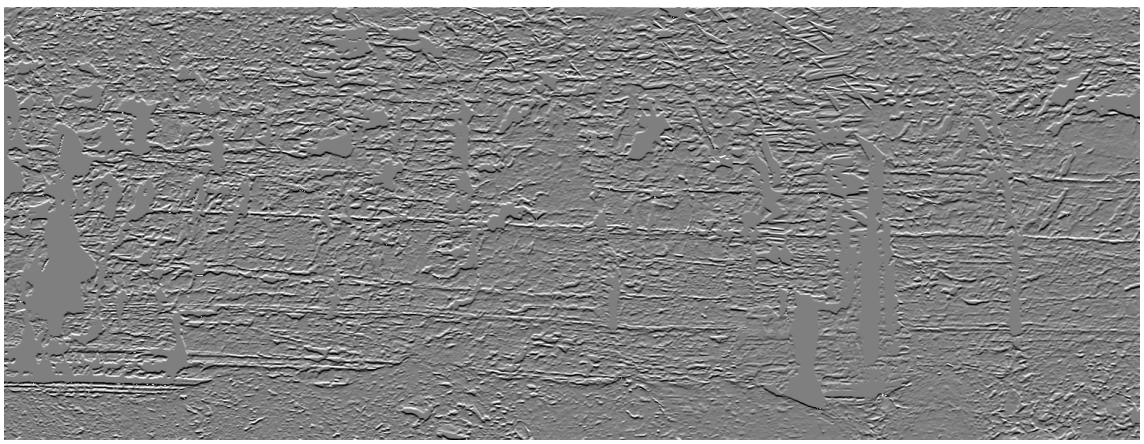

Figure 1.2: *Sedimentary outcrop from Book Cliffs in Utah, USA with horizontal edge-detect filter.*

Figure 1.2 shows the horizontal layers, which in seismic would be the differences in acoustic impedance, only using a quick photo-editing filter. This highlights the boundaries between the channels, and it is possible to observe many lateral wedges, and other geological elements. However, seismic has limited resolution, and the resolution effects is different for vertical and lateral resolution. This can be illustrated by a blurring filter with different degree of blurring laterally and vertically.

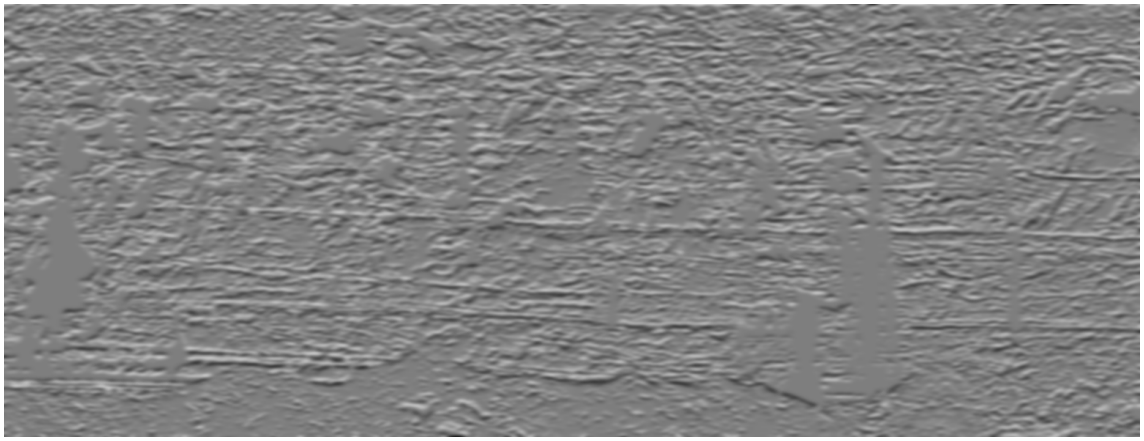

Figure 1.3: *Sedimentary outcrop from Book Cliffs in Utah, USA with added blur.*

In Figure 1.3, I applied a lateral blur twice the value of the vertical. This is analogous to the seismic resolution issue. The difference between this example and the seismic modelling is basically only the filter we use, which is derived from seismic imaging

theory, and the reflectivity used as input. The method presented in this thesis convolves indeed the model with a Point-Spread Function (PSF) to simulate a PSDM image. How to get this PSF will be explained later.

When interpreting a seismic image, we should ideally know which "filter" generated that image. For instance a low frequency filter will yield an image with poor resolution, i.e., blurry boundaries, as illustrated in Figure 1.3. This will complicate the interpretation. We will also illustrate the differences partial illumination makes.

In short the modelling method I will look into starts with a background velocity model, which we use to generate PSFs. These will be convolved with the reflectivity target to give a resulting seismic image. Understanding this process and the effects of the PSF will help seismic interpreters when interpreting real geological models, or to generate synthetic seismic.

Chapter 2

Theoretical background

Seismic modelling is used to simulate elastic wave propagation in Earth models, either by generating prestack data, i.e., synthetic seismograms, to be then used in processing and imaging, or to directly model seismic images. This can be used to understand wave propagation in the subsurface and gives insight to how geological structures are imaged by seismic, which can be, e.g., used to validate seismic interpretation (Lecomte et al., 2015).

The approaches to seismic modelling are classified into three different categories: direct methods, integral-equation methods and ray-tracing methods (Carcione et al., 2002). The direct methods are also known as full-wavefield methods, and use numerical solutions to the wave equation, making it very time- and computer memory-consuming. However, it is often considered the most realistic of the three categories in 2(3)D varying models, making it the benchmark for seismic modelling in such cases.

Integral-equation methods will not be discussed in this thesis, but in short, the methods are based on Huygens' principle, and are more restrictive than the direct methods (Carcione et al., 2002).

RB methods are suitable alternatives in many situations. These methods use high-frequency approximations of the wave equation. The resulting synthetic seismograms include wave phases selected by the user, but in a complex, detailed subsurface, a standard RB modelling will not be adequate because it requires smooth interfaces and property fields (Lecomte et al., 2015).

Convolution modelling is a simpler method. 1D convolution has been used for several decades, and it is still the standard approach in well calibration, AVO, seismic inversion etc. However, 1D convolution is limited, as it can neither predict lateral resolution issues nor lack of illumination, because it does not consider acquisition

survey geometry and an overburden model (Lecomte et al., 2015).

The method we will focus on in this thesis obtains rapid modelling results using RB modelling with convolution approaches, using the PSF as generated from RB data, making it possible to simulate 2(3)D PSDM images at a cost similar to 1D convolution (Lecomte, 2008).

The first step in this method is to obtain the illumination vectors. An illumination vector shows the illumination at a given reference point, i.e., where to calculate the PSF, and we obtain several illumination vectors for a single survey (Lecomte, 2008), this is done using a smooth background velocity model. The illumination vector is then multiplied with the frequency of a chosen wavelet, resulting in the scattering wavenumber vectors.

Mapping all the scattering wavenumber vectors in the wavenumber domain gives us the PSDM filter. A Fourier transform of the PSDM filter from the wavenumber domain to the corresponding space domain gives us the PSF, which is used as estimates of 3D spatial prestack convolution operators. These are convolved with detailed 3D reflectivity models to generate PSDM images (Lecomte et al., 2015).

This method uses different geophysical and mathematical principles, so to fully understand the method I will explain and illustrate some of the key concepts such as rays, slowness vectors, resolution, detectability, Fourier transform, PSDM images and convolution in the following paragraphs.

2.1 Seismic rays

This method simplifies the wave propagation in the subsurface by using the concept of seismic rays. These rays are defined as lines of seismic energy (ray paths). In isotropic media, these rays are perpendicular to the wavefronts (Červený et al., 1977).

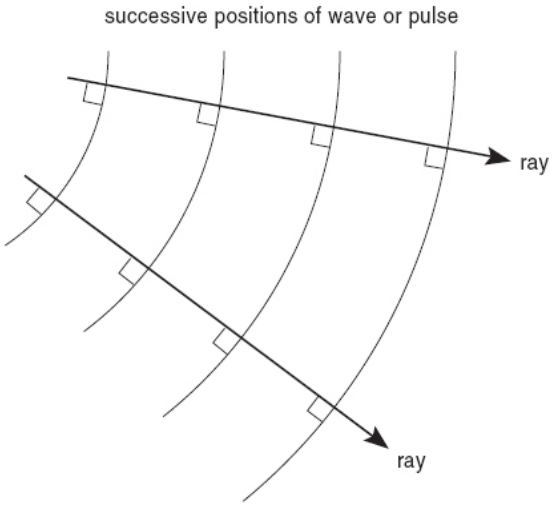

Figure 2.1: *The relation between rays and wavefronts in an isotropic media. Figure from (Mussett et al., 2000).*

In seismic, the subsurface is mapped using the transmitted and reflected rays. Therefore, it is important to have an understanding of the way the body waves behaves. There are two types of body waves; compressional, known as P-waves, and shear waves, known as S-waves. The velocities of the waves are controlled by three elastic moduli, the bulk modulus (K), which describes the solids resistance to compression, the shear modulus (μ) is also known as its rigidity, and the density (ρ). The P-wave and S-wave velocities is given by:

$$v_p = \sqrt{\frac{K + \frac{4}{3}\mu}{\rho}} \tag{2.1}$$

$$v_s = \sqrt{\frac{\mu}{\rho}} \tag{2.2}$$

These equations show that the S-velocity will always be lower than the P-velocity. The direction of the rays at a boundary between two rock layers is determined by the properties of the layers. The amount of energy reflected to the surface, and transmitted down is determined by the contrast in a parameter called acoustic impedance, AI, given as a product of the density (ρ) and the wave velocities (v) in the respective layers. A rapid contrast in acoustic impedance will reflect more

energy back to the surface.

$$AI = \rho v \tag{2.3}$$

AI is for normal incidence, otherwise the Vs also matter, as the incident P-wave would generate reflected and transmitted S-waves in addition to the P-waves. To measure the effect the interfaces, have on the wave propagation in the case of normal incidence, we use the reflection coefficient R_0, which is given as a ratio of the amplitudes of the reflected and incident rays, A_1 and A_0:

$$R_0 = \frac{A_1}{A_0} \tag{2.4}$$

This can also be given by a simple case of the Zoeppritz equations as (Zoeppritz, 1919):

$$R_0 = \frac{\rho_2 v_2 - \rho_1 v_1}{\rho_2 v_2 + \rho_1 v_1} \tag{2.5}$$

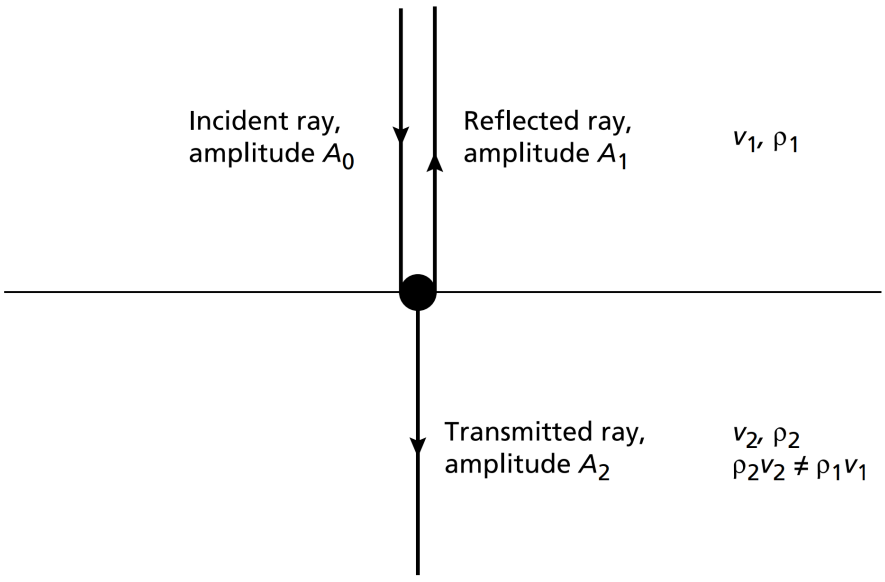

Figure 2.2: *Normal incidence case. Reflected and transmitted rays and the associated amplitudes, velocities and densities at a point of acoustic impedance contrast. Figure from (Kearey et al., 2002).*

In the case of layered media, some of the transmitted waves will become refracted waves. The relation between the angle of incidence and the resulting refracted wave is described by Snell's law:

$$\frac{\sin(\theta_1)}{V_1} = \frac{\sin(\theta_2)}{V_2} \tag{2.6}$$

where θ_1 and θ_2 are the incident and refracted ray angles, and V_1 and V_2 are the velocities for the upper and lower layer, respectively. It should also be noted that an incoming P-wave ray will generate reflected and refracted S-wave rays in addition to the P-wave rays, this partitioning is known as wave conversion. Illustrated by figure 2.3:

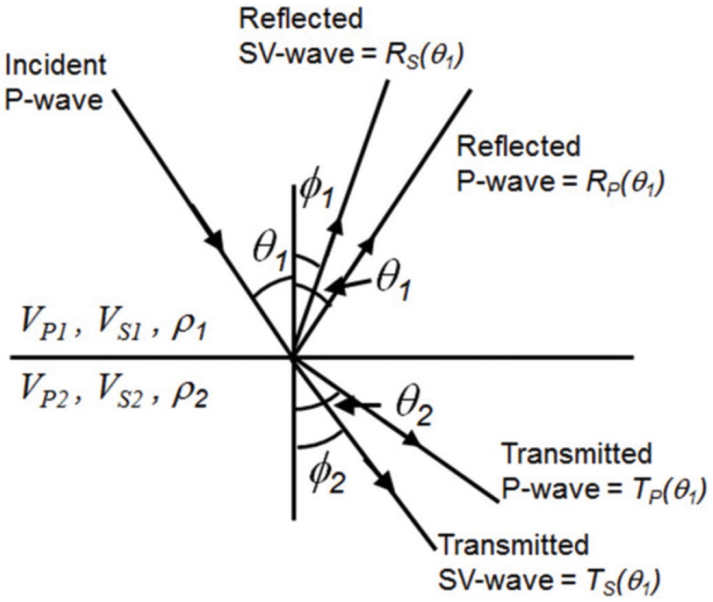

Figure 2.3: *An oblique incident P-wave ray generating reflecting and refracting P- and S-wave rays at a boundary between two elastic layers. Figure from Hampson and Russell (2013).*

The angle of the transmitted rays will increase across the interface with increasing velocity, until we reach the critical angle, i.e., when θ_2 is equal to 90°, where the refracted ray will travel along the interface.

As an example of ray paths, Figure 2.4 shows two generic surveys with a common depth point, with approximately the same geology, except that survey to the right (B) there is a salt dome above the considered point. In such high-velocity events

the ray paths are more bent towards the vertical due to the high velocity in the salt, meaning that they will go in a straighter down and up manner.

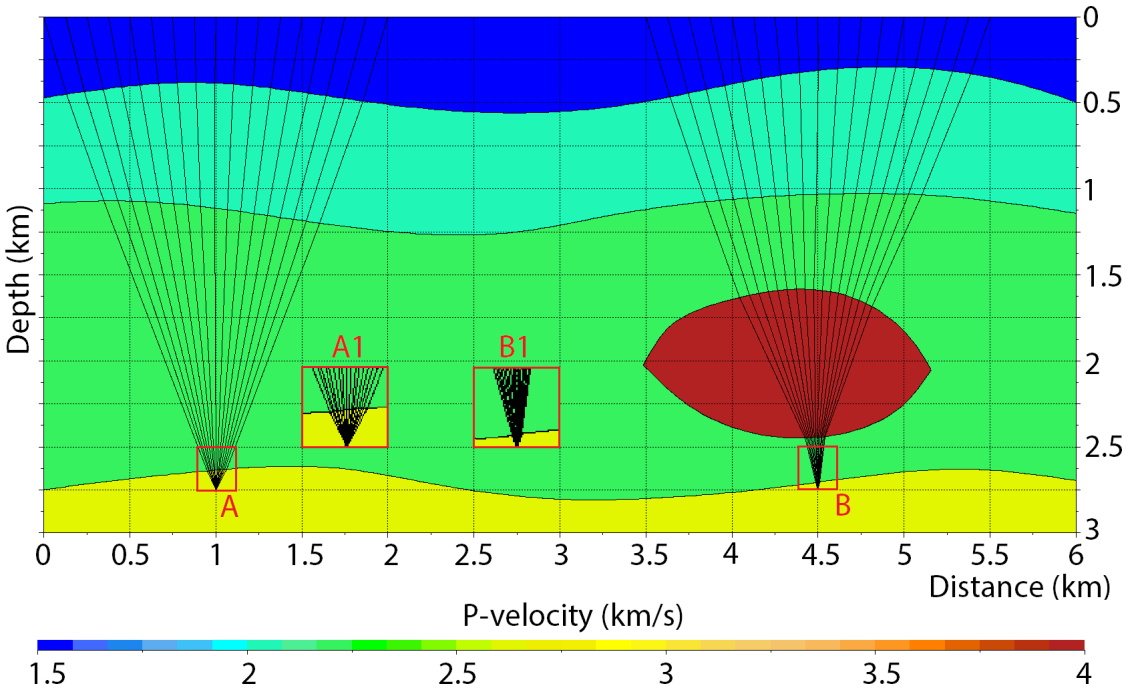

Figure 2.4: *Comparing ray paths at two common depth points. (A) Without a salt dome in the overburden. (B) With a salt dome over. A1 and B1 are zoomed in on A and B, respectively.*

This is what is known as overburden effects, where the seismic signals are altered due to an overburden with different properties than the surrounding area (Fliedner and White, 2003), which is a problem especially in areas with igneous rocks. Other limiting factors in seismic imaging includes attenuation, where the frequencies of the shot in the survey decrease with depth due to absorption and an increase in velocity with depth (Thomson and Hutton, 2004), and the inability to image steep layers (Lecomte et al., 2016).

2.2 Slowness vectors

In chapter 3, the process of obtaining the so-called illumination vectors needed in this method will be discussed, but first it is important to know the theory behind

it. The illumination vector is determined by two slowness vectors, so in this section these slowness vectors will be explained.

As illustrated in Figure 2.5, to generate the illumination vector $\mathbf{I_{SR}}$ at a point in a given background velocity model (e.g., the velocity model used for PSDM), we need two local vectors $\mathbf{p_S}$ and $\mathbf{p_R}$. These are the slowness vectors of the incident and scattered wavefield, respectively, at the considered point called in the following the illumination point. The illumination vector is given as the difference between these vectors Lecomte (2008):

$$\mathbf{I_{SR}} = \mathbf{p_R} - \mathbf{p_S} \tag{2.7}$$

Slowness is per definition the inverse of speed, so it is given as 1/velocity. The slowness vector is the gradient of the wavefront, and by definition will be perpendicular to the wavefront, for both isotropic and anisotropic media. As stated earlier, in isotropic media the seismic rays will also be perpendicular to the wavefronts, and the slowness vectors will thus simply be parallel to the rays, but in anisotropic cases, rays are not necessarily perpendicular to the wavefront. Per definition, the length of the slowness vectors vary with the velocity at the illumination point, i.e., the higher velocity, the shorter the slowness vector is.

Assuming an isotropic velocity model, to simplify, and that there is no wave conversion, both slowness vectors will have the same length because they are attached to the same velocity, but they will have different directions depending on the direction of the corresponding wavefronts (incident or scattered; Figure 2.5). Due to the direction of the wavefronts, the vector $\mathbf{p_R}$ has a positive direction towards the receiver, while the vector $\mathbf{p_S}$ continues downward trough the reflection point. Therefore, the opening angle is between $\mathbf{-p_S}$ and $\mathbf{p_R}$.

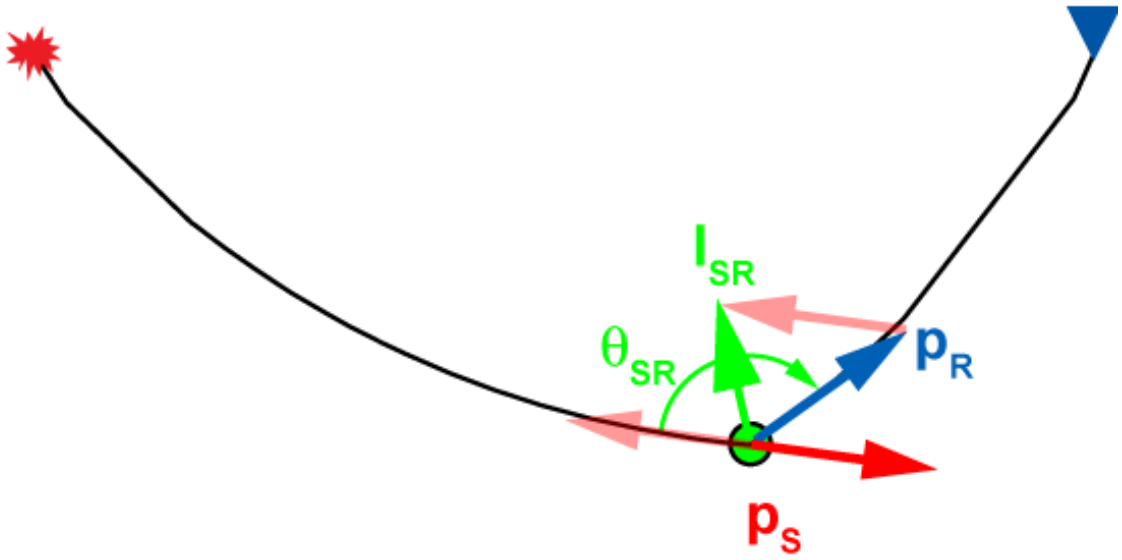

Figure 2.5: *Figure from Lecomte (2008) depicting how the illumination vector at a selected illumination point (green dot) is given by its slowness vectors, where we add the inverse of* $\boldsymbol{p_S}$ *to* $\boldsymbol{p_R}$*.* $\boldsymbol{\theta_{SR}}$ *is the opening angle.*

2.3 Resolution

Resolution is, by definition, the ability to separate two features that are close together (Sheriff, 2002). It is divided into vertical and lateral (or horizontal) resolution, where vertical resolution is generally seen as the most important. The lateral resolution is described by the Fresnel zone, while the vertical resolution is defined as the tuning thickness, which is given as a quarter of the wavelength (Widess, 1973).

2.3.1 Vertical resolution

(Widess, 1973) described the maximum constructive interference from the two reflectors for a case with different polarities to be when the bed thickness is equal to a quarter of the dominant wavelength:

$$tuning\,thickness = \lambda/4 \tag{2.8}$$

The tuning thickness is often illustrated by the wedge model, e.g., Kallweit and Wood (1982). The purpose of this model is to illustrate the wavelet change when

two reflectors are too close together to separate. The effects are different depending on the polarity reflections.

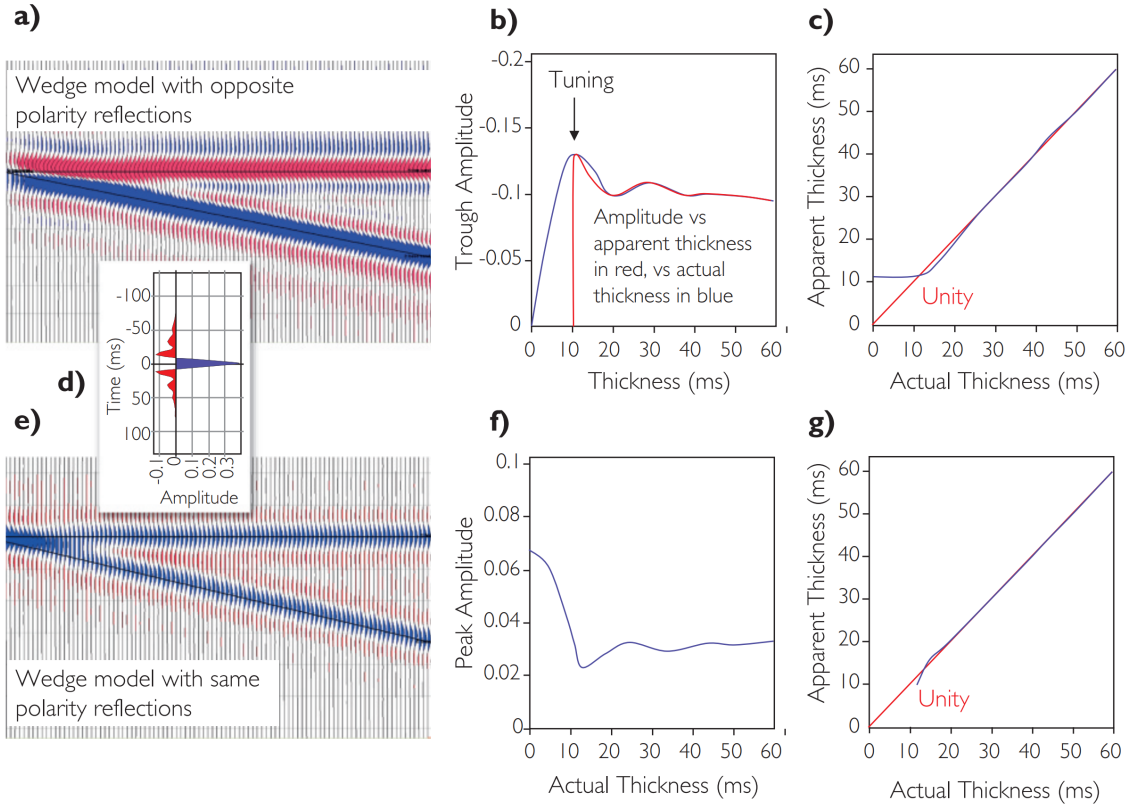

Figure 2.6: *Two wedge models with (a) opposite polarity reflections, and (b) same polarity reflections with thickness and amplitude characteristics. Generated using the seismic wavelet given in (d). Figure from (Simm and Bacon, 2014).*

Figure 2.6 (a)-(c) shows the thickness and amplitude effects of a wedge model with opposite polarity reflections. Below the tuning thickness, the apparent thickness will be significantly lower than the actual thickness.

Figure 2.6 (e)-(g), on the other hand, illustrates the case if the two reflectors are of the same polarity, and the seismic will have an apparent thickness of zero below the tuning thickness Widess (1973). The waveform will not change, and the amplitudes decreases when the thickness decreases. This is until we reach the tuning thickness where the apparent thickness and the actual thickness will align, and it will be possible to observe the two different events.

2.3.2 Lateral resolution

The lateral resolution is determined by the Fresnel zone, illustrated by figure 2.7, a zero-offset survey is conducted, where we have to wave fronts, with the length of each one illustrated by rays with length Z and Z+$\lambda/4$. The Fresnel zone is the width of the reflector which will be reflected as one event, without being able to differentiate between the events inside, because the reflected waves will interfere and add together to become one singular event.

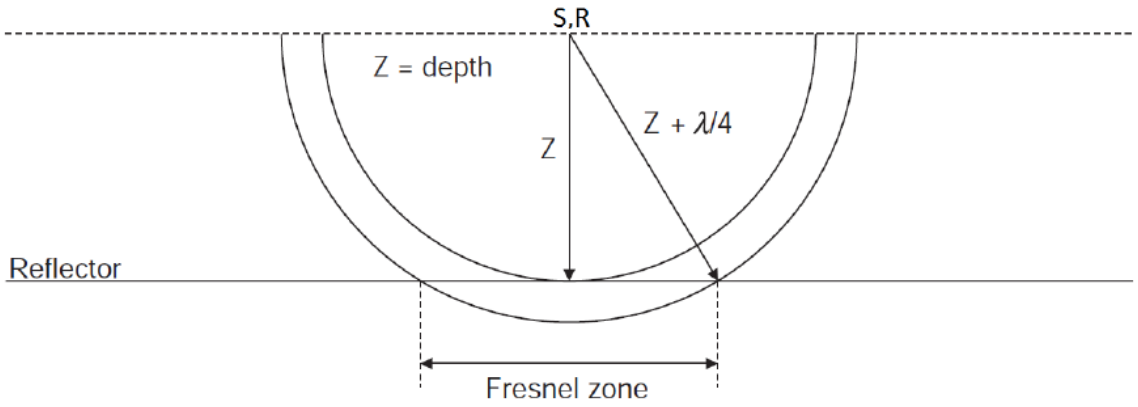

Figure 2.7: *Illustration of the Fresnel zone where Z is the depth, λ is the dominant wavelength. Figure from Herron (2011), modified by (Flesland, 2017).*

The length of the second wave front is Z+$\lambda/4$ because a quarter of a wavelength is the point where the energy from the centre of the reflector transitions from constructive to destructive for the wave (Lindsey, 1989).

The Fresnel zone is given by

$$Fr = \frac{V}{2}\sqrt{\frac{TWT}{f}} \tag{2.9}$$

Where TWT is the two-way time, V is the velocity, and frequency is denoted by f (Sheriff, 2002). Reflectivity changes in a distance less than the Fresnel zone will not be observable (Lindsey, 1989), meaning that the lateral resolving power of a seismic method is determined by the area of its Fresnel zone, which should be as small as possible. In other words, two events at the same depth on a reflectivity line must be separated by, at a minimum, the length of the Fresnel radius to be observable as two independent events. In the subsurface, the velocity of the rocks and the two-way

time will increase with depth, and the frequency will decrease, causing the lateral resolution to decrease.

Migration is the process to improve the spatial resolution, as it is able to shrink the Fresnel zone (Lindsey, 1989). Figure 2.8 illustrates how the Fresnel zone is affected by migration. Before migration the Fresnel zone is shaped as a circle defined by the Fresnel radius. Using 2D migration, it is collapsed to an ellipsoidal shape, with shrinkage only in the direction of the profile, while 3D migration shrinks further the Fresnel zone to a small circle, with a resolution of $\lambda/2$.

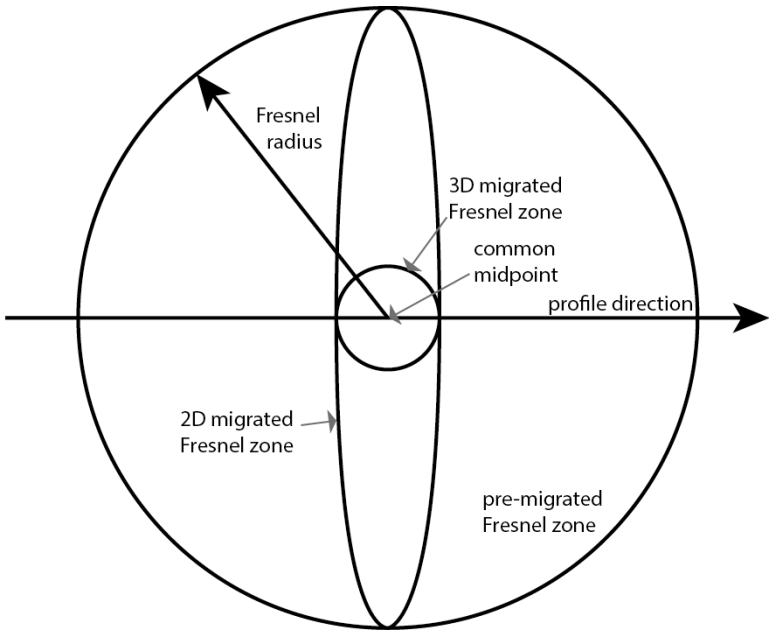

Figure 2.8: *The effect migration has on the Fresnel zone for a survey as seen from above, modified from Lindsey (1989).*

In this thesis, the differences in vertical and lateral resolution for 1D and 2(3)D convolution, will be especially studied. When studying resolution, it is important to know the difference between an event being observable due to the resolution of the seismic, or if the reflection is detectable due to high amplitudes.

2.4 Detectability

Since the reflections from thin layers are not restricted to low amplitudes (Widess, 1973), it is possible to detect layers with a thickness below the tuning thickness

when the layer has higher amplitudes than the background. The detectability of a layer is essentially determined by the acoustic impedance and the signal-to-noise ratio of the seismic (Simm and Bacon, 2014).

For a thin layer to be detectable, the seismic must have high acoustic impedance contracts and ideally low amount of noise. This is especially relevant in seismic hydrocarbon exploration, where there might be thin layers of hydrocarbons with lower acoustic impedance than brine, which results in high amplitude contrast. In these favourable conditions it is possible to detect layers as thin as 1/30 of the wavelength (Sheriff and Geldart, 1995). An example of high-amplitude events is bright spots generated by gas or water, which can be detected due to significant amplitude contrasts in the seismic, e.g. He et al. (2017). In other words, detectability utilizes the amplitude differences in seismic, while resolution is independent of the amplitude effects.

2.5 Amplitude calibration

The amplitudes of the seismic after data processing can be different from the amplitudes in the reflectivity model, and the amplitude values will differ depending on the modelling method and frequencies. This happens because a seismic wave reflected from the reflectivity target will be affected by several other physical factors along the path (Sheriff, 1975). Removing these unwanted factors (noise etc), is the goal of seismic processing, but the final seismic will at best have relative amplitudes (Kumar, 2018).

In cases where different modelling methods are used, amplitude calibration of all the models used to compare the methods is a prerequisite, this is due to how the modelling methods can affect the amplitudes in a model in different manners. If the amplitude calibration is not executed correctly, the amplitudes of the models will not be comparable, as the scales would be arbitrary.

Often, the amplitudes of the seismic are calibrated using well logs to measure consistency. This is done by extracting wavelets and generate synthetics, and tie the well-log synthetics to the waveform wiggles in the seismic. This calibration process is called seismic well-tie (although amplitude calibration is not the primary application of a well-tie) and after applying this method, the seismic can be interpreted as real geology (Kumar, 2018).

2.6 PSDM images

Seismic forward modelling is performed in this thesis. This is the process of using a geological model to generate seismic images, to help us appreciate geological footprints in the seismic. The 2(3)D convolution modelling method generates prestack depth-migrated (PSDM) images, while the classic 1D convolution generates poststack time-migrated images (Lecomte et al., 2015). This section is a brief introduction to give context about what PSDM and poststack time-migrated images are.

In a seismic survey the receiver measures the time from a shot at a source until the wave hits the receiver after it is reflected from a reflection or diffraction point in the subsurface. This means that the seismic after a survey only shows the reflection events at a time, which is not uniquely resolved, i.e., the event in the trace could be placed in several locations depending on the time recorded at the receiver. Migration is the process where these events are geometrically placed where they occured, in time or depth (Sheriff and Geldart, 1995).

The migration is either done by applying a smooth velocity model, which is generated using well information and geophysical parameters, to the seismic to obtain the seismic in the depth domain. Or in the time domain, where the velocity model only accounts for small vertical velocity variations, and generate 1D models of the traces (Etgen and Kumar, 2012). This is not as robust as the depth migration, as it has problems at complex structures with sharp velocity changes, e.g., salt domes (Yilmaz, 2001).

There is also a choice of whether the migration should be done before or after the stacking of the traces. Stacking is the process of adding together traces to reduce the noise, and thus increase the data quality (Yilmaz, 2001). Prestack migration is when each trace is migrated before they are stacked together. This is the most time-consuming method, but it is done when the structures are too complex to be resolved with poststack migration, where the migration happens after the traces are stacked together.

The 2(3)D convolution modelling method generates these PSDM images, which is the state-of-the-art images we are able to obtain in seismic imaging, while standard 1D convolution generates poststack time-migrated images, which cannot image complex structures, but is often seen as sufficient. Note that for comparison purposes, the 1D convolution results are modelled in the depth domain in this thesis, but this does not alter the seismic.

2.7 Fourier Transform

The Fourier Transform is a central part of the method, being used as the bridge between the PSDM filter in the wavenumber domain and the PSF in the space domain. This section will be dedicated to the wavenumber domain, and more importantly the Fourier Transform.

The Fourier Transform is based on Fourier analysis, which is a mathematic technique where any periodic waveform can be decomposed into a series of sine (or cosine) waves (Kearey et al., 2002). This decomposition process is the Fourier Transform (FT). When the FT is used to convert a waveform in time into a function of frequency, it gives the frequency spectrum, which shows amplitude, and phase, which shows the angles derived from the real and imaginary parts of complex values. The two representations of the waveform in time and frequency domain is called Fourier pairs, which means that the two functions are Fourier transforms of each other (Kearey et al., 2002).

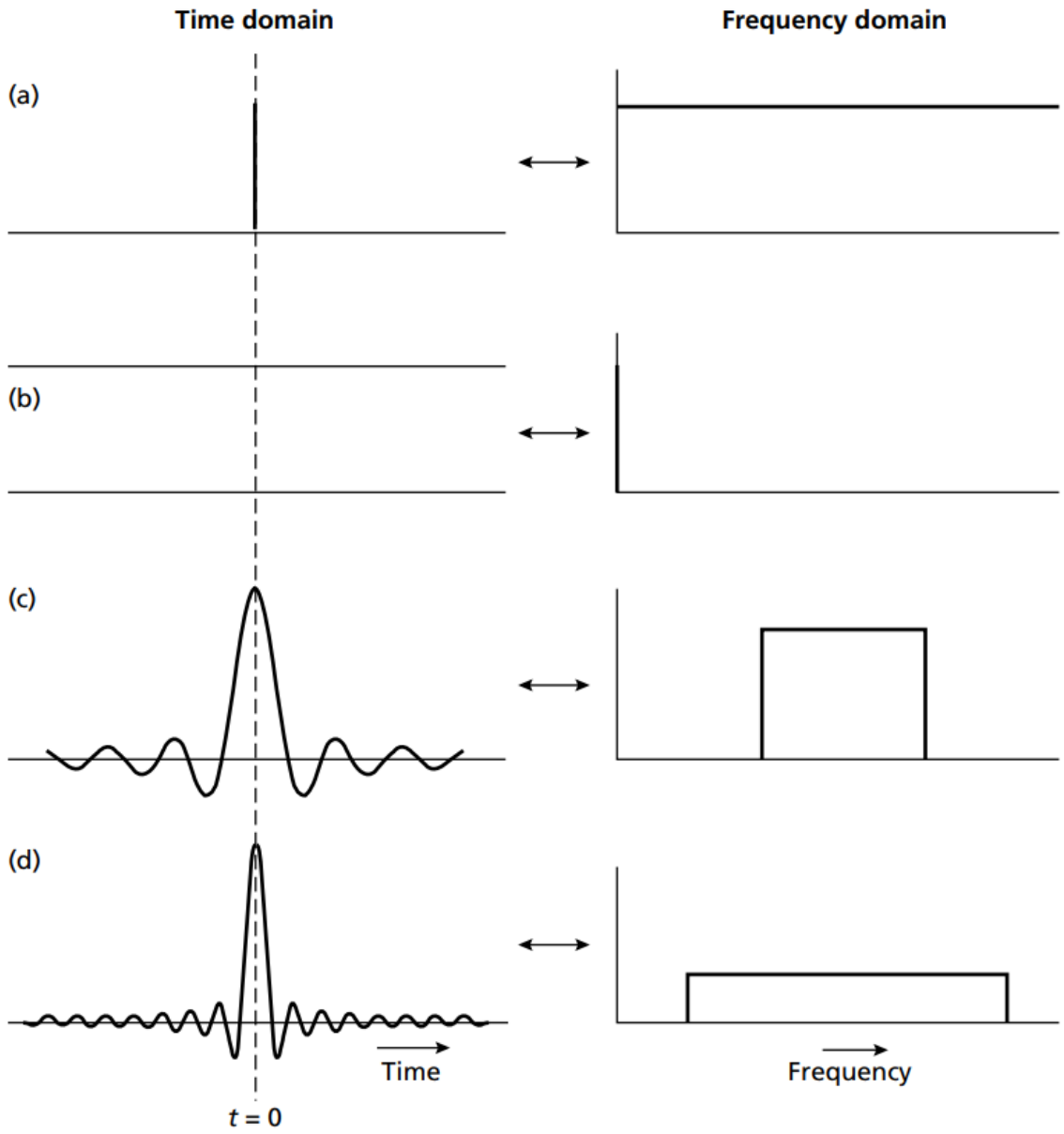

Figure 2.9: *Fourier transforms for four Fourier pairs in the time and frequency domain. (a) A spike function, (b) Continuous line, (c) and (d) Waveforms approximating seismic pulses. Figure from (Kearey et al., 2002).*

Figure 2.7 illustrates four cases of Fourier pairs in the time and frequency domain, each time function (left side) being symmetric around the zero time, thus corresponding to a zero-phase function in the frequency domain entirely described by

its frequency spectrum (right side). This shows the relations between the time and frequency domains, where the two first examples shows two extreme cases, i.e., a spike (impulsive signal with no width) and a continuous one (infinite width), and then two with more complex waveforms approximating seismic pulses in the time domain.

In Figure 2.7, FT is used to relate time and frequency domains, but in this thesis the modelling method uses also FT to relate the space domain to the wavenumber one. A wave is defined by its wavelength and velocity (m/s), where the wavelength is the length of the wave before it repeats itself, given by m, and a wavenumber is the spatial frequency of a wave instead of its temporal one. Frequency is given in Hertz, i.e., 1/s, and is the number of periods per second, and similarly the wavenumber is given as number of wavelengths per unit of distance, so if the unit is given by m, then the wavenumber is given by 1/m, so the FT from space to wavenumber is analogous to the FT from time to frequency.

2.8 Convolution

Convolution is a mathematical operation defining the effect a filter has on an input waveform shape (Kanasewich, 1981). In a convolution an input signal g(t) is convolved with the impulse response f(t) of a filter to give the output (filtered) signal. The impulse response itself is defined as the response of the filter when the input signal is a spike function (Figure 2.8):

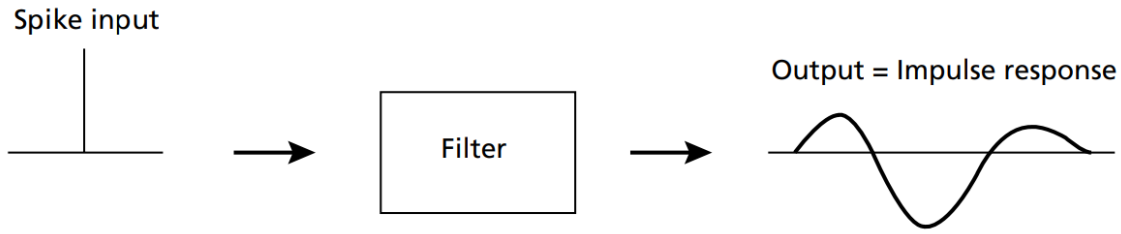

Figure 2.10: *A spike function convolved with a filter, and its resulting impulse response. Figure from (Kearey et al., 2002).*

The result of the convolution of any input signal g(t) with the impulse response f(t) will be the filtered output $\gamma(t)$:

$$\gamma(t) = g(t) * f(t) \tag{2.10}$$

The asterisk is known as the convolution operator. Any transient wave can be seen as a mix of spikes, so we can visualize any convolution by the effects the associated impulses have on each other (Kearey et al., 2002).

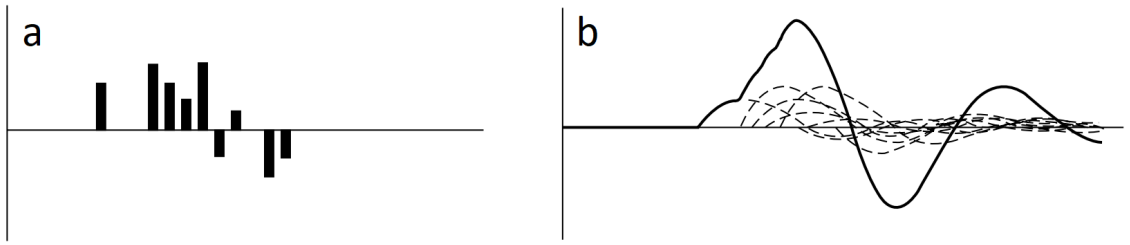

Figure 2.11: *(a) A mix of spikes generated from a signal and (b) its associated impulse responses, added together to show the wave after convolution. Figure from Kearey et al. (2002).*

Convolution in one domain is a multiplication in the other (FT-related) domain. Convolution in the time domain, e.g, equals a multiplication in the space domain. This is what happens in the software used in this thesis, where the modelling options in SeisRoX are generating the PSDM filter in the wavenumber domain, then it multiplies that filter to the FT of the input reflectivity, before taking an inverse FT to get back to the space domain.

I will not go into depth about the mathematical implementation, only a general understanding of convolution is needed to analyse the modelling method studied in this thesis, but I refer the reader to (Kearey et al., 2002), or (Kanasewich, 1981) for more information on convolution approaches.

2.9 1D Convolution

In the industry, the dominating convolution method is 1D time convolution and it has been used for decades to design seismic acquisition, processing, imaging, and inversion (Lecomte et al., 2015). The 1D convolution works on 1D reflectivity logs (e.g., from well logs or extracted trace per trace in a time model), and convolve them with chosen wavelets to generate seismic traces. The chosen wavelet is often a zero-phase Ricker because of its simple side lobes. This process can be expressed mathematically as (Huang et al., 2007):

$$X(t) = W(t) * R(t) + N(t) \tag{2.11}$$

where X(t) is the seismic trace, W(t) is the input wavelet, R(t) is the reflectivity function and N(t) is the added noise to make the seismic trace realistic. The reflectivity coefficient (RC) is given as spikes along the time axis from reflection or diffraction events (Figure 2.9). That reflectivity function is only varying along one dimension, hence the name 1D convolution.

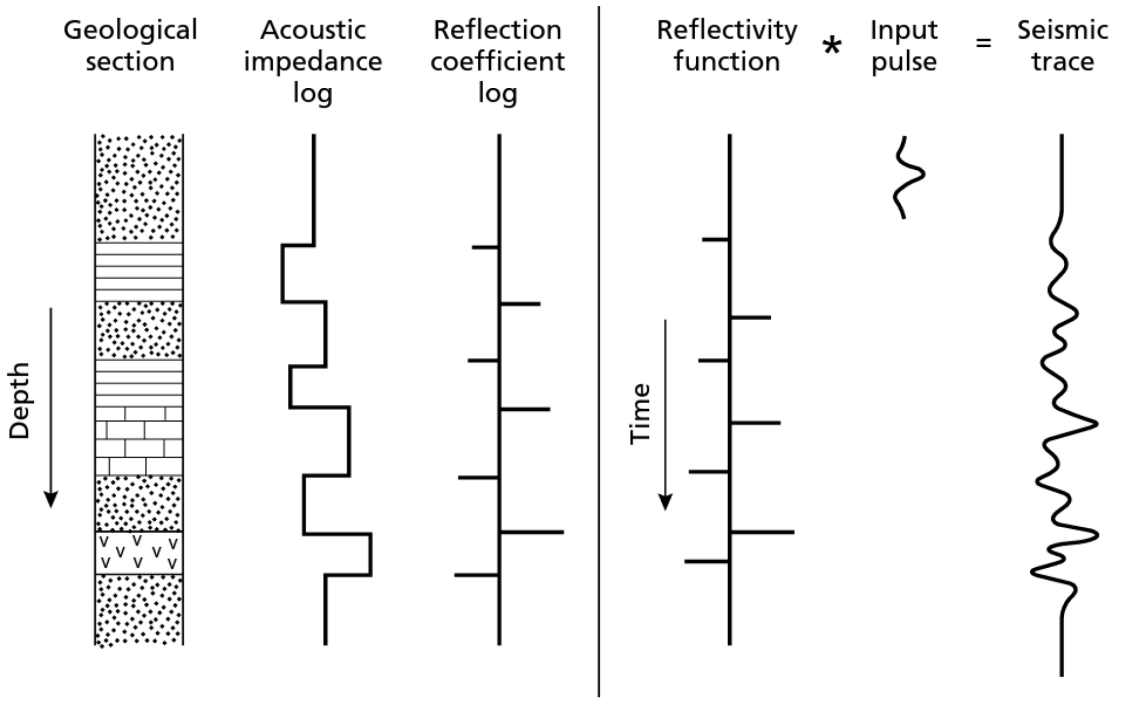

Figure 2.12: *The acoustic impedance contrast at boundaries between layers in the geological section gives the reflection coefficient log in depth. The resulting reflectivity function in the time domain is convolved with the input pulse for the seismic trace. From: Kearey et al. (2002).*

The 1D convolution method simulates poststack time-migrated images (Lecomte et al., 2015). As the 1D time convolution is only performed in the time domain, the time-dependent reflection function must be generated. This gives one of the key problems in 1D time convolution; how to generate the time function so that it represents the reflection coefficient log in a proper fashion. Another is which wavelet to choose, as the side lobes will affect the seismic trace different depending on the distance between the layers in the geological section.

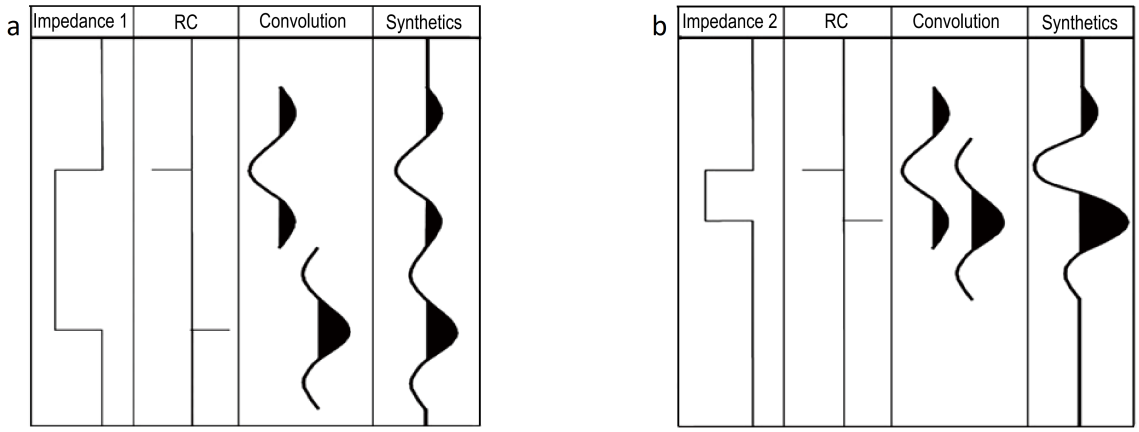

Figure 2.13: *Two different impedance examples to show how 1D convolution works. (a) A longer bed between impedance contrasts than (b). From: Huang et al. (2007).*

The different distances between the reflectivity coefficients in Figure 2.13.a versus 2.13.b make possible the observation of the effects of vertical resolution introduced earlier;, the side lobes have a more significant effect on the synthetic seismic trace in case (b) than in (a). This also illustrates the importance of the side lobes in a wavelet, as wavelets with several side lobes will generate a substantial amount of noise in the seismic. As a result, close-by layers will have an effect on each other.

As shown in Figure 2.13, the 1D time convolution is quite simplistic, as the wavelet is inserted at the RC spikes, and added together for the synthetic trace. Since the reflection coefficients are a result of the formation impedance, the only variable is the wavelet, and which wavelet to use will be essential.

To illustrate that a 1D convolution has no lateral effects, we can observe how a 1D convolution operator appears when using the same variable-density image style as later for the PSFs (Figure 2.14). In later chapters the wavelet is illustrated in the same manner as the PSFs, but it is really just a wavelet as figure 2.14.b shows.

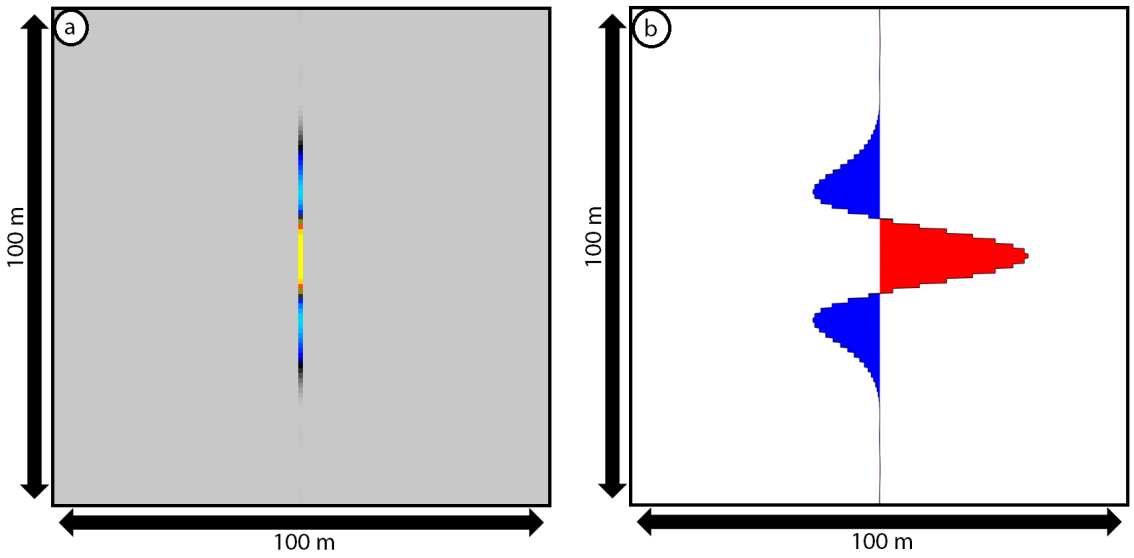

Figure 2.14: *30 Hz Ricker wavelet presented (a) in the same style as PSFs (variable density), and (b) as a wavelet.*

The 1D time convolution is a quick and uncomplicated modelling method, but at a cost, as it does not consider any lateral resolution effects nor lack of illumination issues. As the velocity and density distributions in the Earth are not one-dimensional, while seismic acquisition and imaging are not perfect, both lateral resolution and illumination effects, in addition to the well-studied vertical resolution ones, should be accounted for ((Lecomte et al., 2015)). The present study is an attempt to analyse and illustrate the impacts of such seismic-imaging issues, e.g., on amplitudes and other structural information. Despite its lateral shortcomings, 1D convolution modelling is still a popular choice to this day, e.g. Pemberton et al. (2018), where they use 1D convolution modelling with Ricker wavelets of a variation of frequencies, hence the need to further highlight what might still be missing in such standard modelling.

Chapter 3

PSF-based convolution modelling

In this chapter the modelling method will be presented in its entirety, now that the various key principles behind the method have been exposed. As earlier mentioned, this modelling method is originally ray-based, meaning that the method derives from a high-frequency approximation of the wave equation, and is illustrated by rays instead of waves in the subsurface. We use slowness vectors which is normal to wavefronts, to express the illumination of the reflection/diffracted events.

3.1 From illumination to PSF

The first step towards generating a PSF is to find the illumination vector, which describes the illumination of a point in a velocity model, based on the slowness vectors for the incident and scattered wavefield. The slowness vectors are calculated by ray-tracing methods as previously explained.

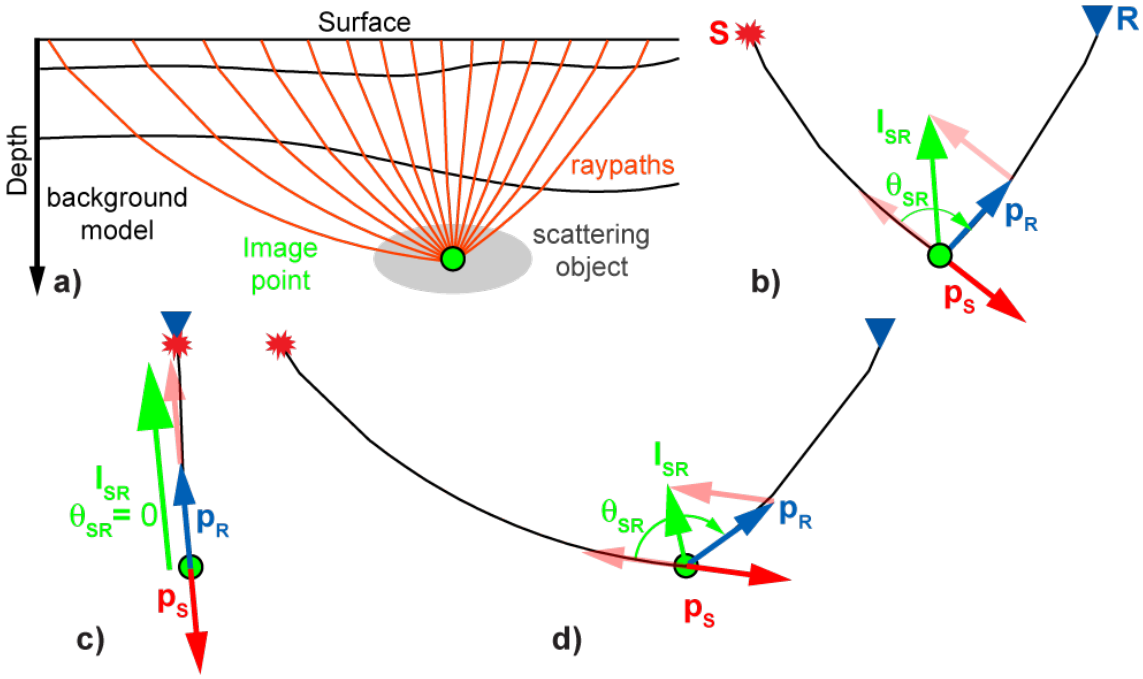

Figure 3.1: *An illustration of how the opening angle causes shorter illumination vectors in a homogenous media, where* $\boldsymbol{p_S}$ *and* $\boldsymbol{p_R}$ *are the slowness vectors for the incident and scattered wavefield, respectively,* $\boldsymbol{I_{SR}}$ *is the illumination vector, and* $\boldsymbol{\theta_{SR}}$ *is the opening angle. (a) Background model with a reference point (green dot) in the zone of interest and an array of sources and receivers. (b) Source (red star)-receiver (blue triangle) pair with a short offset, therefore a narrow opening angle and a long illumination vector. (c) Zero-offset pair, where the illumination vector is at its longest for this survey. (d) Large offset, wide opening angle, and therefore a short illumination vector. From: Lecomte (2008).*

These three cases of Figure 3.1 show how the choice of source/receiver pair affects the length of the illumination vector; a long illumination vector gives better resolution than a short one, and as the figure illustrates, the length will decrease with offset in a homogenous media, i.e., increase in the opening angle $\theta_{\mathbf{SR}}$. If the incident wave is of the same type as the scattering one, then we can express the illumination vector mathematically by:

$$\mathbf{I_{SR}} = \mathbf{p_R} - \mathbf{p_S} = \frac{\hat{\mathbf{u}}_\mathbf{R} - \hat{\mathbf{u}}_\mathbf{S}}{V} = \frac{2\cos(\theta_{\mathbf{SR}}/2)}{V}\hat{\mathbf{u}}_{\mathbf{SR}} \tag{3.1}$$

where V is the velocity of the waves at the reference point, while $\hat{u}_S$ and $\hat{u}_R$ are two unit vectors perpendicular to the incident wave front from source s and to the

scattered wave front towards receiver r, respectively (Lecomte, 2008). The resolution is at a maximum at zero-offset, where $\theta_{\mathbf{SR}}$=0, and $\mathbf{I_{SR}}$=2/V.

The next step towards generating the PSF is to define the scattering wavenumber vector (K_{sr}). This is done by multiplying the illumination vector with frequency f (according to the frequency band of a chosen wavelet). Since the illumination vector is given by the slowness vectors, with unit 1/(km/s), and frequency is Hz, 1/s, the product of the multiplication will be in unit 1/km, which is the unit of wavenumber.

After all the K_{sr} are calculated at the reference point for the source-receiver pairs in the survey, we map the K_{sr} in the wavenumber domain and weight them according to the frequency spectrum of the selected wavelet. This is the PSDM filter, and the last step is to apply a Fourier transform from the wavenumber domain to the depth domain, where we finally obtain the PSF (Lecomte, 2008). The whole process from illumination vectors to PSF is illustrated in Figure 3.2.

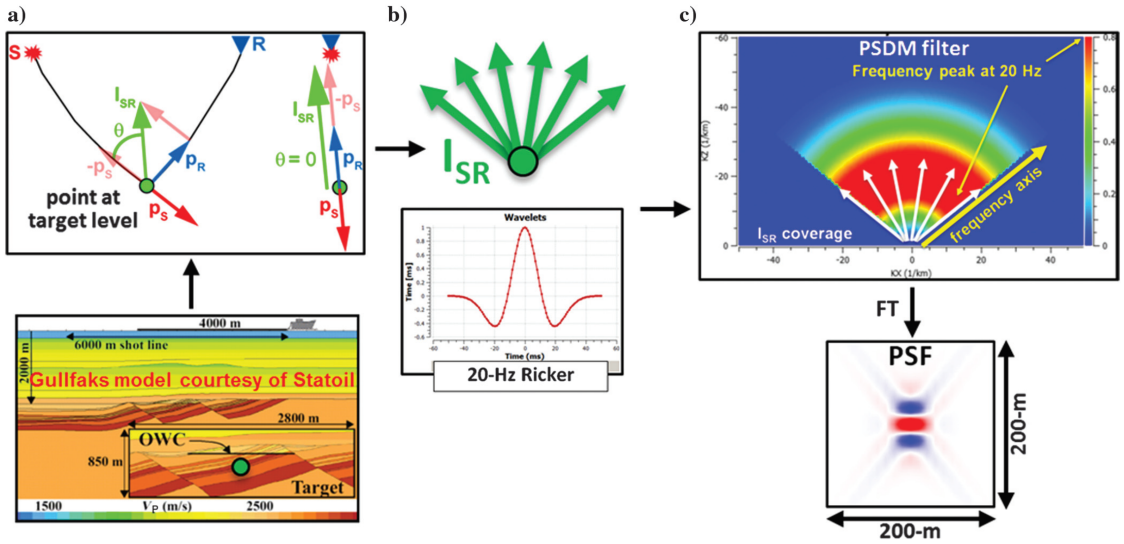

Figure 3.2: *Illustration of the basic elements in the 2(3)D convolution method. (a) Shows the illumination vector from the target in the Gullfaks model (green dot), note: in this figure θ is the incident angle, i.e., half of the opening angle $\theta_{\mathbf{SR}}$. (b) Is the resulting illumination range and a wavelet to generate (c) the PSDM filter in the wavenumber domain, and the final step is to Fourier transform the PSDM filter to (d) the resulting PSF. From: Lecomte et al. (2015).*

Figure 3.2 also illustrates how the angles of the PSDM filter is controlled by the survey. In (a), an illumination vector is generated by a slowness vector pair of a selected shot-receiver pair in a survey. The illumination vectors for the whole survey

is illustrated in (b), which shows the cut-off angle due to the survey restrictions in a. In (c), these illumination vectors are superimposed on the resulting PSDM filter, which has a cut-off defined by the illumination range.

The PSDM filter and PSF are thus Fourier pairs, so the PSDM filter and PSF are made up of the same values, but given in different domains. Naturally, the shape of the PSF will be dependent on the shape of the PSDM filter, where the opening angle of the PSDM filter will determine the cross pattern angle in the PSF. Figure 3.3 illustrates the relationship between a dipping reflector in the two domains.

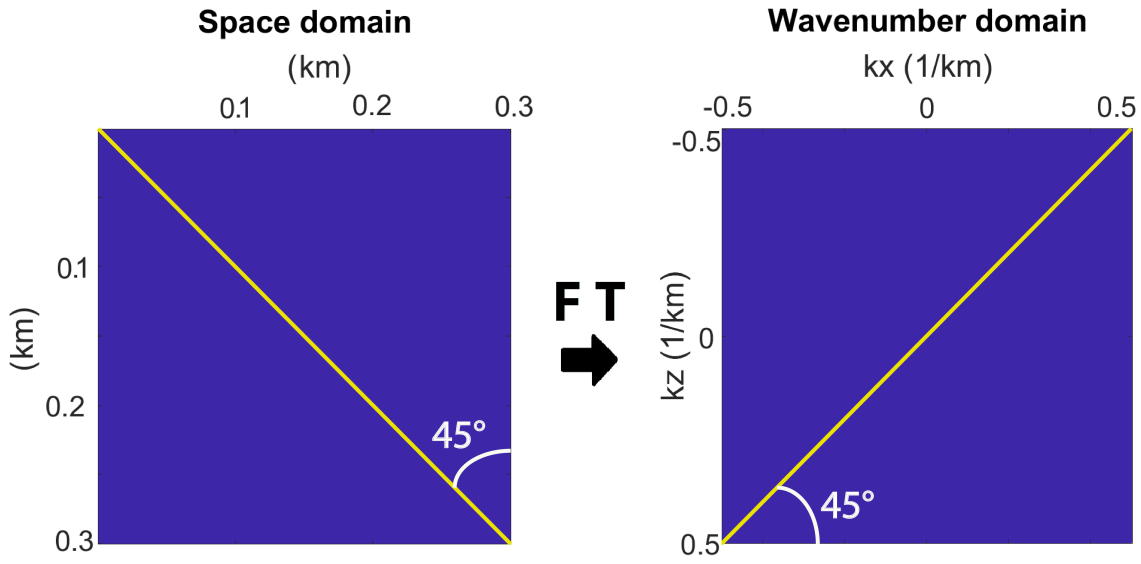

Figure 3.3: *A dipping reflector in the space and wavenumber domain after a Fourier Transform. Figure stretched.*

The PSDM filter of Figure 3.4 (left), corresponding to illumination of reflectors with dips varying from 0° to 45° has a limited lateral aperture(opening of the coloured cone) which also determines the cross pattern angle in the corresponding PSF (Figure 3.4, right). To illustrate the effects attached to that limited aperture, I added pink and white lines onto the 45°dip limits in the PSDM filter to show how these lines explain the cross pattern of the PSF after a Fourier Transform (truncation effect; See Figure 2.7.c/d for that effect in 1D).

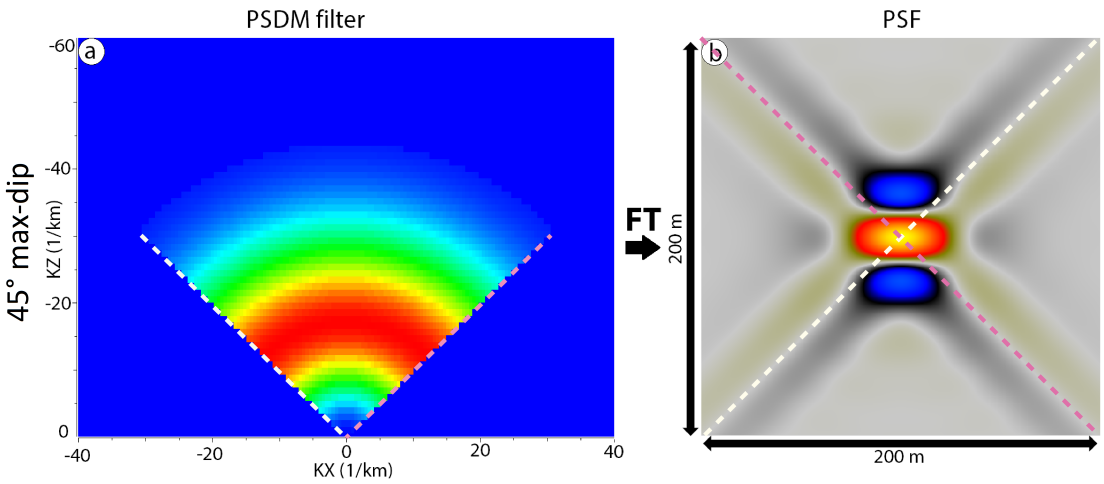

Figure 3.4: *(a) A 45° max-dip PSDM generated by a Zero Offset survey, with a 30 Hz Ricker wavelet. (b) The corresponding PSF. Dip angles in the PSDM filter and PSF highlighted in pink and white.*

The cross-patterns and the size of the mid-section of the PSF in Figure 3.4 causes lateral resolution effects. This means that the PSFs at reflection/diffraction points has an effect on each other laterally, as well as vertically.

3.2 The Point-Spread Function

A perfect PSF should ideally be a circle in the space domain, which would correspond to a perfect illumination where all reflector dips are imaged (circular PSDM filter in the wavenumber domain). However, a reflection/diffraction point would never be perfectly illuminated in actual seismic, as this would require a 180° span of source and receivers. But we should aim to get PSF as close to perfect illumination as we could, i.e., a wide PSDM filter, as this would yield a sharper PSF. In this thesis the perfect illumination PSF is a half-circular (not dealing with turning waves) a where all dips from 0° to 90° are illuminated.

I made a 600 m x 1000 m reflectivity model of two intersecting sills (Figure 3.5), with a fine 50-cm sampling to observe the effects of some different shapes of PSFs and how they are generated by the PSDM filter. I first convolve the reflectivity model with a 1D "PSF" convolution operator, which is the 1D-equivalent of a PSF (i.e., just the wavelet stretched in depth according to the velocity), a perfect illumination PSF, a 45° max-dip PSF, as the one in Figure 3.4, and a PSF generated from a 20-degree incident-angle case, obtained for a given survey, with holes in the PSDM filter due

to a coarse source and/or receiver sampling which causes sparse illumination vector coverage. The latter is only used to illustrate lack of illumination in a survey, it is not studied beyond this chapter.

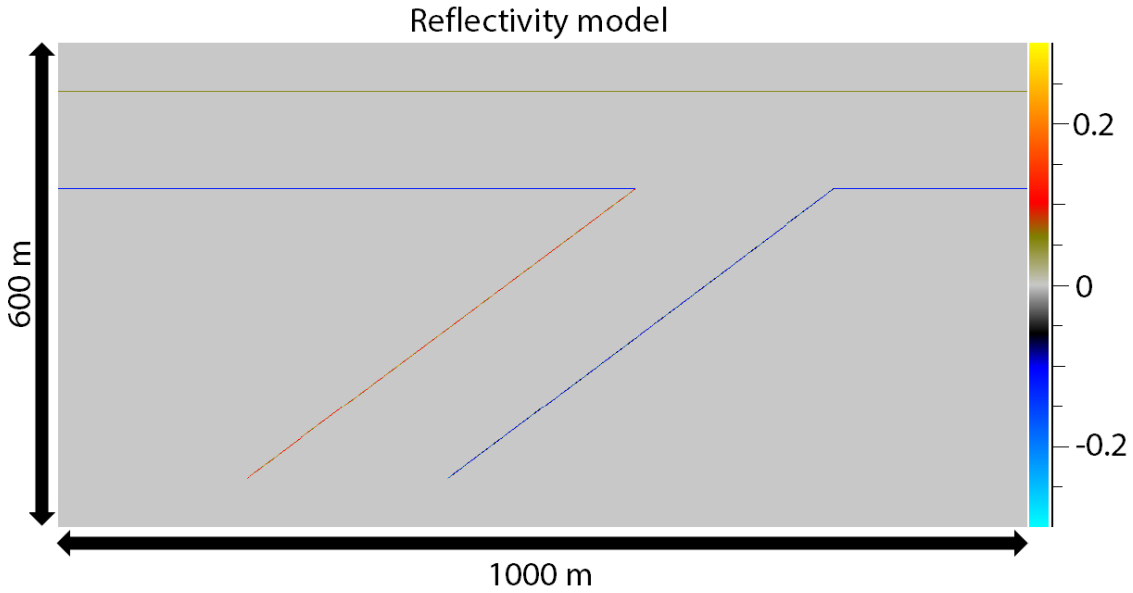

Figure 3.5: *Reflectivity model based on an intrusion model from (Magee et al., 2015).*

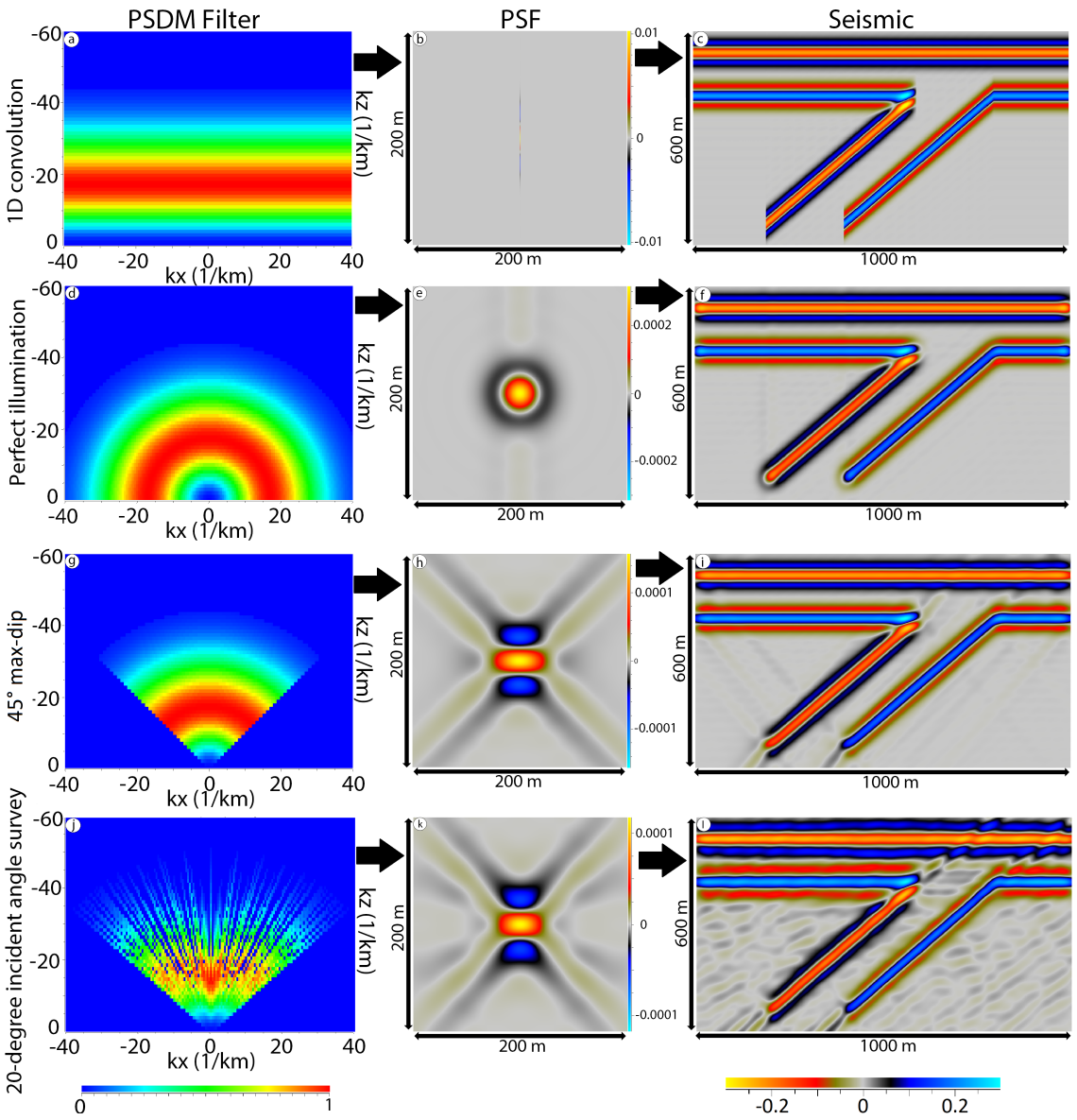

Figure 3.6: *Four PSFs generated from PSDM filters with different cases of illumination, convolved with the reflectivity model from figure 3.5. (a)-(c): 1D convolution. (d)-(f): Perfect illumination. (g)-(i): 45-degree max dip. (j)-(l): A 20-degree incident angle survey.*

Due to the value differences in the PSFs, I will generally illustrate the PSFs I use with the same relative "-max to max" amplitude scale, since the important part is the shape of the PSFs; the proper calibrated amplitude values will however be used for the modelled seismic.

In Figure 3.6, the four cases are presented to illustrate how the final seismic is affected by the illumination range and its vector coverage when generating the PSDM filters. From (a)-(c) is the PSF-equivalent of a 1D convolution, where the PSDM filter is a horizontal line, which generates a lateral PSF with the size of a pixel. This causes a seismic to have an uneven shape due to the thin vertical 1D "PSF".

In the case of a perfectly illuminated PSDM filter, Figure 3.6.d, the corresponding PSF is a circle, with some noise vertically, caused by the horizontal cut-off of the PSDM filter at low wavenumbers. The resulting seismic has a lateral resolution effect due to the size of the PSF, causing the seismic to be "rounder" than the 1D case.

A more realistic PSDM filter is presented in Figure 3.6.g, where I have a 45° dip PSDM, as also illustrated in Figure 3.4, where the cut-off causes the PSF to have a cross-pattern. This causes the seismic to include oblique striations, in addition its lateral resolution effect; lateral smearing, due to the mid-section of the PSF being longer than for the perfectly illuminated PSF.

In all the three previous cases I used analytical filters, which assumes a dense set of zero-offset illumination vectors. Therefore, I wanted to illustrate what may happen when this is not the case, purely to show the effects caused by a lack of a dense set of illumination vectors. This case is not used in the modelling section, where we run full-field (as done with Figure 3.6.a,b,c, and not a local survey which causes the lack of illumination.

This was done by defining a normal survey with an array of offsets, where I used the incident-angle range to select a 20° incident angle survey. The parameters of my survey caused the PSDM filter to have holes in the illumination range due to the source and receiver spacing. This survey has a maximum illuminated dip of 45° and the resulting dip and holes in the PSDM filter causes the PSF to include more noise, which is transferred into the seismic.

The illumination is dependent on the location of the target reflector in the velocity model, which consequently causes the PSF to change. To illustrate how the layers in a model can alter the illumination range and coverage I chose a reference point in a zero-offset case in an isotropic media. This velocity model is used as an example of how high-velocity layers alters the density in the illumination range, but it is not a classical background model which would be used to compute the illumination vectors in.

In zero-offset cases in isotropic media, the rays which directly connects the reference point and points at the surface can be used as a proxy to illustrate the illumination vector coverage at that point. This coverage corresponds to the illumination range as seen in Figure 3.2.b. For the different examples the survey and lateral position of the reference point at which I calculate the PSF is consistent, the only difference

is the depth of the reference point.

The illumination can change drastically within a velocity model, as with the sill intrusions one, presented here. In Figure 3.6.e, the PSDM filter is generated below the intrusion in the model. To illustrate how the illumination alters with depth I made a smaller version of the figure 3.5. In Figure 3.7 I used a zero-offset survey to illustrate the difference due to the location of the target in a case with an intrusion.

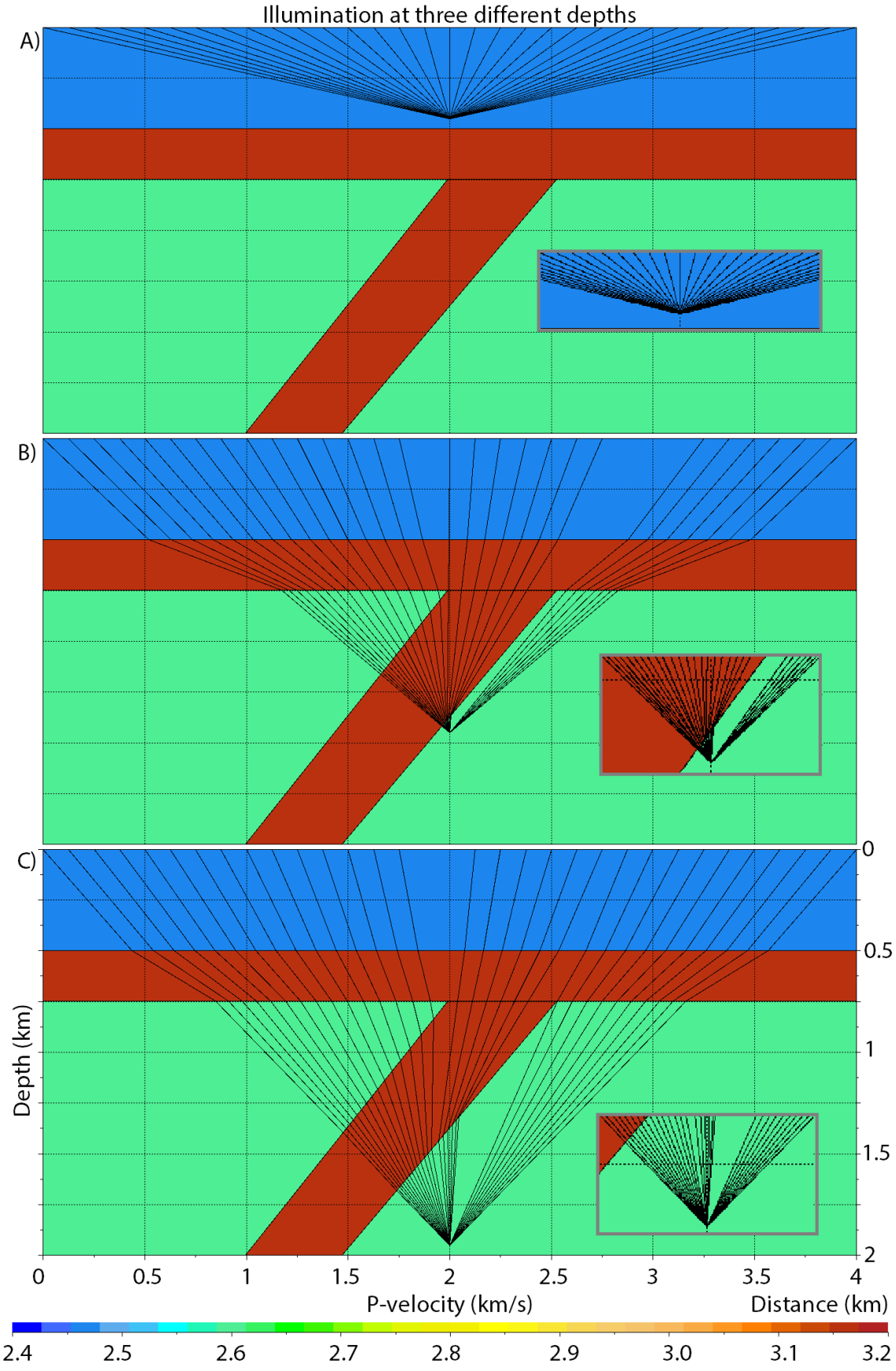

Figure 3.7: *Three different reference points where we could do a "target-oriented" modelling, and use the PSF calculated at these points. The three targets are located (a) over the sill, (b) below the sill and (c) at the bottom of the model.*

Figure 3.7 illustrates three cases with different depths of the reflection point. In location (a) the target reflector is above the high-velocity intrusion, which gives a wide illumination range without gaps due to the ray path changing. However, since it is so shallow, there will be gaps above the considered point due to the spacing of the survey. The result is a wide illumination range, albeit with a sparser illumination pattern in the mid-section which could cause noise in the PSF, hence in the seismic images like in Figure 3.6.j-l.

In figure 3.7.b the reference point is located below the intrusion sill. The high velocity of the intrusion causes the ray paths to alter their direction, which causes the illumination range to narrow. It also causes a significant gap in the illumination. Location (c) is further down, which results in a wider illumination range than in case b, and since this is further away from the intrusion, the illumination gap is now narrower, but still significant. While in the illuminated areas, the rays are closer together, so the illumination range is denser than both previous examples.

In Figure 3.8 I generated PSDM filters and PSFs which correspond to the reference points in Figure 3.7. These are approximations designed to illustrate noise in the PSF caused by illumination effects in the survey. In Figure 3.8 case (a) the symmetric, but poorly illuminated PSDM filter causes a PSF with noise in between the cross-patterns, but the middle part is symmetric. In case (b) and (c), the PSFs have an asymmetric shape due to the gap in illumination range in the PSDM filters.

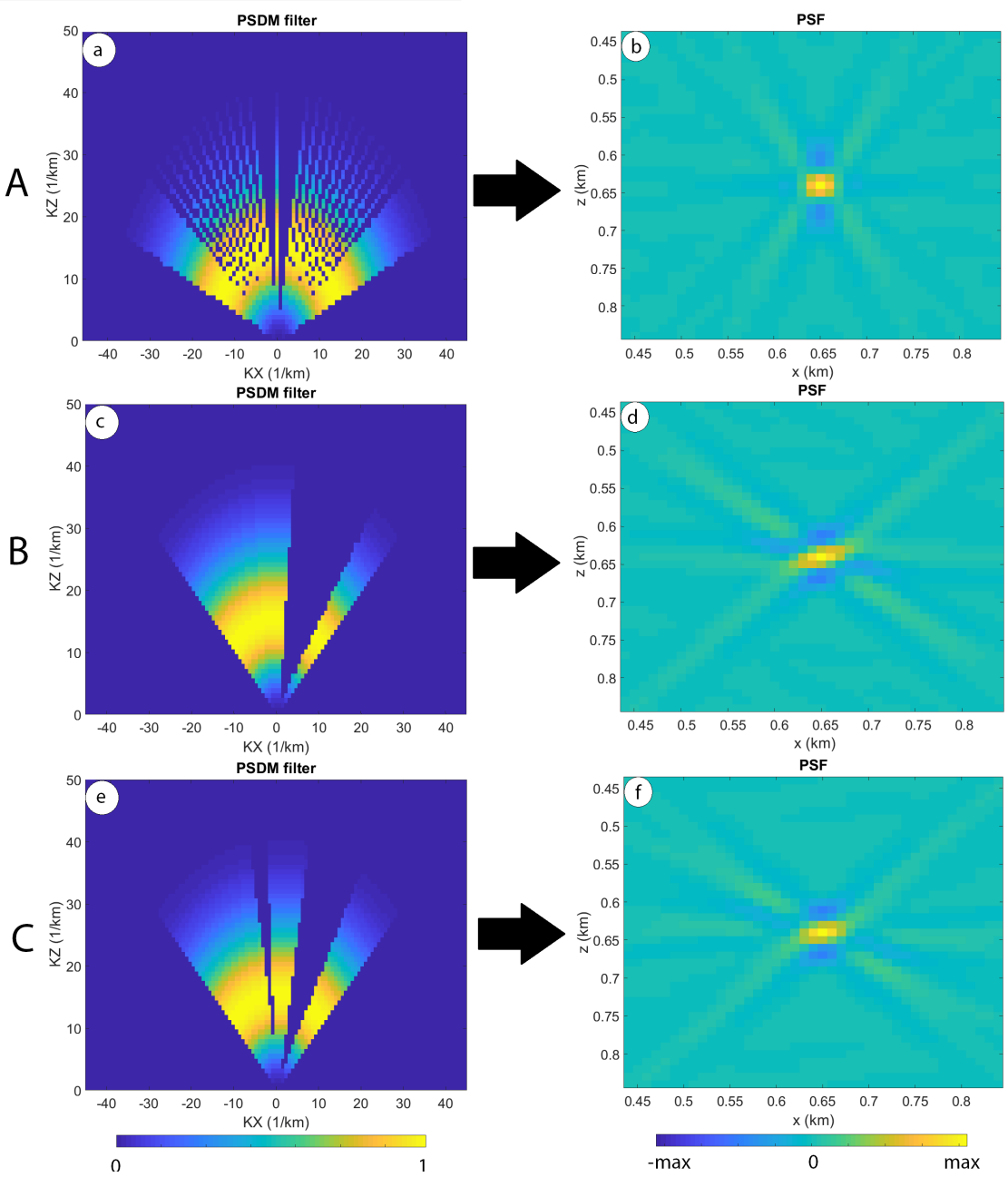

Figure 3.8: *PSDM filters and PSF corresponding to the three targets A) a-b: over the sill, B) c-d: below the sill and C) e-f: at the bottom of the model.*

To summarize and conclude the method chapter, we choose a reference point in a velocity model, then generate the illumination vectors at that point, before multiplying them with the frequency to map them in the wavenumber domain, adding the

frequency spectrum of a user-chosen wavelet as a weight. The resulting PSDM filter is Fourier Transformed to a PSF, which is then convolved with an input reflectivity model around that reference point ot get the synthetic seismic.

Chapter 4

Results

After becoming familiar with the method, I will study how wavelets and surveys affect the PSF before comparing the 2(3)D PSF modelling method with standard 1D convolution modelling using 2D and 3D reflectivity models with varying degrees of complexity.

4.1 Survey effects

What seismic is able to resolve and illuminate in a reflectivity model is determined by the shape of the corresponding PSDM filter. In particular, the aperture of the filter is a result of the survey geometry, to examine the survey effects on resolution and illumination, I generated four PSFs from four different zero-offset surveys in a homogenous velocity model, and convolved them with the reflectivity model from Figure 4.1.a.

This reflectivity model can illustrate how the illumination limits impacts the seismic depending on the PSDM filter. Figure 4.1 illustrates how the range of the PSDM filter controls whether a reflector is illuminated or not. The normal of a reflector needs to be inside the range of the PSDM filter for the reflection to occur, i.e., the reflector to be illuminated (Lecomte, 2008).

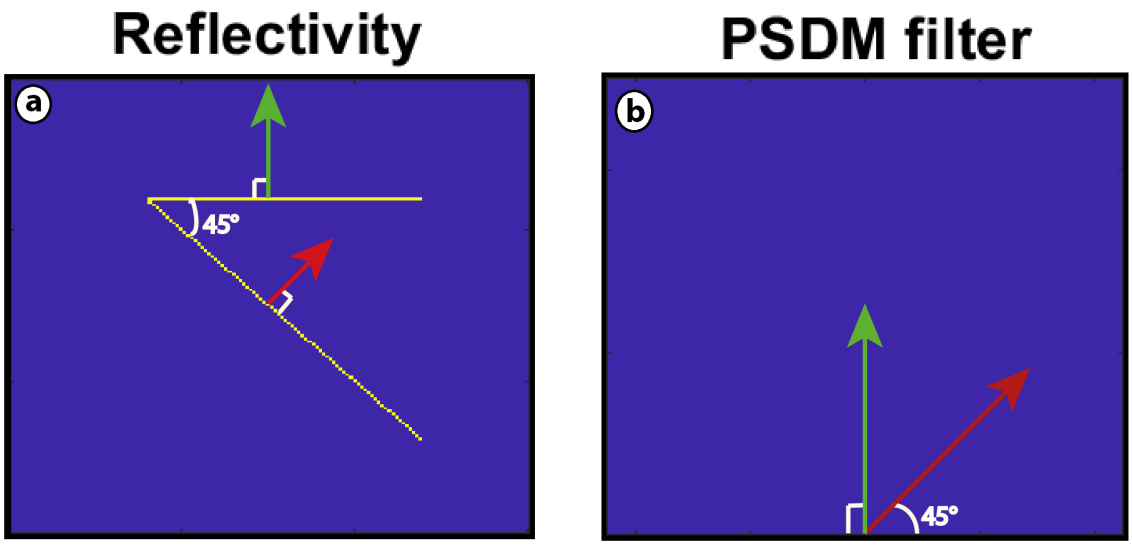

Figure 4.1: *Illumination. (a) The reflectivity model used, with two vectors normal to the horizontal and 45˚ dipping reflector. Red vector normal to the dipping reflector, green vector to the horizontal reflector. (b) The normals together to show the illumination range needed from a PSDM filter to illuminate both events.*

I generated four zero-offset surveys to generate the PSFs, each with 150 shots (except for the last which had 300 shots). The first survey illuminates the left side of the target, the second illuminates the right side. The third has the same length, but is centred above the target, and the last survey covers the whole 300 m, a summation of the two first surveys. The target has a sampling of 5 m in the xz-direction and a 30 Hz Ricker wavelet.

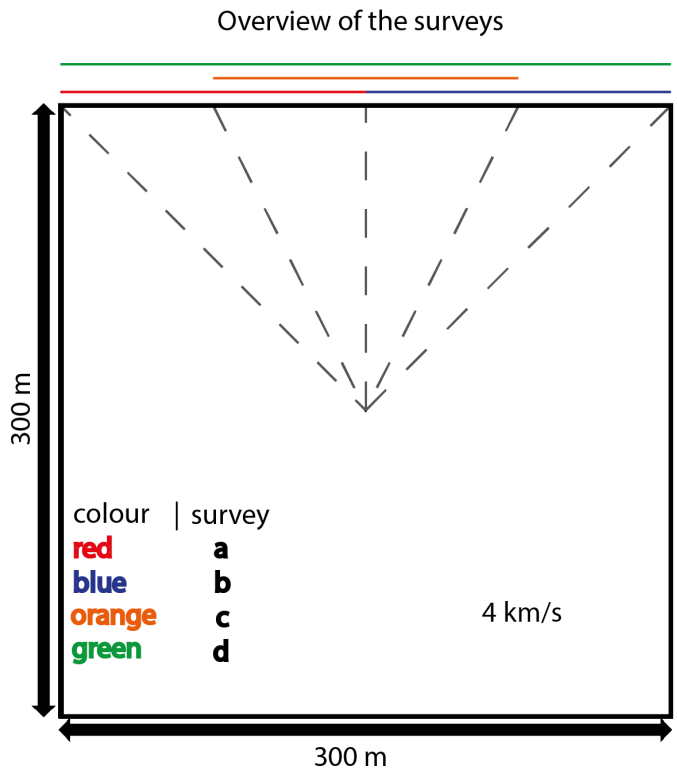

Figure 4.2: *A homogenous 4km/s background velocity model, with four different zero-offset surveys. Survey (a) is a survey from zero to 150 m, straight above the target, (b) starts above the target, and ends at 300 m. Survey (c) starts in the middle of (a), and ends in the middle of b), while survey (d) covers the whole distance from zero to 300 m with 300 shots. Dotted lines illustrate the extremities of the ray paths.*

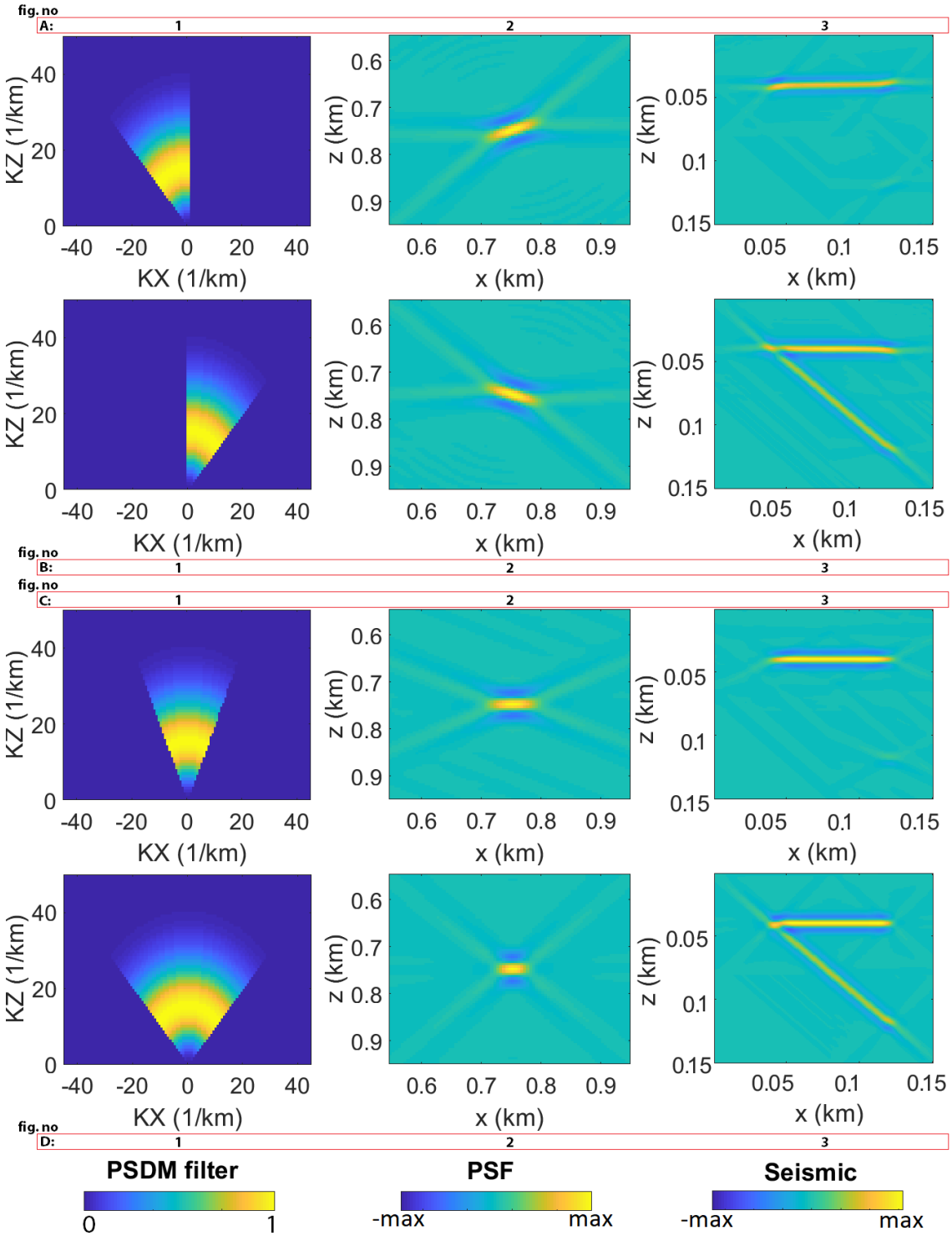

Figure 4.3: *The PSDM filters (column 1), PSF (column 2), and seismic (column 3) for Survey (a),(b),(c) and (d). fig. no A, B, C and D, respectively.*

The four surveys give four different PSDM filters, where the two first, A1 and B1, will be asymmetric, while the last two, C1 and D1, are symmetric. These differences in illumination affect the final seismic, as the asymmetric PSDM filters causes oblique PSFs, which causes the extremities of the horizontal reflector to have patterns from the PSFs. This is not the case for the PSDM filters which are symmetric about the zero value. If the illumination range is not covering some of the normals of the reflectivity, then it is not present in the seismic.

For the first survey, the PSDM filter A1, has a 45° illumination range from the left side to directly above the target point. This causes the PSF to dip in the same direction, and convolving this dipping PSF with the reflectivity model (Figure 4.1.a), results in a seismic where the horizontal is illuminated, but the dipping reflector is not illuminated at all.

Survey (b) goes from above the target to the end of the survey. The corresponding PSDM filter B1 covers the normals of both reflectors in the reflectivity model, as illustrated in figure 4.1, with a a range from 0° to 45° on the right side. The PSF will be dipping in the direction of the dipping reflector, and the whole wedge model is illuminated. The third survey (c), is directly above the target, with dips on from 0° to about 22.5° on both sides. The corresponding PSF only illuminates the horizontal layer. Since the opening of the cone, the aperture, is the same for (a), (b) and (c), they have the same lateral resolution.

If we add together the two surveys (a) and (b), we get survey (d), which covers the whole survey area. The resulting PSDM filter, D1, corresponds to a complete illumination with dips from 0° to 45° on both sides. This causes the whole target to be illuminated, and without dips at the end of the reflectors.

4.2 Wavelet effects

In the process of generating the PSDM filter, we must choose a wavelet with a given dominant frequency to attach to the illumination vectors. As interpreters, we must know which effects the different wavelets and their frequency band will have on the seismic. The width of the main lobe in a wavelet defines the resolution, where a thin lobe gives a better resolution than a broad one. In addition, the wavelets have side lobes generates noise in the seismic. In the software I use in this thesis, NORSAR SeisRoX, the standard synthetic wavelet I can generate is a zero-phase Ricker wavelet, also known as a Mexican hat wavelet.

The Ricker wavelet is relatively simple, with two smaller side lobes on each side of the central peak (symmetrical wavelet since it is zero-phase), where we only need to define the dominant frequency. As an example of a more complex wavelet, I chose

the Ormsby wavelet, where there are multiple side lobes. The input frequencies are the low-pass, low-cut, high-pass and high-cut, along with a more complicated equation which results in numerous side lobes (Ryan, 1994). I used MATLAB to generate values for an Ormsby wavelet, which I imported into SeisRoX.

In a real survey, the pulse contained in a migrated seismic section, i.e., obtained after processing (including deconvolution) and as extracted for seismic inversion, would have some side lobes, so the Ormsby wavelet is the realistic choice, but for a modelling study where the goal is to understand the acoustic signature for different survey geometries, it is reasonable to choose a wavelet without additional side lobes, e.g., the Ricker wavelet. The choice of frequency is also dependent on the degree of realism the user wants, as the frequency will decrease with depth due to attenuation.

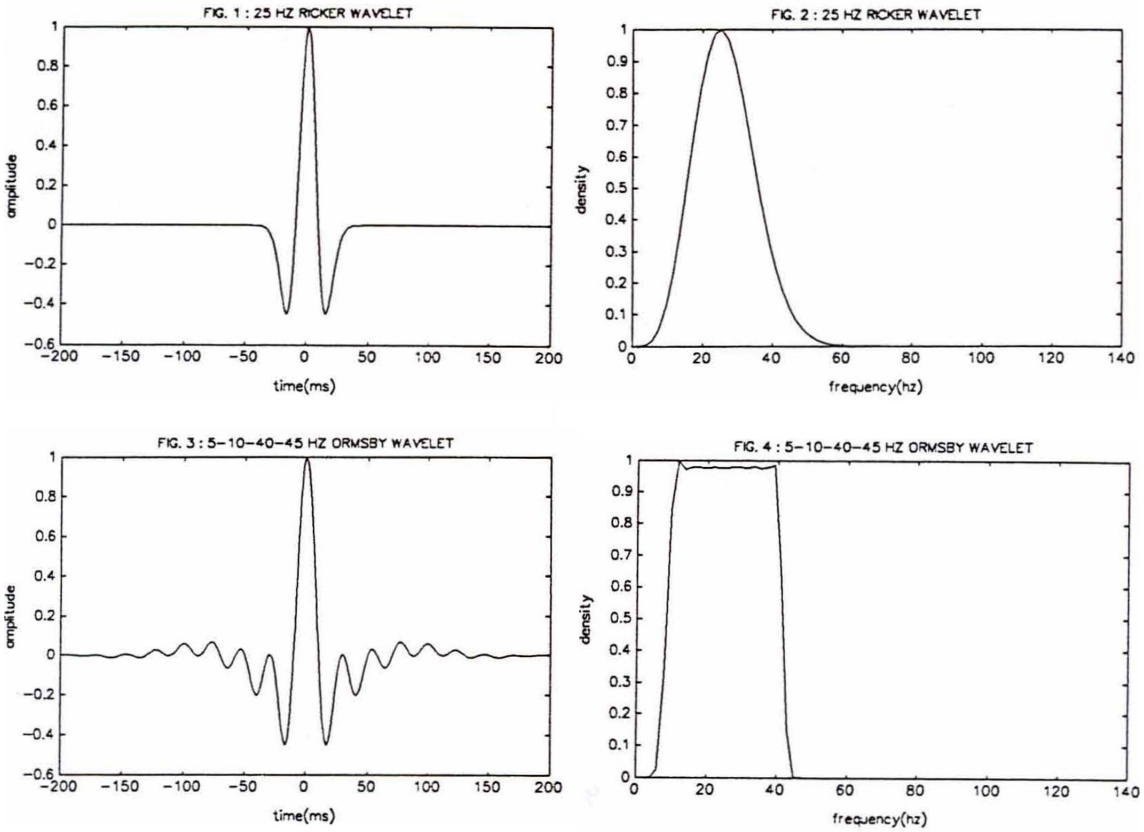

Figure 4.4: *The Ricker and Ormsby wavelet in the time and frequency domain Ryan (1994).*

Figure 4.4 from Ryan (1994) shows the difference between the 25 Hz Ricker and an Ormsby with low-pass, low-cut, high-pass and high-cut frequencies of 5 Hz, 10 Hz,

40 Hz and 45 Hz, respectively, both in the time and frequency domain. These values are not chosen at random, as the figure shows the peak amplitudes of the Ricker and Ormsby will coincide with each other, making it possible to observe the effects of side lobes.

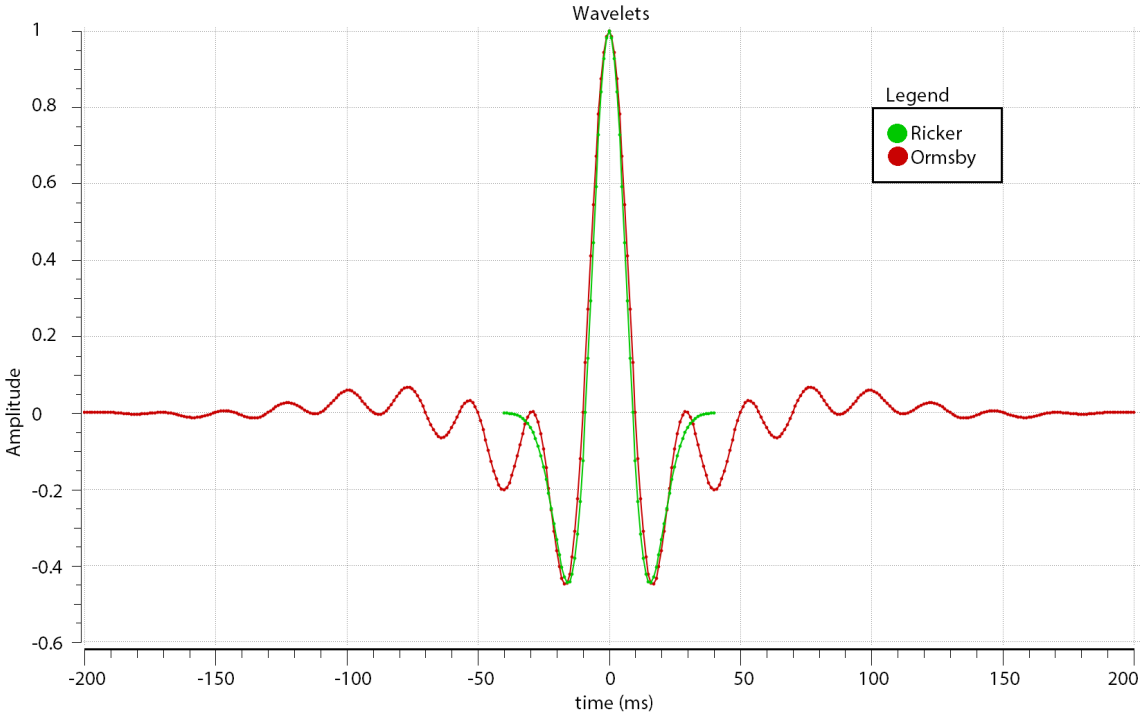

Figure 4.5: *The 25 Hz Ricker and corresponding Ormsby wavelets being compared.*

In Figure 4.5 I superimposed the two wavelets I will use, i.e., 25 Hz Ricker and the corresponding Ormsby. Both the main lobe and the two first side lobes are nearly identical, for the Ormsby and the Ricker. The Ormsby wavelets will have a time range of -200 ms to 200 ms, chosen to match the values in the paper by Ryan (1994), while the 25 Hz Ricker can have a cut-off at -40ms and 40ms, because the values for the Ricker are zero outside that range.

A Fourier Transform of the Ricker and Ormsby wavelets yields the values in the frequency domain, Figure 4.4, which determine the properties of the PSDM filter, so the frequency spectra is very interesting. Due to the relations between the domains, the energy in the side lobes of the Ormsby wavelet which gradually approaches zero yields a steeper shape in the frequency spectrum than the Ricker wavelet. The values in the Ormsby is constant over a wider band, but with a lower high frequency than the Ricker wavelet, which has generally lower amplitudes around its dominant

frequency. These characteristics are visible in the PSDM filter I generated with an average velocity of 3.15 km/s in Figure 4.6.

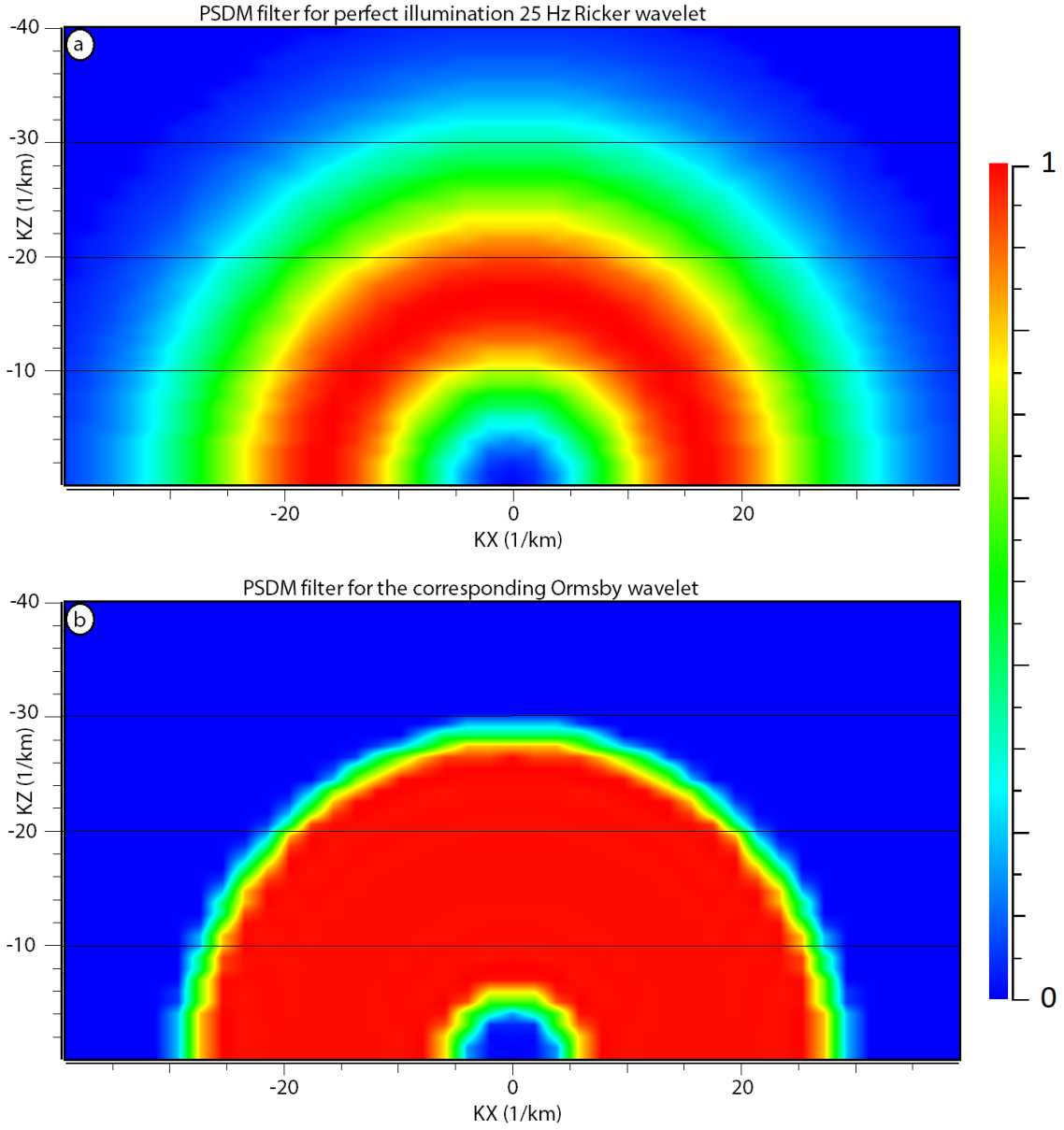

Figure 4.6: *The PSDM filters from (a) Ricker and (b) Ormsby wavelets.*

In Figure 4.6, the PSDM filters are based on the same survey, and the target point is perfectly illuminated, so the illumination angle is 180 degrees regardless of wavelet choice, but due to the frequency spectrum of the Ormsby, the PSDM filter for the

Ormsby wavelet has a significantly shorter wavenumber band than the PSDM filter from the Ricker wavelet. Also, the abrupt increase and decline of the values in the Ormsby frequency spectrum is visible in the PSDM filter. The Ricker-generated PSDM filter, however, has a much smoother shape due to its frequency spectrum having smoother transitions than the Ormsby.

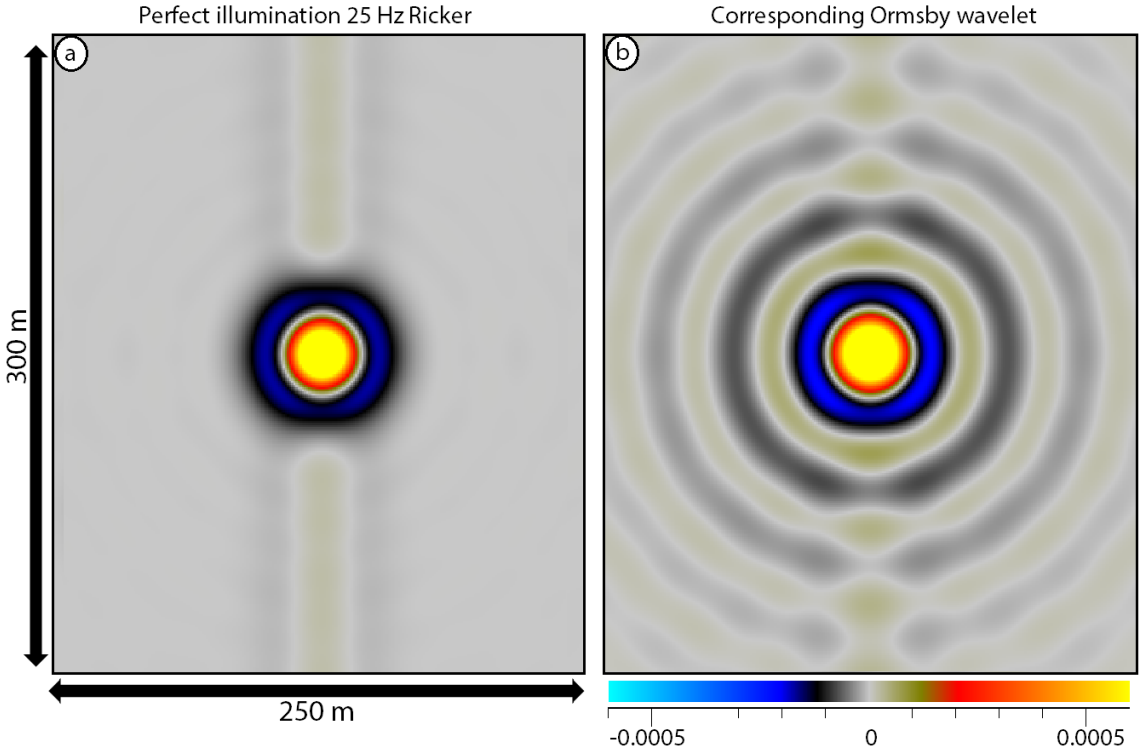

Figure 4.7: *The 25 Hz PSFs generated using (a) Ricker and (b) Ormsby wavelets.*

Both the Ricker and Ormsby PSFs have some vertical noise in the centre part, this is because of the horizontal cut-off in the PSDM filters at Kz=0 (turning waves not considered). They also have a similar main peak, but as explained before, a smaller PSDM filter gives a wider PSF (less resolution). This is the case for the Ormsby wavelet generated PSF, Figure 4.7.b, where the min part is slightly larger than that of the Ricker, due to the more limited wavenumber band of its PSDM filter. In addition, the Ormsby PSF has circular noise around the centre. This is truncation effects, due to sharp transitions at the frequency-band extremities for the Ormsby spectrum, while the Ricker spectrum is a smooth function. The sharp sides of the Ormsby filter then generate side lobes along each illumination vector direction, hence the spherical ringing pattern observed in Figure 4.7.b. To study

the effects on a reflectivity model I used a 2D wedge model, Figure 4.8 which will be studied again at a later stage.

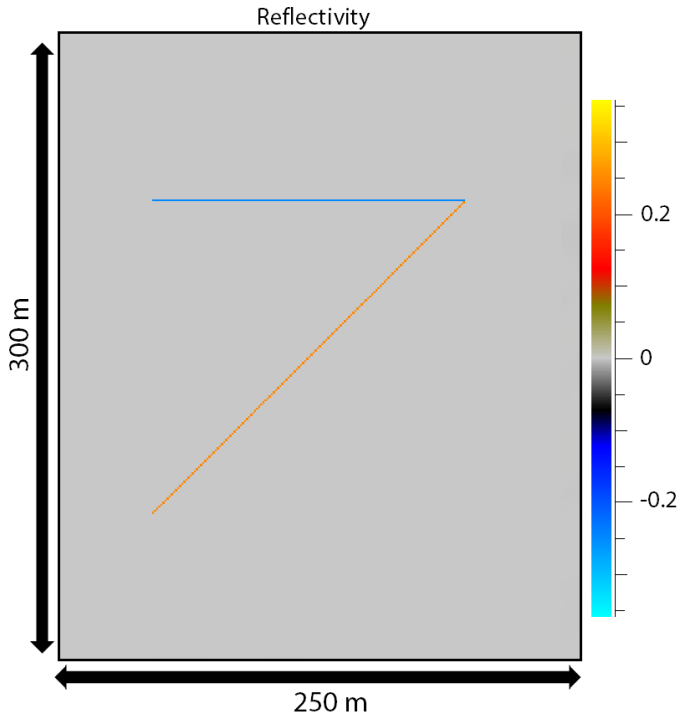

Figure 4.8: *2D wedge model, where the length and maximum wedge thickness is 150 metres, with a dip angle for the dipping reflector of 45°.*

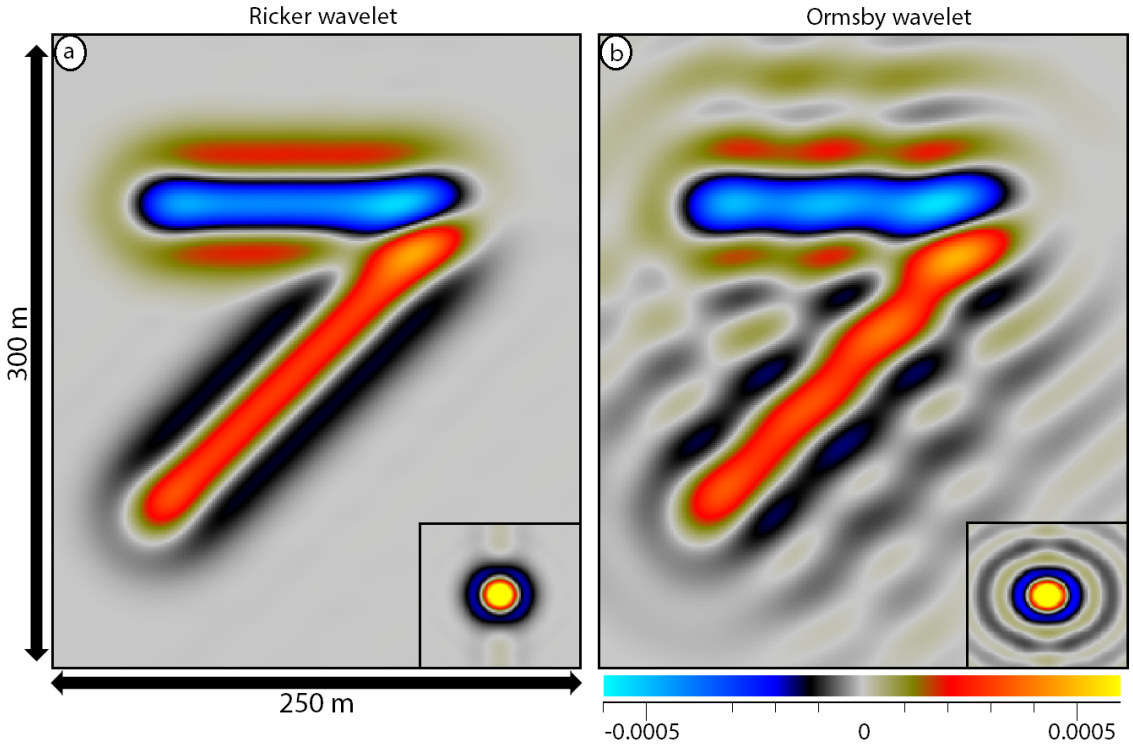

Figure 4.9: *The wedge model convolved with (a) the Ricker-generated PSF, (b) the Ormsby-generated PSF. Both PSFs are calculated for a 25 Hz dominant frequency, and perfect illumination case, which means that they have a 180-degree illumination range, and thus no cross-patterns. The superimposed PSFs are not to scale, see Figure 4.7.*

In Figure 4.9 the circular noise in the Ormsby case is significant, to the point where both the dipping and horizontal reflector will have an uneven shape at the wedge, due to the noise of the upper and dipping reflector having a constructive and destructive effect on each other, and thus altering the shape of the reflector in the seismic.

4.3 2D modelling: wedge model

As previously stated, 1D convolution modelling is the standard convolution modelling method. The advantage of this method is its efficiency, and it can predict reasonably well vertical resolution effects. It cannot, however, predict lateral resolution effects, which are often ignored or neglected. This causes the apparent lateral resolution for 1D modelling in 2(3)D cases to just be the size of the lateral sampling

of the model, i.e., no lateral dependency of the modelled seismic response and a sampling-dependent effect, Figure 2.14. A classic example used when modelling vertical resolution effects is the wedge model, but these wedges do not only occur in the vertical plane, lateral wedges also exist (e.g. fluvial channels) and lateral resolution effects on such should be studied too. Even in the case of a vertical wedge, as the 1D modelling method has a (false) lateral resolution of a sample, such wedge may not be modelled realistically, since the effects from a laterally near reflection event would not influence the seismic at all.

The lack of lateral resolution is studied later, with three models, the 2D Franklin Mountains and Beckwith Plateau outcrops and the 3D Setergrotta model. As the two convolution methods also has differences in vertical resolution, I will study their vertical resolution using a classic wedge model. The three cases compared here for the simple wedge model are the 1D convolution method, represented by a "1D PSF", and the 2(3)D convolution method represented by a perfect illumination PSF and a PSF with a maximum illuminated dip of 45°.The wedge model in figure 4.10 is inspired by Magee et al. (2015) with similar properties; "Sandstone: V_p = 3.9 km/s, ρ= 2.24 g/cm^3), shale: (V_p = 2.41 km/s, ρ= 2.19 g/cm^3)". I defined the host rock as a sandstone, and the intrusion as shale. The wedge is relatively small, with a length and maximum thickness of 150 metres, and a dip angle for the dipping reflector of 45°.This is a larger angle than commonly used in other wedge models, e.g. Magee et al. (2015). This is because I believed this would result in more significant differences than one with a low angle. I also used a low frequency wavelet, a 20 Hz Ricker wavelet, for the same reason. As the velocities in the model vary from 2.41 km/s to 3.90 km/s, I set the average velocity as 3.15 km/s when generating the PSDM filter.

The theoretical tuning thickness is calculated with equation 2.8, where the wavelength, λ, is given by the velocity of the intrusion, 2410 m/s, divided by the frequency of the wavelet. For the 20 Hz wavelet the tuning thickness of 30 m.

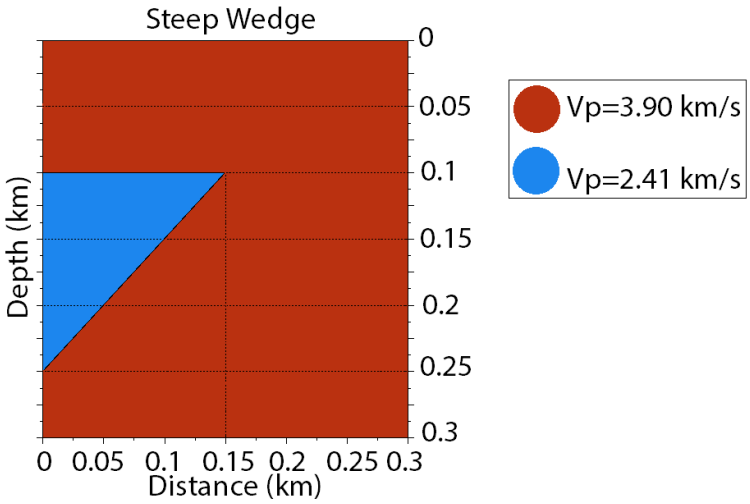

Figure 4.10: *The wedge model illustrated by its P-velocity.*

The resulting 2D reflectivity model is the same as in Figure 4.8, which consists of two different polarities, where blue is negative and red is positive. The model has a sampling of 1 m in both directions.

In Figure 4.11 a-c) the three convolution PSFs are illustrated in a variable density seismic plot type, while d-f) show their central trace only in wiggle form, this to better study the differences between the operators. For the two PSFs, there are originally wiggles on both sides of the central one. The figure illustrates significant differences, especially between the 1D wiggle (d) and the perfect illumination (e) case, as the perfect illumination PSF has a broader main lobe, and smaller side lobes than 1D, but it has a vertical band where the 1D has zero values. The 45° max-dip PSF wiggle (f), however, is more like the 1D, with broader side lobes and a narrower main lobe. It also has some lobe effects after the side lobes.

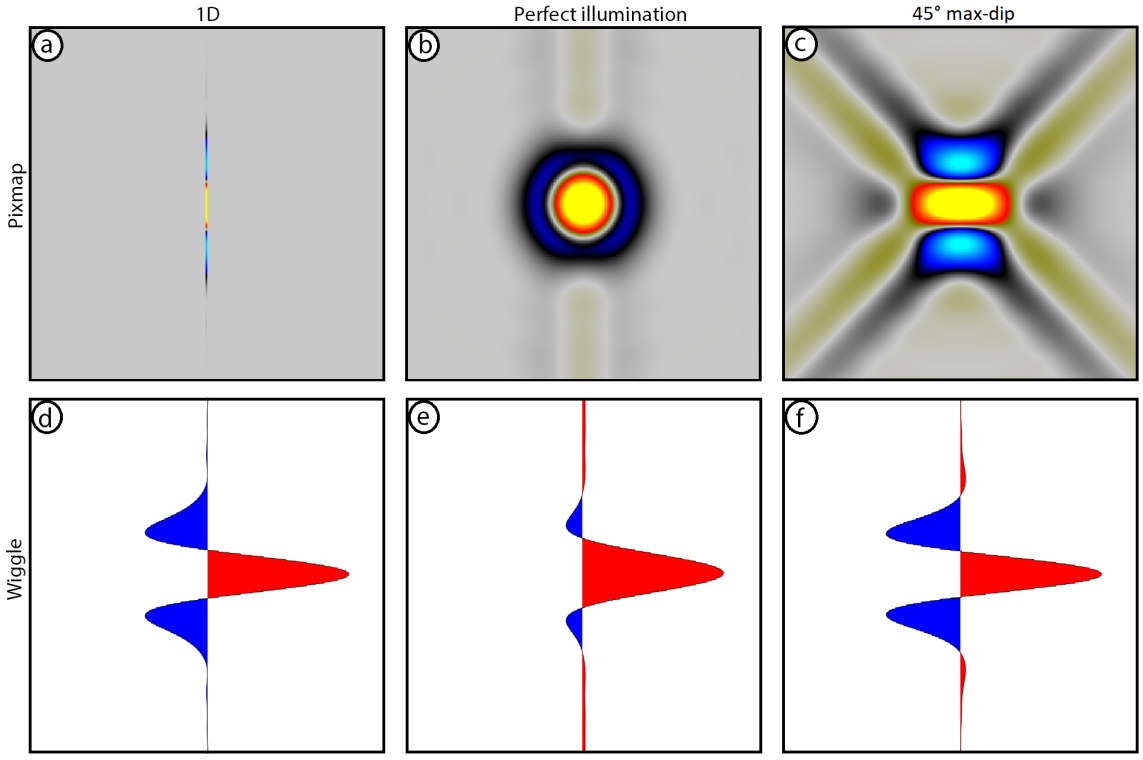

Figure 4.11: *Comparing three convolution PSFs, (a)1D "PSF", (b) Perfect illumination PSF, (c) 45° max-dip PSF in pixmap (a)-(c), and wiggle the central trace (d)-(f).*

The first step is to calibrate the amplitudes because the amplitudes in the modelled seismic will not directly correlate with the original values in the reflectivity model (also true with real seismic, which needs to be calibrated at well prior to, e.g., AVO or seismic inversion). Also, since we utilize three different PSFs for the modelling, the energy will be distributed in different manners (i.e., the PSDM filters do not have the same area covered in the wavenumber domain). The 1D convolution has strong vertical amplitudes in that case, but they will not affect the amplitude strength of nearby reflectivity/diffraction points (having no lateral "thickness"), while the two other 2D PSFs will have a varying degree effects on the nearby reflections.

For the amplitude calibration, I generated a horizontal plane at the centre target depth with a reflectivity value of 1. This is done to remove other factors than the convolution methods (1D- and 2(3)D-PSF), and as a result we can find the differences in seismic amplitude due solely to the differences in PSF amplitudes. Modelling this plane with the different PSFs, I can read the peak values of the seismic at the calibration reflector for each case, thereby dividing the modelled seismic with

that value to get amplitude calibrated seismic results directly comparable to the input reflectivity.

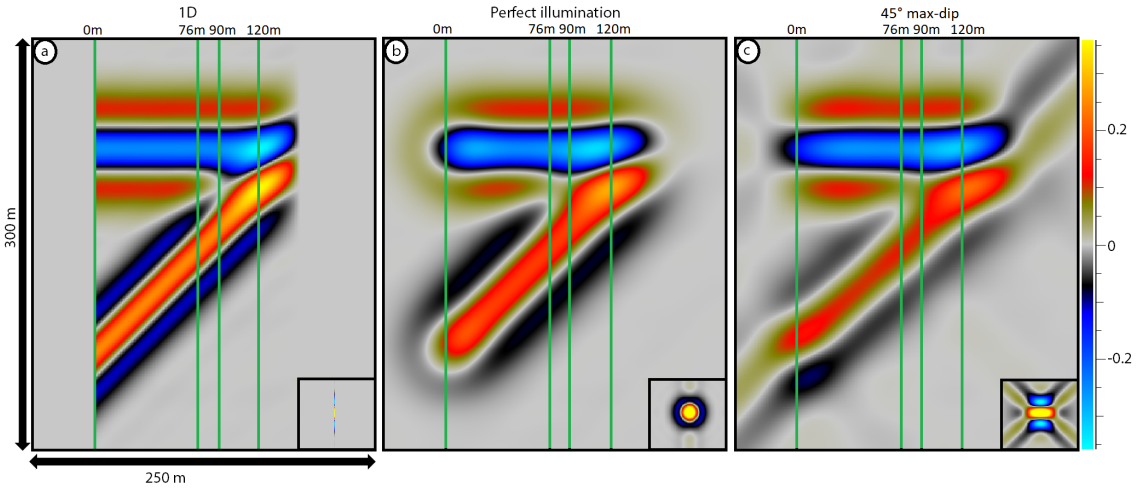

Figure 4.12: *The synthetic seismic generated for the reflectivity wedge model, with (a) 1D convolution, (b) a perfect illumination PSF, (c) a 45° max-dip PSF. Four lateral trace positions, i.e., 0 m, 76 m, 90 m and 120 m, are marked with green lines and are analysed as wiggle plots in a later figure. PSFs superimposed, not to scale.*

In the seismic, Figure 4.12, four points of interest at 0, 76, 90 and 120 m are marked with green lines where I extracted the corresponding wiggle plot for a detailed analysis. Theoretically, the tuning thickness is when the distance between the two layers is 30 m, which happens at 120 m in the model. After studying the model, I found other interesting locations to be towards areas where the two layers will also interfere, 76 m and 90 m, in addition to the start of the model, 0 m (Table 4.3).

Table 4.3: The notation of the locations of chosen traces

Notation	Location	Wedge thickness
A	0 m	150 m
B	76 m	74 m
C	90 m	60 m
D	120 m	30 m - Tuning Thickness

Figure 4.13 illustrates the location A and B. At location A, 0 m, the 1D convolution illustrates two mirrored versions of the 20 Hz Ricker wavelet, symmetric with opposite polarities, and they do not interfere. This is not the case for the PSFs, where for (b) Perfect illumination, the side lobes for the dipping layer reflector are not symmetric, and the highest side lobe has energy all the way up to the upper reflector due to interference. This is like (c) 45° max-dip PSF, but contrary to (b),

there is more energy in the bottom side lobe than in the highest one for the dipping reflector, again due to interference.

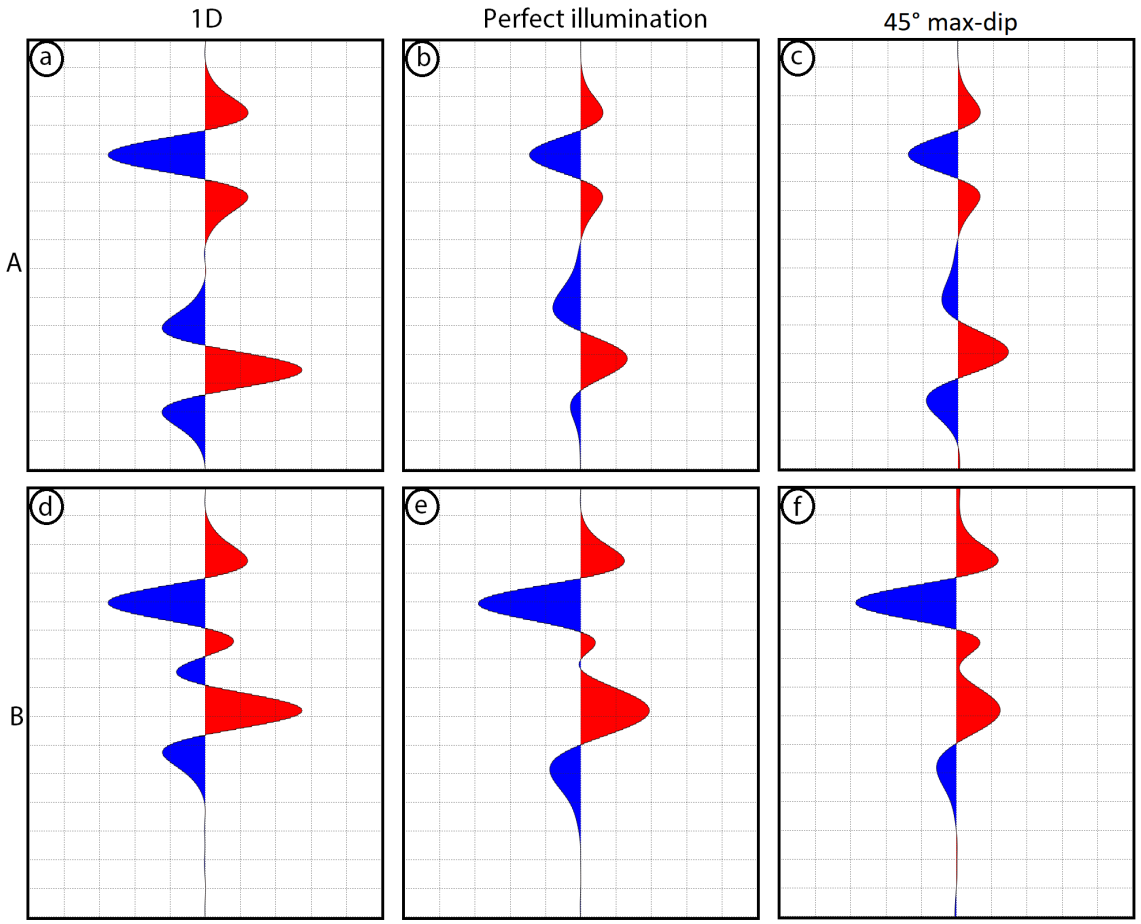

Figure 4.13: *Traces for three convolution operators (left: 1D; middle: perfect illumination; right: 45° max-dip) Wedge thickness: Location A: a-c: 150 metres and location B: d-f: 74 metres.*

Figure 4.13, Location B is where the upper side lobe of the dipping reflector disappears in the case of a perfect illumination PSF, e). However, in the 45° max-dip PSF, f), the positive side lobe has already been removed, and the negative side lobes in the mid part have begun affecting each other. In the 1D case, there is still symmetry, and the three traces have similar amplitudes for the horizontal reflector, excluding the bottom side lobe.

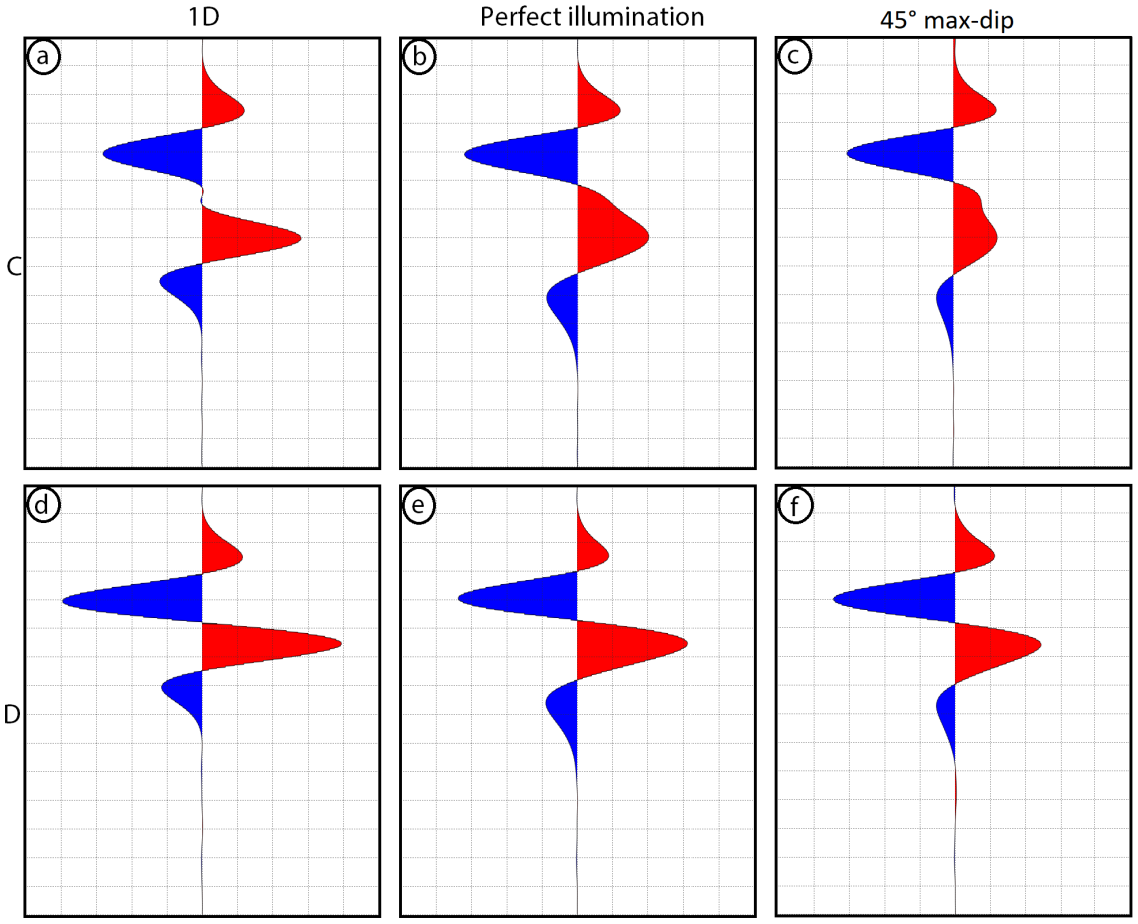

Figure 4.14: *Traces for three convolution operators (left: 1D; middle: perfect illumination; right: 45˚ max-dip) Wedge thickness: Location A: (a)-(c): 60 metres and location B: (d)-(f): 30 metres.*

In Figure 4.14, location C, the 1D convolution, (a), has approximately zero value between the two main lobes, which means that the interference of the side lobes has started, and the two main lobes is about to interfere with each other. Interestingly, in the cases generated with 2D PSFs, the dipping reflector main lobe has a new shape because it is affected by the side lobe of the horizontal reflector. This thick main lobe means a significantly worse resolution for the 2D modelling cases than the 1D case. There are also some differences between (b) and (c), where the amplitudes are generally higher everywhere for the perfect illumination case, (b). The main lobe of the horizontal layer in case (c) is also somewhat narrower than the two others, and there is energy above the upper side lobe.

The final case, Figure 4.14 D), is at 120 metres, which is where the distance between

the two reflectors is 30 metres, the tuning thickness. At this location the main lobes and bottom side lobe of the dipping reflector is significantly thicker for the 2D PSFs than the 1D case, and the amplitudes are significantly higher in the 1D than for the 2D PSFs.

In Figure 2.6, the tuning thickness is illustrated using an amplitude plot. This is interesting to perform for this case, i.e., to study how the tuning thickness of the model differs with the convolution methods. In contrast to the wedge model from Simm and Bacon (2014), Figure 2.6, in this model the horizontal reflector is negative, and the wedge is in the opposite direction, causing the amplitude figure to differ from the example from Simm and Bacon (2014), i.e., the tuning thickness will be illustrated by the lowest point of amplitude in the figure. Since the reflector is negative, an increase in amplitude value is downwards in the figure.

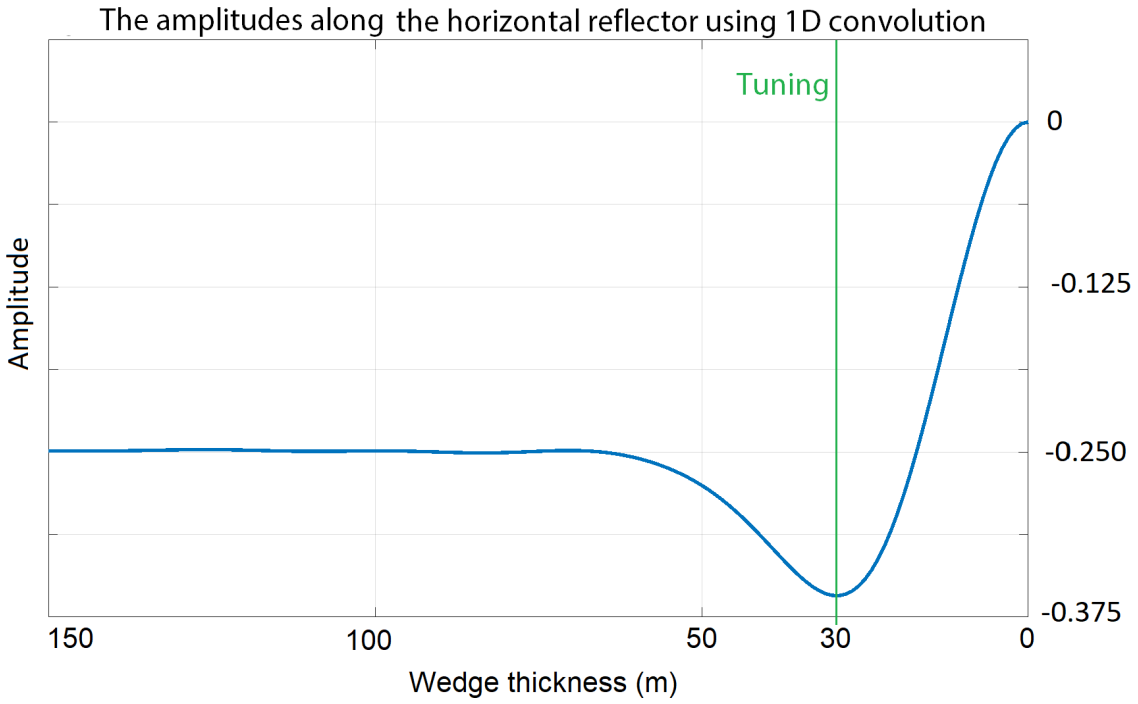

Figure 4.15: *Amplitudes along the horizontal layer using 1D convolution, with the tuning at 30 m wedge thickness highlighted in green.*

Figure 4.15 illustrates the first amplitude extraction for the 1D convolution, where the tuning thickness is where the wedge is 30 m thick, which coincides with the calculated value. The amplitudes of the dipping layer do not affect the horizontal reflector until about the thickness is about 70 m, and at the end of the modelling case, the amplitude value is zero. This means that the apparent thickness of the horizontal

reflector is zero when the wedge thickness is zero. Figure 4.15 also illustrates how the amplitude calibration should work, as without interference it is stable at -0.250, which is the amplitude value of the reflector.

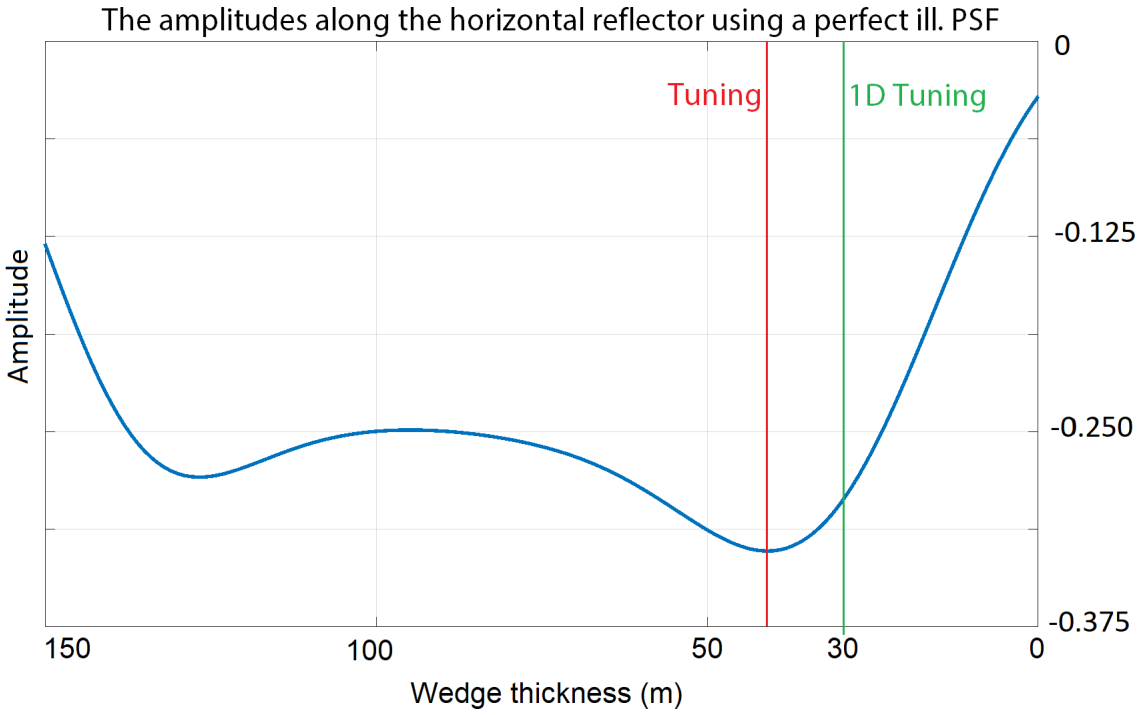

Figure 4.16: *Amplitudes along the horizontal layer using a perfect illumination PSF, with the tuning at a wedge thickness of 41 m highlighted in red, and the 1D convolution tuning thickness in green, for reference.*

The tuning thickness for the perfect illumination PSF case is located at a wedge thickness of 41 m in Figure 4.16. This means that the vertical resolution is about 1/3 worse than for the 1D convolution in this case. Also, the amplitudes will generally differ more than for 1D, with the side lobes of the wavelets of the surrounding reflection points interfering in the seismic.

This is especially noticeable at the start of the reflector, where lower amplitude values are the result of fewer adjacent reflection points (since there is no reflectors beyond 150 m wedge thickness). The 2D PSFs lateral resolution effects makes the adjacent amplitudes stronger, as the horizontal reflection points have a constructive effect on each other. Hence an increase in negative amplitude values until it stabilizes at -0.250, the value of the reflector.

When the interference starts, the side lobes of the reflectors have constructive in-

terference with each other, which causes the amplitude values to increase until the tuning thickness. At this point the seismic of both reflectors starts to bend together, which causes the amplitudes at the reflector to decrease. I have compiled the observed effects on the amplitude values in a list in the discussion, Chapter 5.

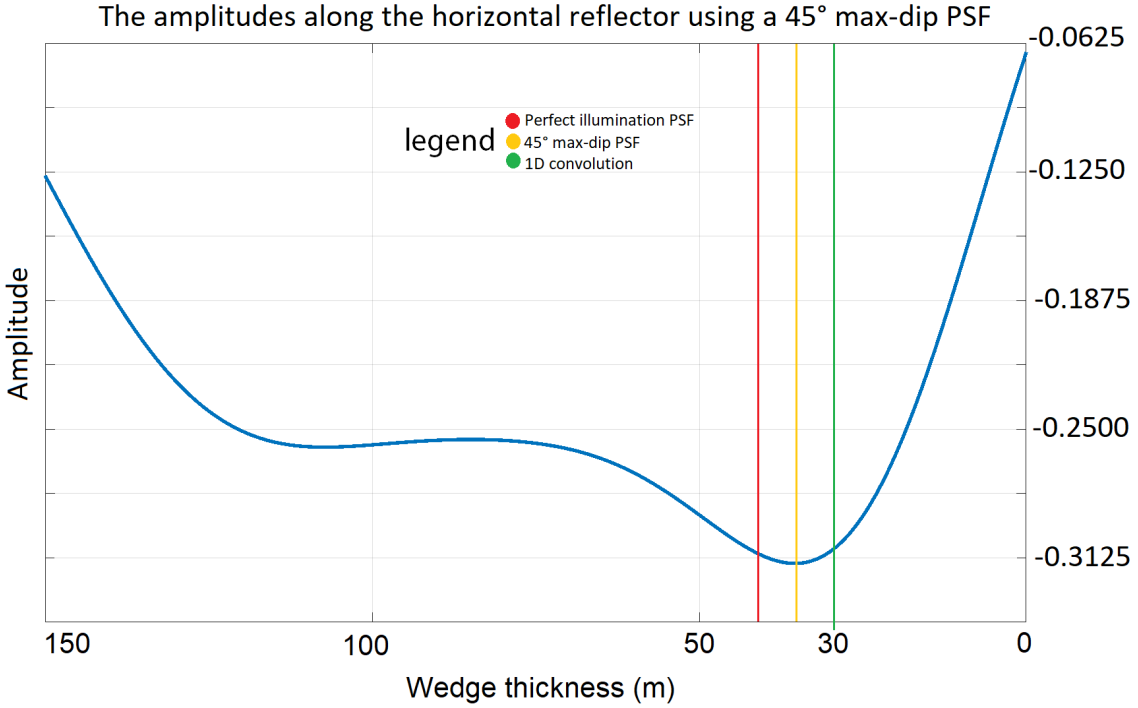

Figure 4.17: *Amplitudes along the horizontal layer using a 45° max-dip PSF, with the tuning at a wedge thickness of 35 m highlighted in orange. The 1D convolution and perfect illumination PSF tuning thickness in green and red, respectively.*

In Figure 4.17, where a 45° max-dip PSF was used, the amplitudes does not stabilize at the reflector amplitude value, this might be due to a the dipping reflector not being fully resolved. The tuning thickness, however, is at 35 m wedge thickness. This is approximately in the middle of the 1D convolution and perfect illumination PSF. This shows that even though the lateral resolution effects are the main difference between the results, the 2(3D) PSF-based modelling method also impacts the vertical resolution.

4.4 2D modelling: Franklin mountains paleo cave

As an example of a 2D modelling of a more realistic geomodel, I chose an outcrop-based one, i.e., paleo caves in the Franklin mountains, where the main cave is named The Great McKelligon Sag (GMS), which consists of collapsed material (Målbakken, 2009). Modelling this cave is interesting due to its many facies, steep layers and nearby paleo cave structures with high acoustic impedance. This model was made by Johansen (2018), where the values of the model are based on rock physics assumptions. I use this model from Johansen (2018) to especially study 1D/PSF-based convolution modelling. I refer to Johansen (2018) for further details on seismic modelling of various paleokarst models.

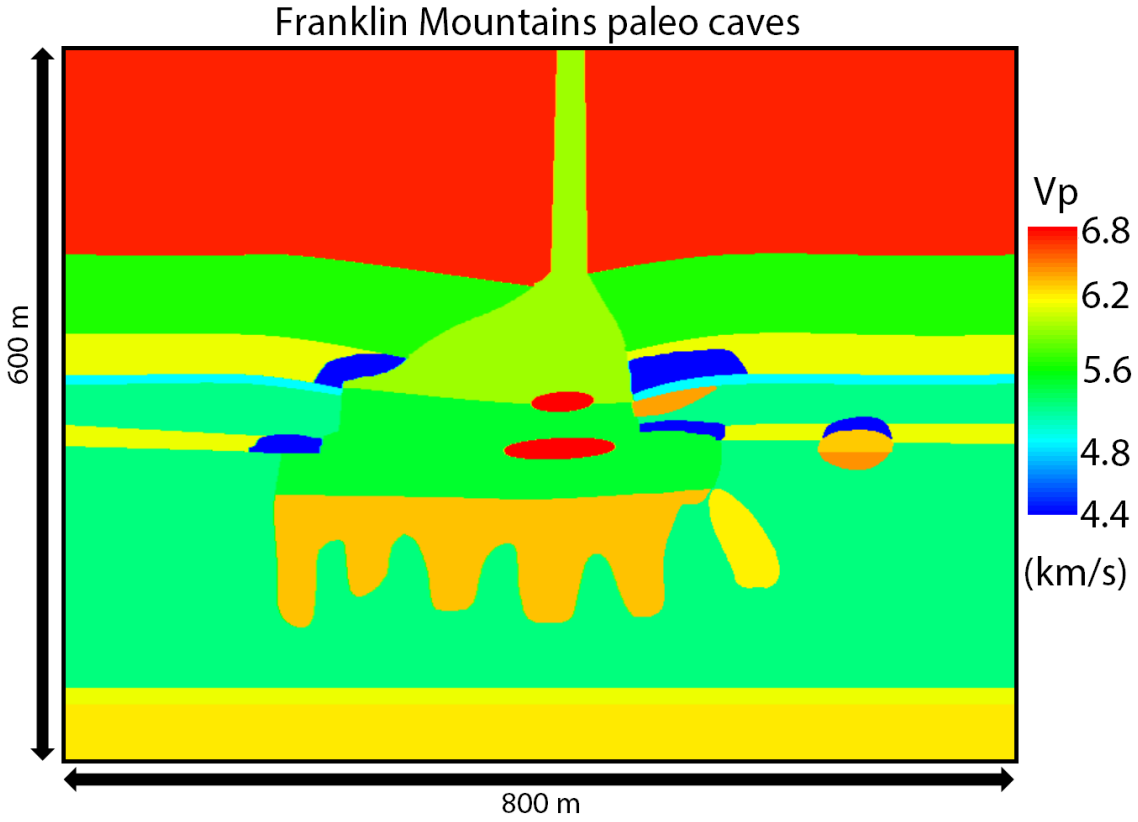

Figure 4.18: *The Great McKelligon Sag along with other paleo cave structures, illustrated by its P-velocities. Model courtesy of Johansen (2018).*

The 2D model consists of a background layered medium with varying P-wave velocities, and the paleo cave units consisting of the GMS and a smaller elliptical cave located to the right of the GMS. The GMS consists of a folding shape at the bottom

of the cave, a pipe-like feature at the top, some high velocity pockets inside the cave, and low velocity fracture components located at the side of the GMS. A similar low porosity fracture component is also present above the smaller cave.

In this model, both caves are modelled as oil-saturated, including the low-velocity fracture components at both sides of the GMS and above the smaller cave, while the background layers around the caves are brine-saturated. Due to their complex nature, these karst structures tend to be difficult to model and interpret. I chose a fine sampling of 50 cm in each direction, a 30 Hz Ricker wavelet and an average velocity of 5.6 km/s. The results were amplitude calibrated according to the reflectivity model.

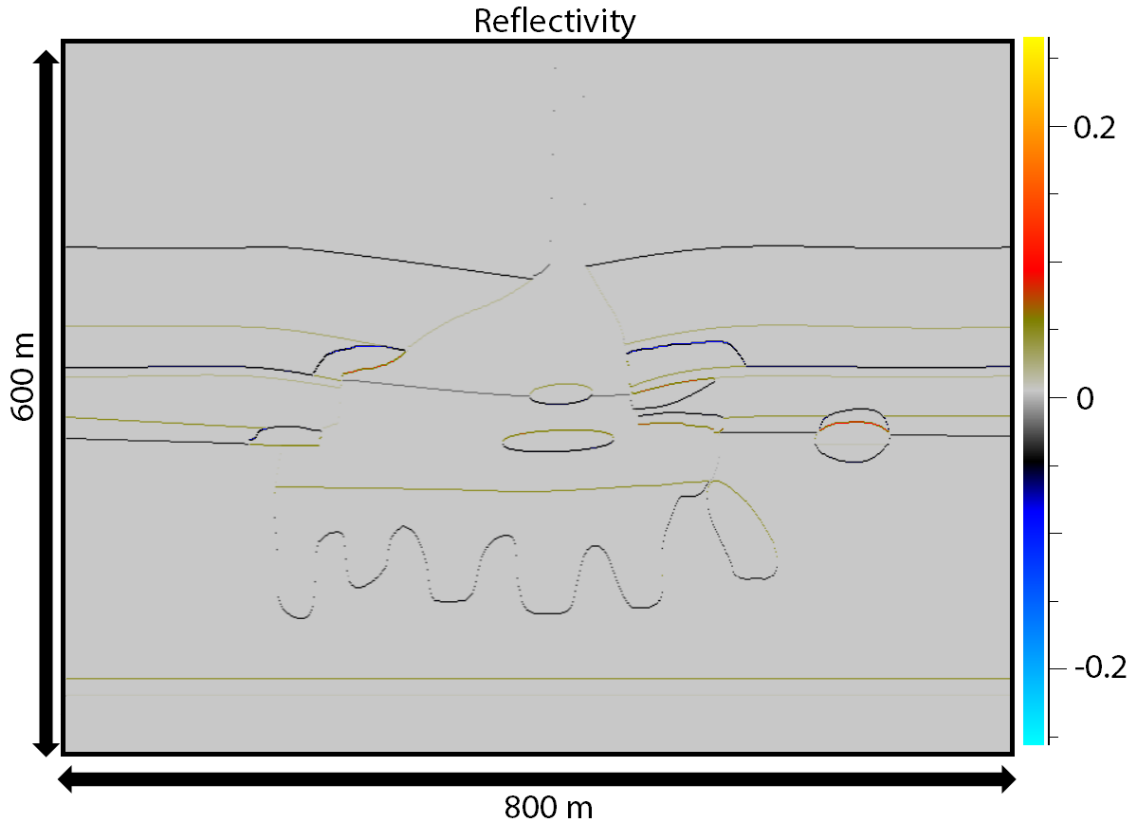

Figure 4.19: *The 2D Franklin Mountain reflectivity model.*

The reflectivity model, Figure 4.19, reveals generally weak reflectivity in the roof and outline of the GMS, especially the walls of the middle layer, where the reflection coefficient is close to zero. The steep nature of the bottom of the cave, where there is a "folding" shape, is represented by few isolated point scatterers due to an intrinsic limit in the code extracting reflectivity in SeisRoX (only along vertical depth lines),

which is not proper for seismic modelling of such steep structures. This causes an aliasing of steep structures which gives a pattern of isolated point scatterers for steep structures. This is also the case for the pipe, which is represented by few and weak reflection points. The strongest reflections are located at the fracture lobes on the side of the main cave and the adjacent smaller cave, in addition to strong reflections at the pockets inside the GMS.

Unfortunately, because of the aliasing in the steep-reflectivity issue in SeisRoX, which causes the reflector to be discontinuous, I cannot conclude much from the "folding" structures, which is the most eye-catching effects in the model. There is, however, other structures in the model which can be studied.

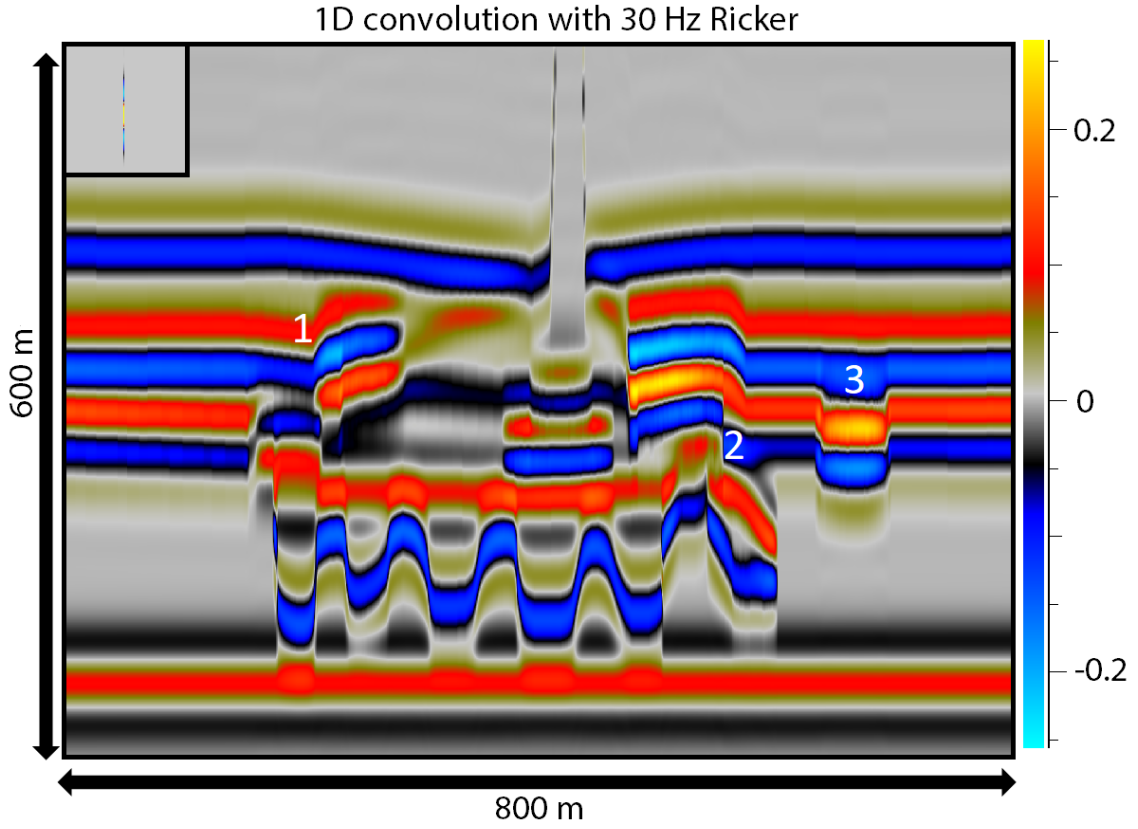

Figure 4.20: *The Franklin mountain paleo cave modelled with 1d convolution for a 30 Hz Ricker wavelet. Some key locations, from left to right, marked with 1,2,3. Superimposed PSFs not calibrated.*

Figure 4.20 is the modelled caves with 1D convolution. In this 1D modelling case with near-vertical "folds", there are many areas with apparent thinning of the layers

(even in zones where steep reflectors were properly represented in the input reflectivity grid). This happens because 1D convolution modelling cannot consider lateral resolution effects in the model. In some areas this thinning is so extreme, that the reflectors can be interpreted as faults. This happens at both ends of the "folds" at the bottom of the main cave, but it is partially due to the "steep-reflectivity" issue.

The lack of lateral resolution is also visible in other key locations, as with the adjacent smaller cave (location 3), which could easily be interpreted as a graben structure. Another location is at the fracture components in location 2, where the sudden dip of the fracture components causes apparent thinning of the reflectors. This also happens at location 1, where there is a sudden fracture-like artefact. As for amplitudes, the highest values are at the low-velocity fracture lobes.

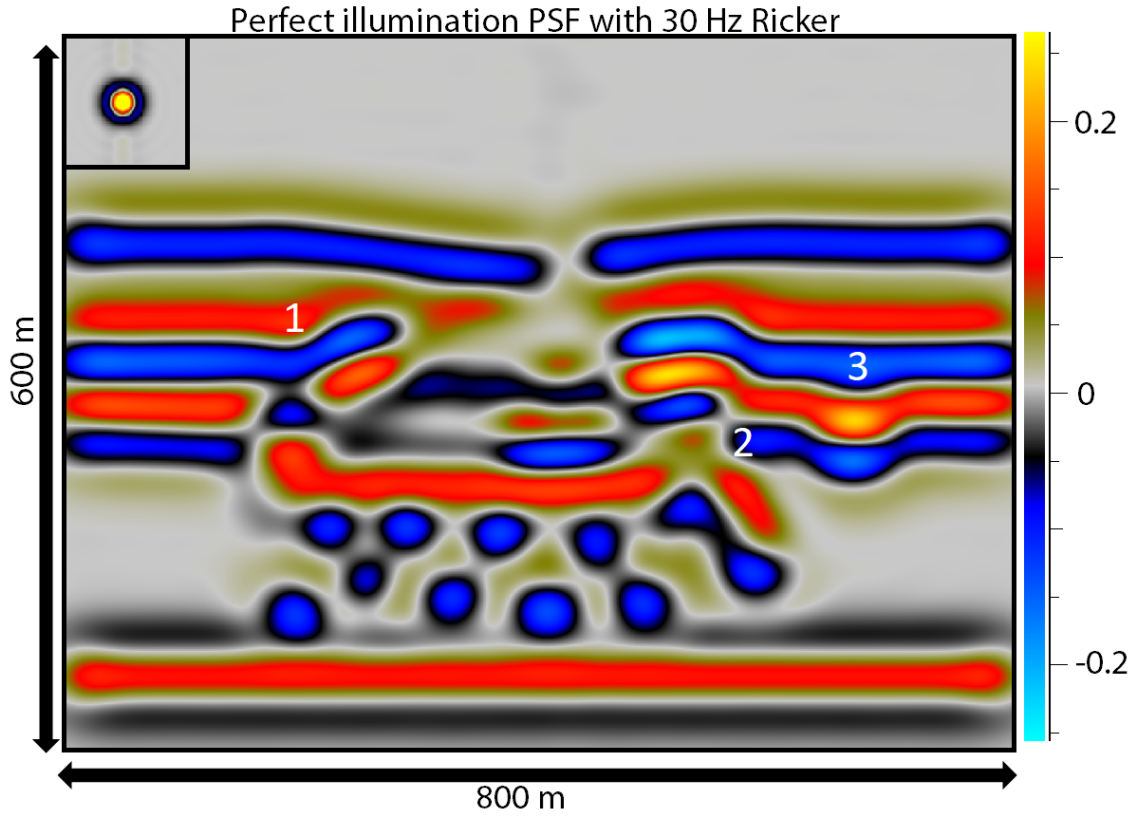

Figure 4.21: *The Franklin mountain paleo cave modelled with a perfect illumination PSF for a 30 Hz Ricker wavelet. Some key locations, from left to right, marked with 1,2,3. Superimposed PSFs not calibrated.*

At a frequency of 30 Hz, the Figure 4.21 illustrates the difficulties in imaging high velocity paleo caves, as there is a lot of discontinuous layers, causing the seismic

energy to be spread across layers. However, the general shape of the cave is possible to interpret. One may also interpret the smaller cave (location 3), but this is not trivial. In locations 1 and 2, the abrupt apparent thinning from the 1D model is smoother, and the "fault-like" artefacts are gone. Again, the highest value amplitudes are due to the low-velocity fractures present on the side of the main cave, in addition the high-velocity layers in the main cave are well illuminated in the model.

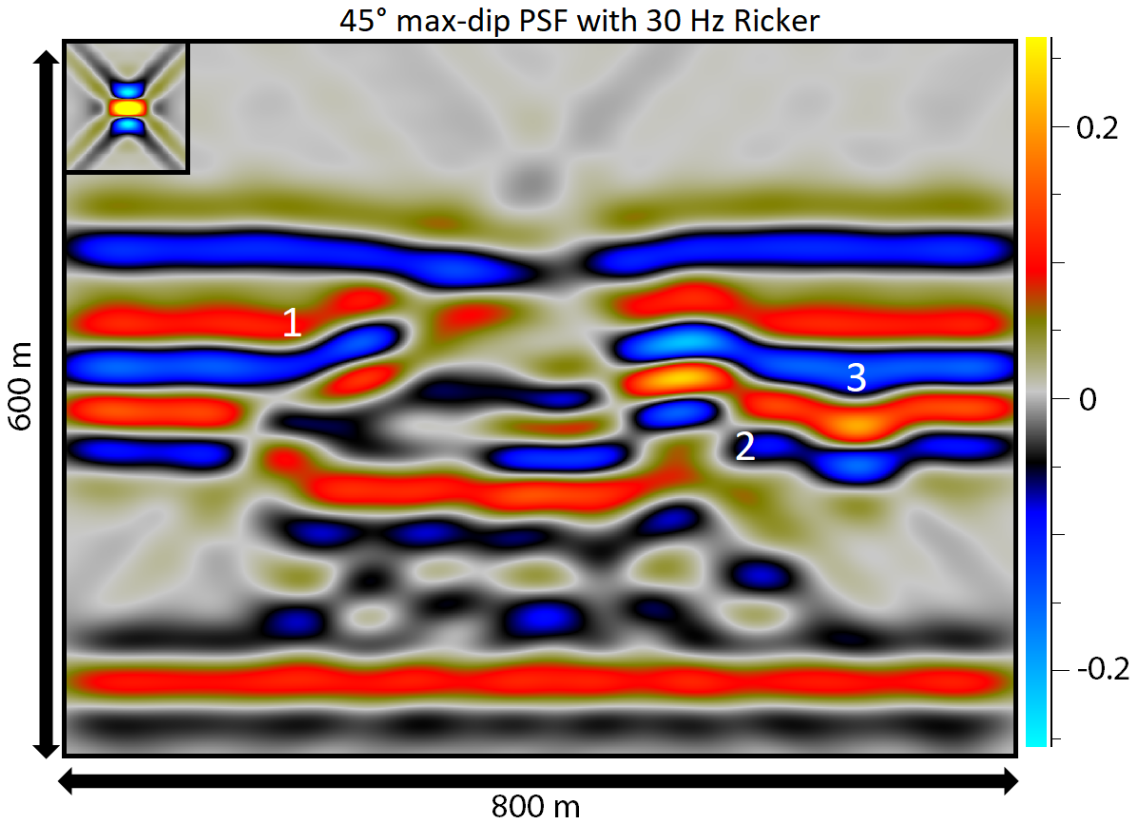

Figure 4.22: *The Franklin mountain paleo cave modelled with a 45° max-dip PSF for a 30 Hz Ricker wavelet. Some key locations, from left to right, marked with 1,2,3. Superimposed PSFs not calibrated.*

To study the modelling with an illumination-limited PSF, I also modelled with a 45° max-dip PSF in figure 4.22. As explained in the Survey effects chapter, the 45° max-dip PSF is not able to illuminate events steeper than 45°İn this model there are several structures steeper than that limit, even if we ignore the extremely steep areas poorly represented by the improper gridding function in the bottom "fold"-area of the GMS.

Due to the lateral smearing effect introduced by the poorer lateral resolution (com-

pared with Figure 4.21), these steep reflectors will not be illuminated. With seismic energy being spread laterally, the target model appears to have a gentler shape. This is apparent in all three locations of interest, in addition to the highest reflector, where the gap over the GMS is filled. However, structures with a lower angle than 45° is illuminated, and the shape and structure of the main cave is illuminated without the artefacts caused by 1D convolution modelling, such as apparent thinning.

4.5 2D modelling: Beckwith Plateau

In the introduction, I illustrated seismic imaging using a sedimentary outcrop from Beckwith Plateau, Utah, USA in figure 1.1, courtesy of Friestad (2018). For a more in-depth discussion about seismic modelling of the Beckwith Plateau I refer here to Friestad (2018). This area consists of large-scale horizontal extensive beds, with little tectonic effects, meaning that there are few faults. However, the selected scope, figure 4.23, also consists of visible small-scale sedimentary architecture, such as thin high-velocity silt layers and low-velocity coal seams, in addition to some areas with steeper layers, up towards 90° in the middle part of the outcrop.

When modelling such thin layers, the modeller is faced with several options, i.e., one can choose whether to define these layers in great details, or to simply give them an average property considering that the expected resolution is not sufficient to see such "small details". When modelling this outcrop, Friestad (2018) and I made two cases where we defined the sandstones with silt layers differently; in the first case we defined each silt layer as illustrated in figure 4.23. In the second case we evaluated which of the two rocks (sandstone and silt) dominated the structure, the structure was then defined as one rock with the properties of the dominating one, thereby removing the dipping and horizontal layers inside it. For each case, I modelled using three, now familiar, methods; 1D convolution, and the 2(3)D convolution with perfect illumination PSF and a 45° max-dip PSF. After doing this, I made plots to study the variations between the outcrops with and without modelling the silt layers for each modelling method.

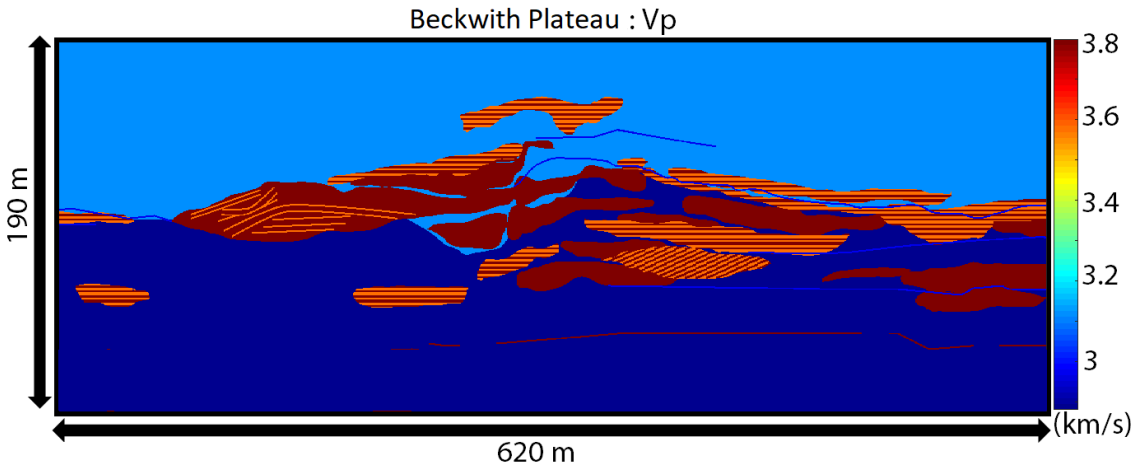

Figure 4.23: *The P-velocities of the Beckwith Plateau outcrop. High-velocity sandstone layers in orange with Vp=3.58 km/s.*

The P-velocities in the model range from 2.88 km/s to 3.8 km/s, in figure 4.23, with some steep contrasts (Friestad, 2018). The silt layers (3.58 km/s) are located inside higher velocity sandstone (3.8 kms/s), with minimal differences in porosity, resulting in a low acoustic impedance, and thus low reflectivity coefficient, illustrated in the reflectivity model (Figure 4.8). In other locations, the high-velocity sandstone is directly in contact with the low-velocity mudstone (2.88 km/s), which yields high reflection coefficients. The low-velocity coal layers generally generate low reflectivity coefficients, except when they cut the sandy parts of the model, where they increase velocity contrasts, and thus the reflections in those areas. The model was made with a sampling of 50 cm in each direction.

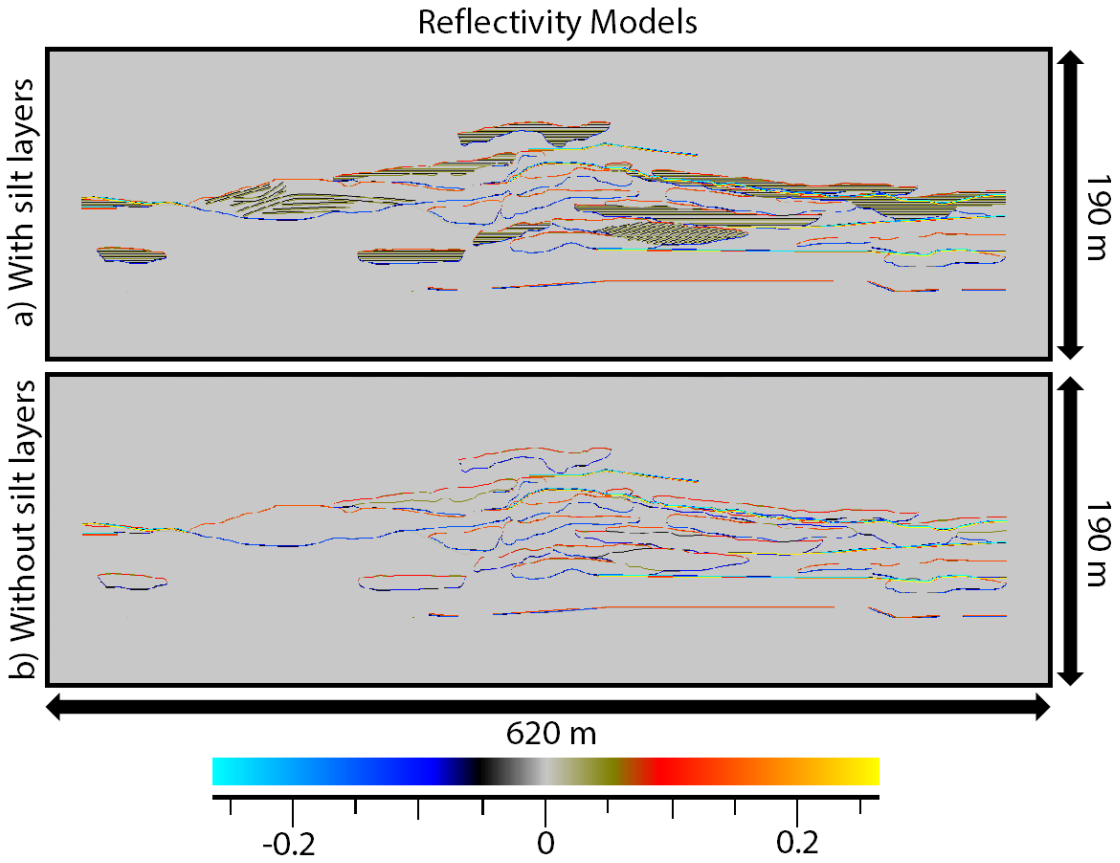

Figure 4.24: *The reflectivity model for the two cases (a) with silt layers, and b) without silt layers.*

The reflectivities in Figure 4.24 are generally strong for the structures in the model, including the thin coal layers, and the line of sand at the bottom of the model. In contrast to these, the silt layers have weak reflectivity, as expected. In this thesis, I focus on how the dipping layers are modelled with the convolution methods. Therefore, I have highlighted two interesting areas in the model where there are such dipping silt layers, Figure 4.25, with the dip ranges in Figure 4.26 and I will also study how the seismic in these locations alters with and without the layers, depending on the modelling method. This can also be a discussion of detectability.

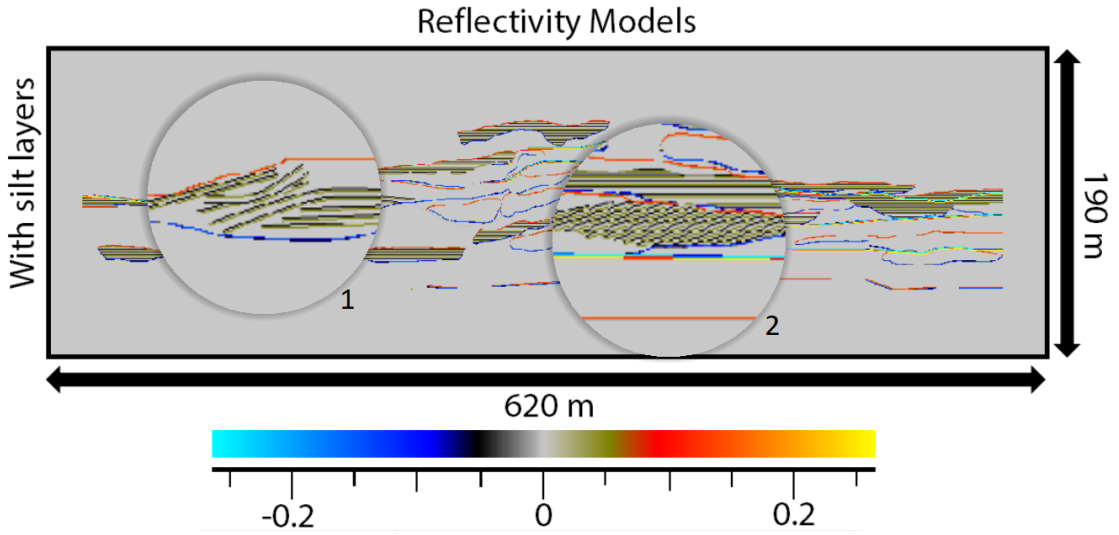

Figure 4.25: *The silt layer reflectivity model, with the two locations 1,2 where the dipping silt layers present is highlighted.*

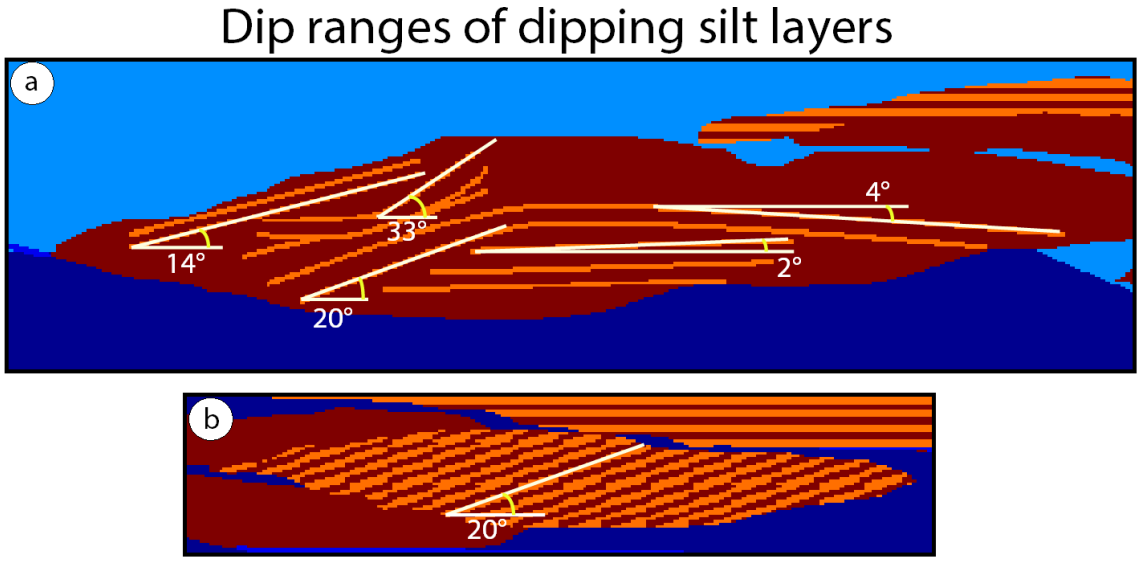

Figure 4.26: *The dips in the two locations 1,2 illustrated in a and b, respectively. The dip ranges from 2˚ to 33˚˙*

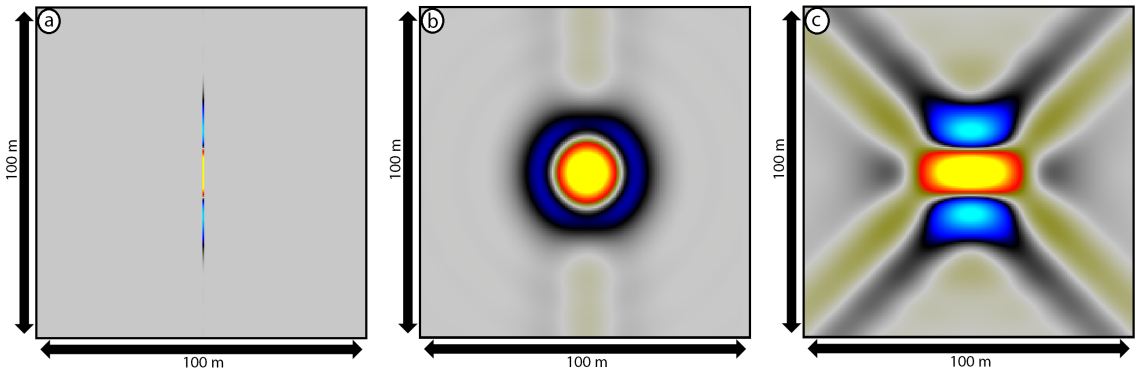

Figure 4.27: *The three convolution operators, (a) 1D wavelet, (b) Perfect illumination PSF, (c) 45° max-dip PSF.*

The results the amplitude calibrated seismic modelling after convolution with the PSFs in Figure 4.27 are presented in the following pages before comments. The 1D convolution results are in Figure 4.28, perfect illumination PSF in Figure 4.29, and the 45° max-dip PSF in Figure 4.30. For each modelling approach, the three rows are: (a) the model with the silt layers, (b) without the silt layers, and the third, (c), is the difference between the two to study the difference the silt layers makes. This enables the reader to compare the results from the operators by turning the pages in the .pdf-format. The seismic is, as for every case in this thesis, displayed with "no resampling" to avoid adding fake auto-interpolation. This is especially powerful in the 1D case. Please note that the PSFs in the following figures are not calibrated, nor to scale, see Figure 4.27.

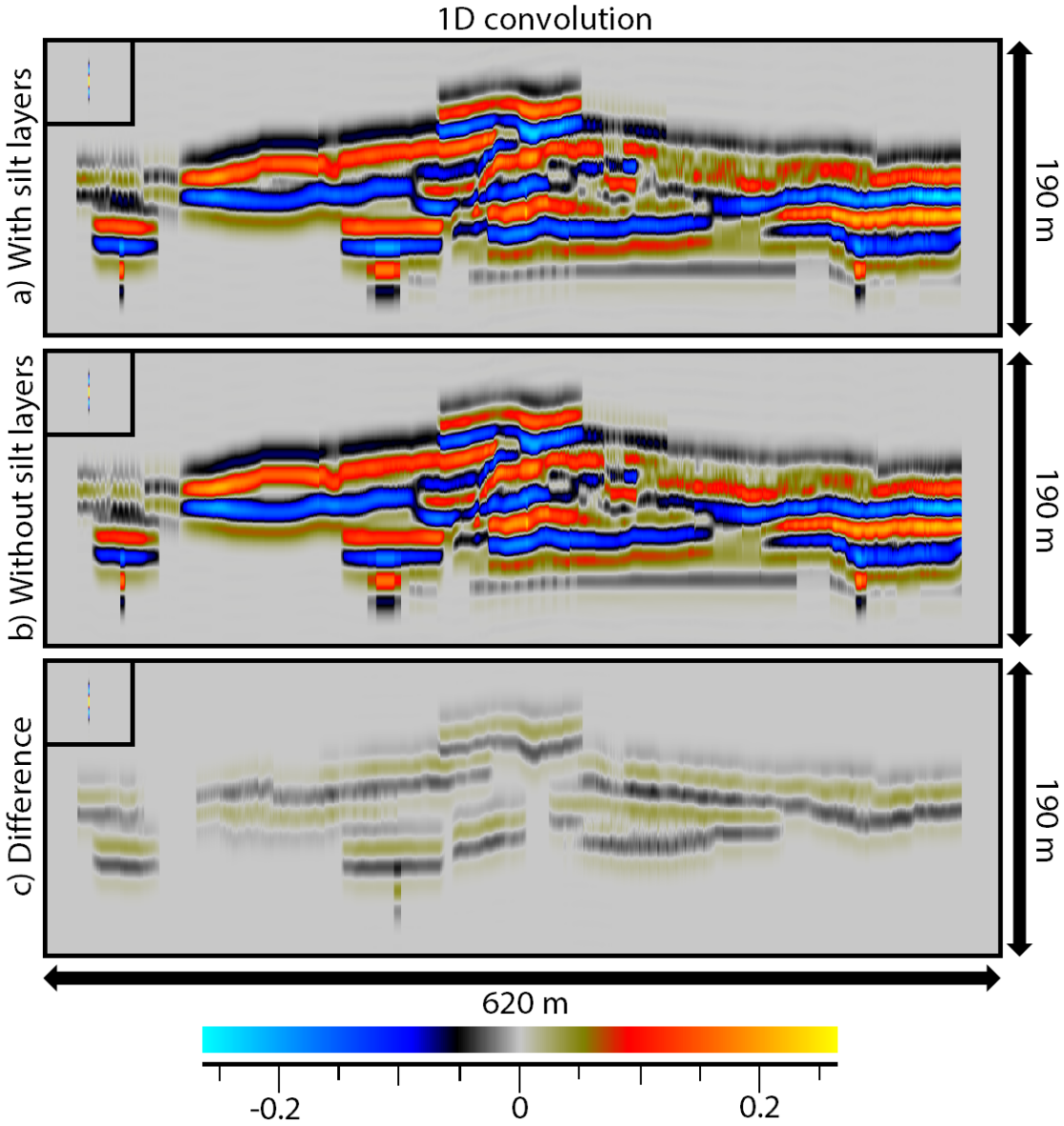

Figure 4.28: *The Beckwith Plateau outcrop modelled with 1D convolution. (a) The model with thin silt layers in the model, (b) without silt layers, (c) the difference between the two cases (a) and (b)*

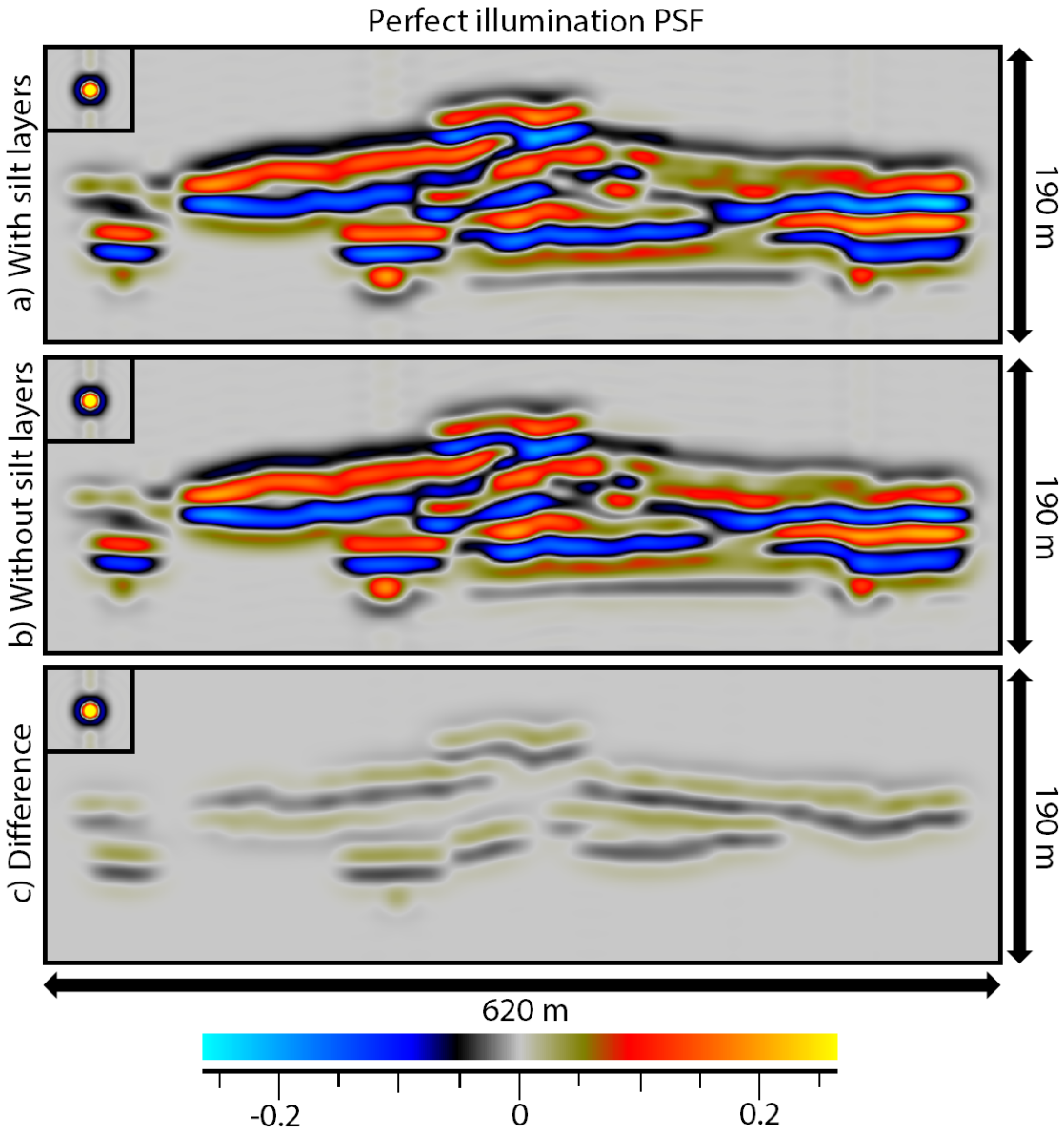

Figure 4.29: *The Beckwith Plateau outcrop modelled with a perfect illumination PSF. (a) The model with thin silt layers in the model, (b) without silt layers, (c) the difference between the two cases (a) and (b)*

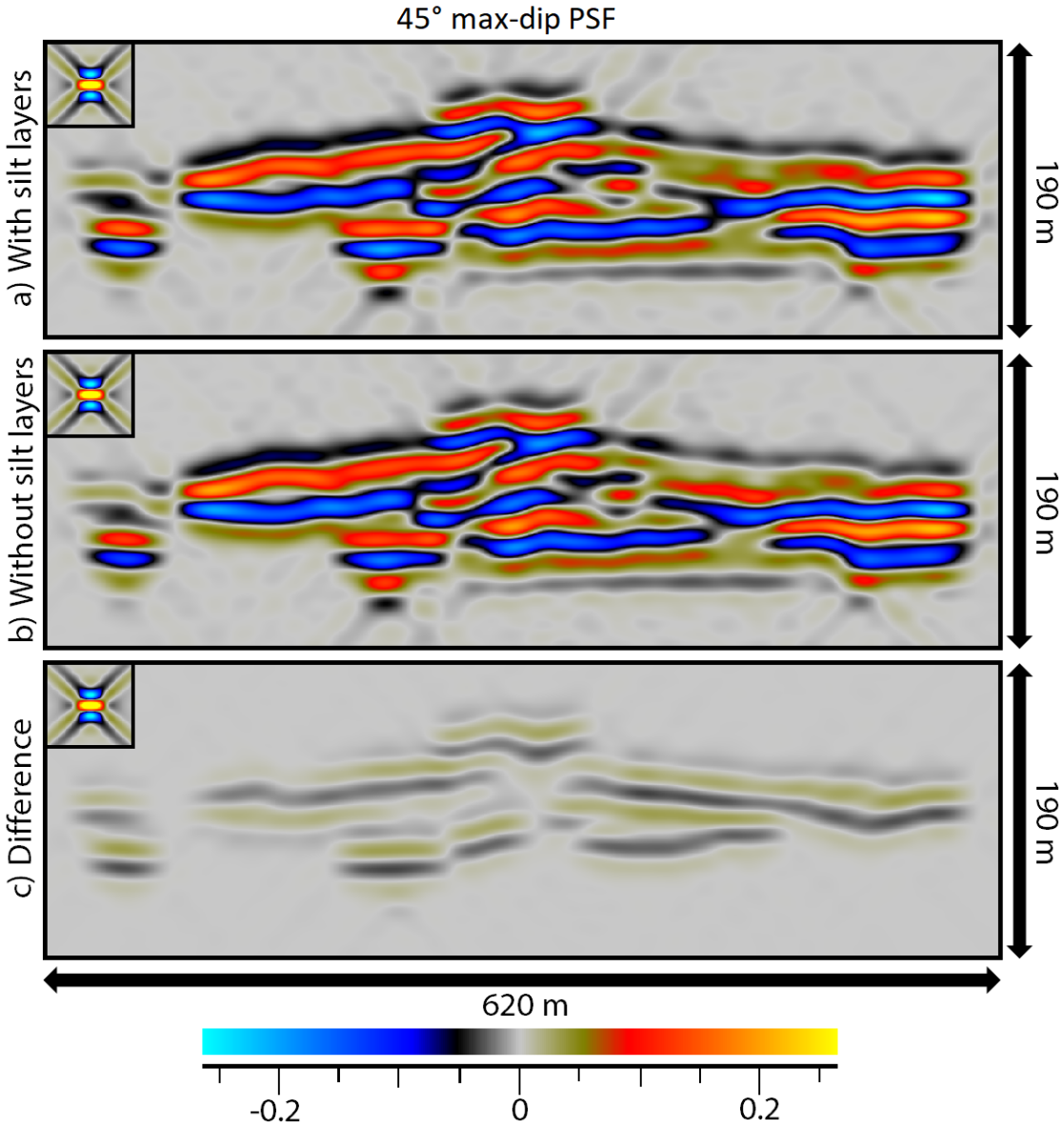

Figure 4.30: *The Beckwith Plateau outcrop modelled with a 45˚ max-dip PSF. (a) The model with thin silt layers in the model, (b) without silt layers, (c) the difference between the two cases (a) and (b)*

As illustrated in Figures 4.28, 4.29, 4.30, the silt layers have various effects on the seismic. Using the maximum values for the case with silt layers, and the difference plot, I estimated the degree of effect the silt layers have in terms of amplitude variations, by reading the maximum values in the amplitude calibrated models.

Table 4.5: Effect of silt layers

	With Silt Layers	Difference	Percent
1D "PSF"	0.2642	0.0460	17.4
Perfect illumination PSF	0.2440	0.0366	15
45° max-dip PSF	0.2526	0.0356	14.1

Table 4.5 shows that, in this case, the silt layers have a bigger impact on the amplitude values for the 1D convolution modelling method than the 2(3)D convolution modelling operators. It is also interesting to study how the 1D convolution method models these differences, in addition to how the method works in general for this complex target area.

I examined four interesting locations in the silt layered model, where the complexities of the model could cause difficulties for the methods. In addition, I explicitly studied how the methods modelled the dipping silt layers by enhancing the locations of the dipping layers in the difference plots.

Figure 4.29 and 4.30 shows that the seismic obtained by the two cases of 2D convolution modelling, using perfect illumination PSF and a 45° max-dip PSF, have few differences, except for some areas with lateral smearing, amplitude differences, and the striations around the model due to the cross-patterns of the PSF in the case with a 45° max-dip PSF. Since the two models are similar, I chose to only compare the 1D convolution to the more realistic 45° max-dip PSF case.

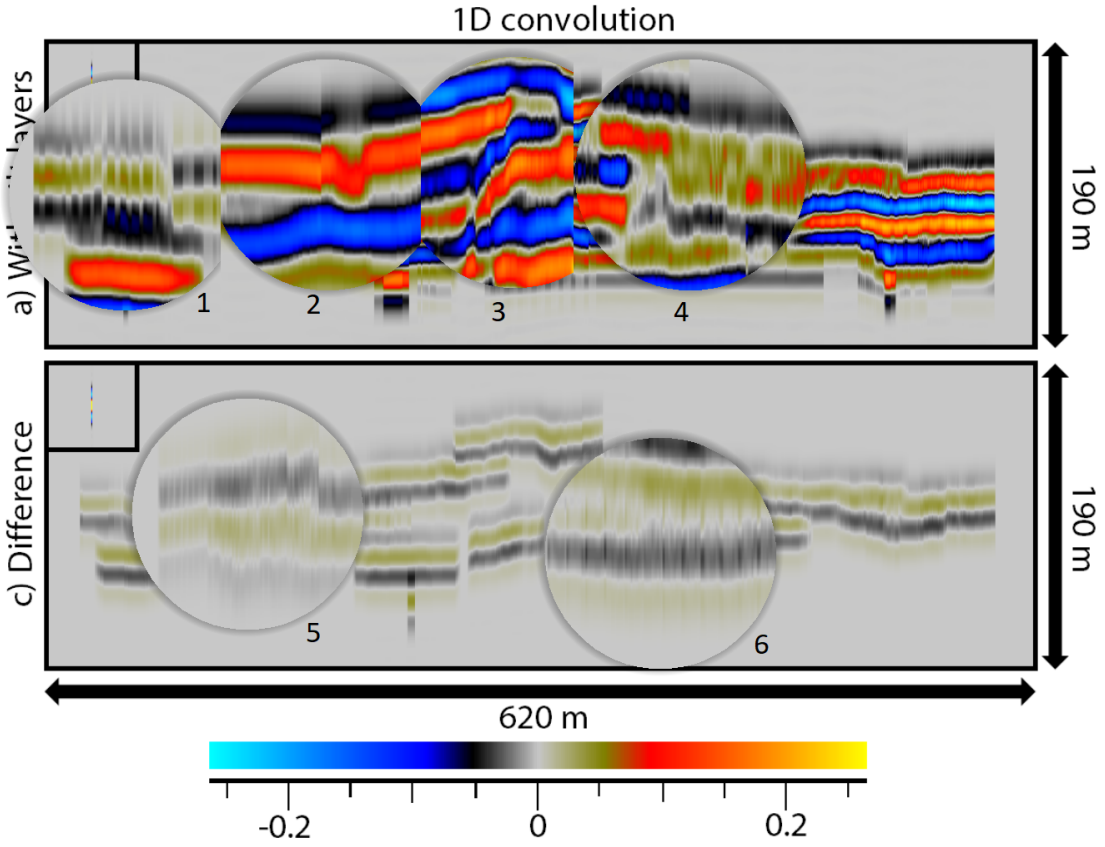

Figure 4.31: *The Beckwith Plateau outcrop modelled with 1D convolution, with six locations of interest highlighted and enhanced. Locations in the figure with silt layers; 1: Rough area. 2: Fault-like artefact. 3: Mid-section, complex, steep area. 4: Continued complex area with several small layers Locations in difference plot; 5: First location with dipping silt layers, 6: Second location with dipping salt layers.*

In figure 4.31.a, the Beckwith Plateau outcrop is modelled with 1D convolution. This model includes a lot of interesting artefacts, starting at the left side of the model (Location 1), where the seismic has a choppy shape, due to the thin layer in addition to the coal layer going through the rock. Further towards the middle part of the model, at location 2, the impact of a new structure above causes the model to suddenly go further up, without any smoothing, since there is no auto-interpolation. In the middle of the model, at location 3, the structure is steep with an array of different layers and properties. This causes the model to be rough and have a rapid thinning of some layers, which results in a discontinuous seismic.

Location 4 is where the silt layers have the most significant impact. It is a complex area with several different thin layers, which the seismic is not able to differentiate.

This causes a thick layer in the seismic which consists of two thin sandstone/silt layers, with a thin gap between them, in addition to low-velocity coal. In Figure 4.28.a and (b), we can observe the amplitude decrease caused by the silt layers in that area. Meaning that the layers does have an impact, even if the thin layers are not detected individually.

Generally, for this model, the 1D convolution modelling method struggles to generate a realistic image, and it results in a cluster of independent traces without considering the properties of the adjacent seismic. For an interpreter, all these choppy vertical changes may seem to be faults. This is especially the case with a much coarser lateral sampling. In locations 5 and 6, the dipping layers are modelled in an uneven manner, with sharp edges, in contrast to the other horizontal areas in the model.

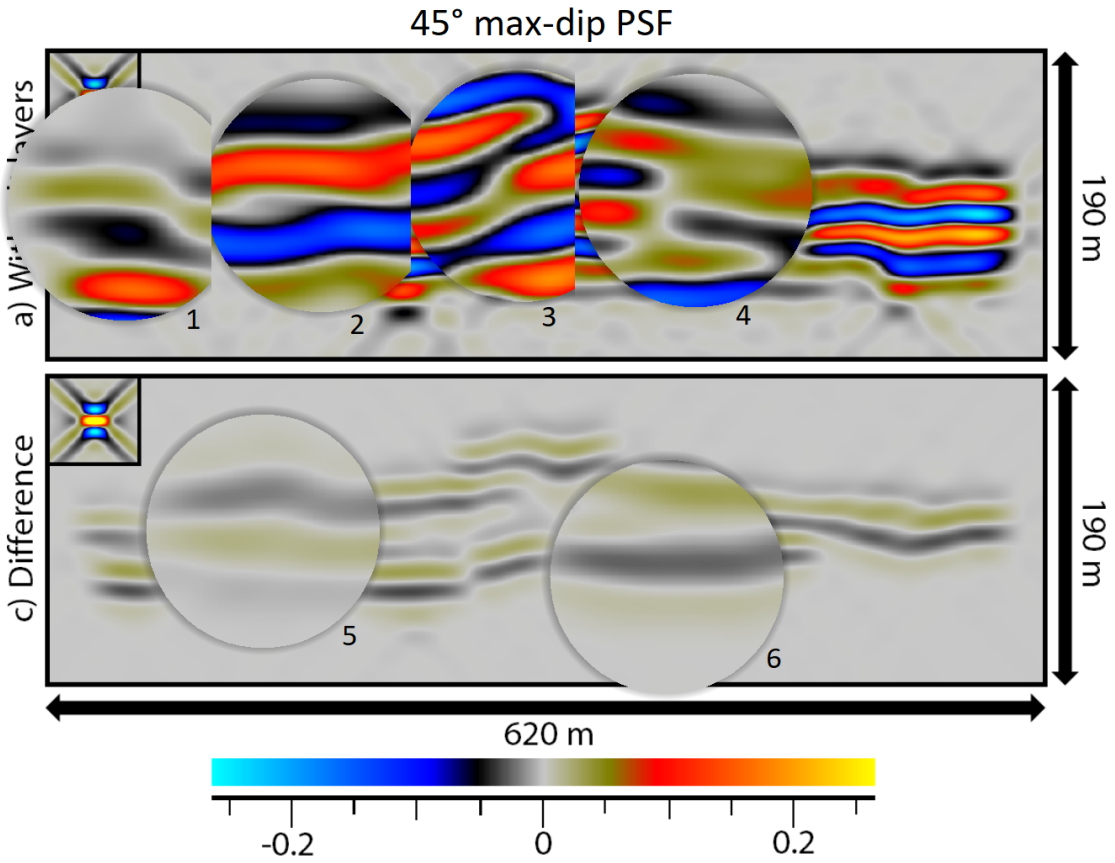

Figure 4.32: *The Beckwith Plateau outcrop modelled with 2D convolution, using a 45° max-dip PSF. Six locations of interest highlighted and enhanced. Locations in the figure with silt layers; 1: Rough area. 2: Steep area, modelled as a fault-like artefact in figure 4.31. 3: Mid-section, complex, steep area. 4: Continued complex area with several small layers. Locations in difference plot; 5: First location with dipping silt layers, 6: Second location with dipping salt layers.*

With a 45° max-dip PSF, figure 4.32 illustrates a smoother seismic of the Beckwith Plateau outcrop than 1D convolution. Starting at the location 1, the area is much smoother than the choppy section at location 1 in figure 4.31. In location 2, the seismic is continuous, and does not have the artefact the 1D convolution method had due to the steep layer. Further towards the middle, at location 3, the seismic is still continuous, but the seismic remains difficult to interpret in the complex middle section, with high amplitudes where the sandstone is located. The thick reflector at location 4 is still present in this modelling method, but now the amplitudes are more evenly distributed, in other words, the lateral resolution effects is more realistic than for 1D convolution modelling. At location 5 and 6, the lateral smearing and

frequency of the wavelet causes the dipping layers to be invisible.

4.6 3D modelling: Setergrotta

Using 3D data from the Setergrotta cave system provided by FOPAK, I can study the effects of the different convolution operators on real 3D data. For real 3D data the fashion in which the data is acquired has a significant effect on the resulting resolution. In this section the acquisition theory is idealized.

With 3D seismic data it is possible to study full 3D resolution effects, where the seismic in one slice is affected by nearby events, which may not be present in that chosen slice. To study these effects, I focused on two cases; a vertical slice adjacent to a cave, and a horizontal slice, to study the seismic as seen from above. In both cases I will use 1D convolution modelling, and the 3D convolution modelling method, represented by a perfectly illuminated PSF and a 45° max-dip PSF. The two latter have a full 3D resolution, while the 1D convolution only has vertical resolution effects, illustrated in Figure 4.33.

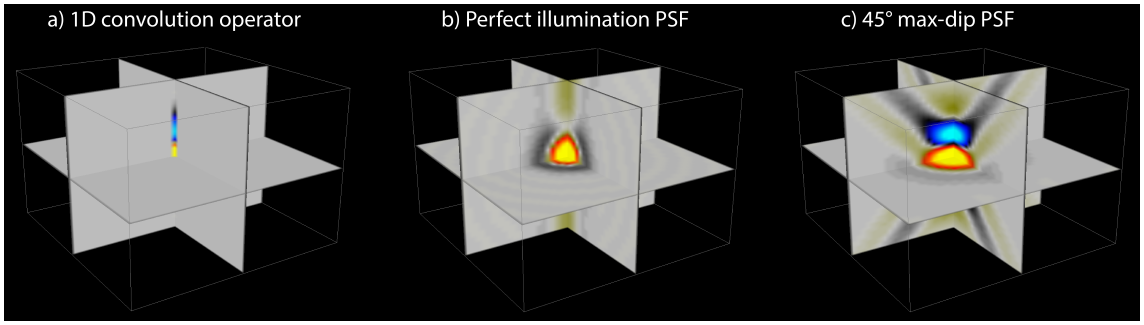

Figure 4.33: *3D view of the 30 Hz Ricker generated PSFs used in this section (a) 1D convolution operator, or 1D "PSF" (b) perfect illumination PSF and (c) 45° max-dip PSF.*

The amplitude calibration values obtained for this model is given in the table 4.6, for each method and each with three different frequencies, 30 Hz, 50 Hz and 80 Hz.

Table 4.6: Amplitude calibration values

Frequency	1D conv.	45° max-dip	Perf. ill.
30 Hz	19.42	19.69	19.38
50 Hz	11.67	11.69	11.67
80 Hz	7.29	7.29	7.29

A high value means high amplitude loss, and in this case, for the low frequencies the 45° max-dip PSF will have more amplitude loss than the two others, this is probably due to the noise from the cross patterns and broader PSF causing more lateral resolution effects than the perfect illumination and 1D convolution "PSF". The two latter quickly align, with the perfect illumination having lower amplitude loss for lower frequencies. As the frequency increases the amplitude loss will go towards the same for all methods, meaning the effects from the convolution PSFs will be small in comparison to the effects from the physical factors along the ray-path.

For 1D each seismic slice will be independent of nearby events in the lateral direction, but it has an impact on layers above and below. With 3D PSFs the nearby reflection/diffraction events in all three directions will influence surrounding seismic. The model is generated with an average velocity of 3.5 km/s, a 30 Hz Ricker wavelet, and a vertical and lateral sampling of 2.5 and 5 m, respectively. The plots are generated without auto-interpolation, as is the normal in the thesis.

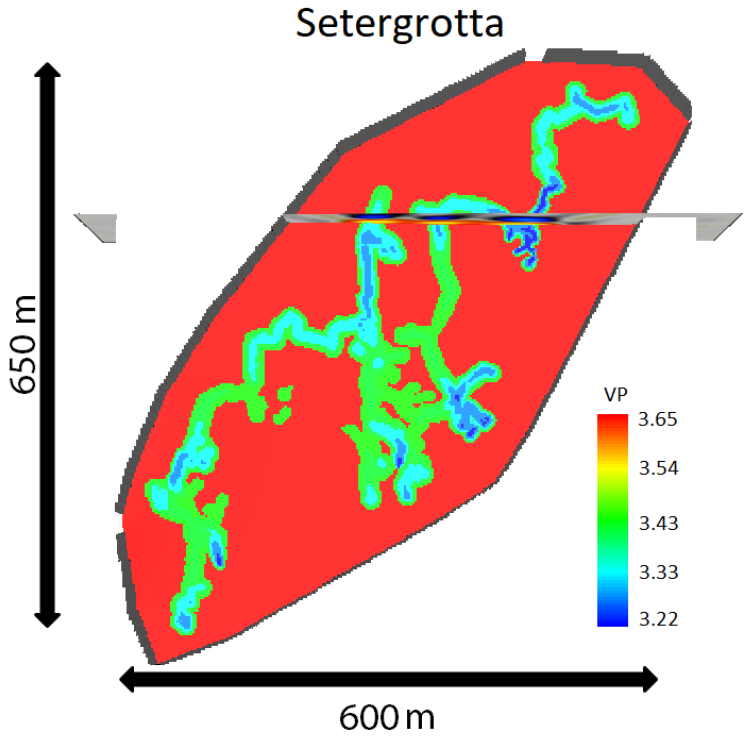

Figure 4.34: *A layer in the middle of Setergrotta with the location of the slice.*

Figure 4.34 illustrates the general shape of Setergrotta by a layer in the middle of

the cave. The seismic slice shows where the studied vertical plane is located. The slice is chosen due to its placement right beside a long cave, which means that in this area the seismic generated from the reflectivity of the cavern should interfere with the seismic from the events in the slice when we use a 3D convolution PSF.

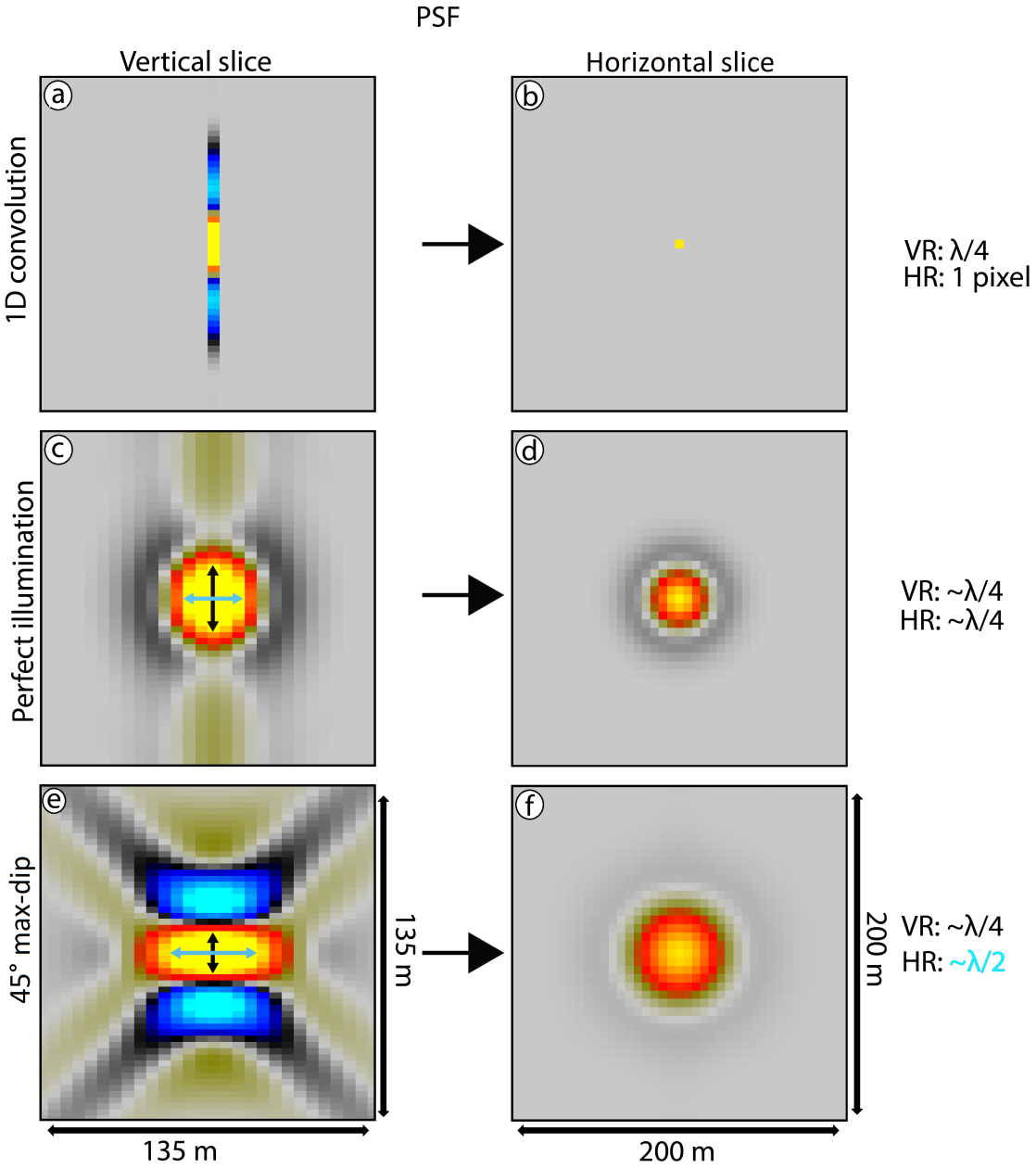

Figure 4.35: *The 30 Hz Ricker generated PSFs used in this section, both as vertical slices (a, c, e) and seen from above (b, d, f). Vertical and horizontal resolution illustrated by the black and turquoise arrows in the PSFs. Different axis values due to user-defined boundaries in the vertical slice.*

Figure 4.35 illustrates the three 30 Hz PSFs used when modelling Setergrotta, both as vertical and horizontal layers. As the vertical resolution is about a quarter of

the dominant wavelength, it is possible to use the relations in the PSF to find horizontal/lateral resolution. For the 1D convolution, the lateral resolution is a pixel-size, since there is no lateral resolution effects. For the perfect illumination PSF, the ratio between the lateral and vertical resolution is 1:1, as illustrated by the arrows in Figure 4.35.c, which gives a lateral resolution of about $\lambda/4$. In the 45° dip, however, the arrow indicating lateral resolution is twice as long as the vertical, which means that the lateral resolution effects are twice the vertical. This gives a horizontal resolution of $\lambda/2$. This results in a broader horizontal area as illustrated in Figure 4.35.f.

The PSF used to generate the model is in the top left corner of each figure. This PSF is, however, not to scale, nor is it calibrated, it is merely there to illustrate the shape of the PSF for each model. The reason for it not being to scale is because each PSF is originally 135 x 135 metres, which would take too much space in the figure. PSFs with calibrated values are shown in Figure 4.47 and Figure 4.33.

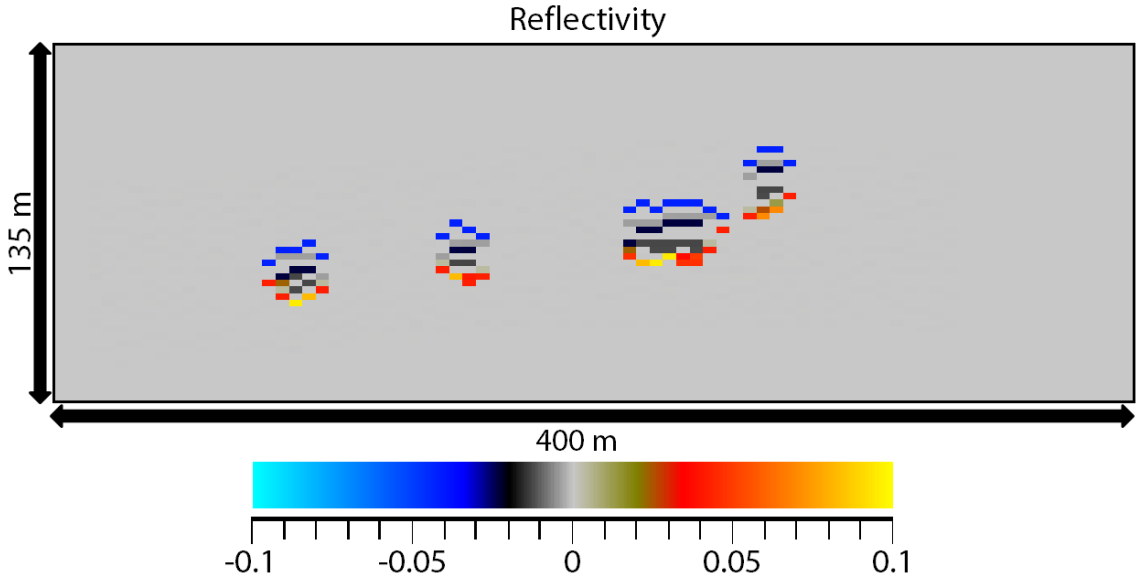

Figure 4.36: *The Reflectivity model of Setergrotta at the chosen slice.*

The reflectivity model 4.36 shows four events, with a varying degree of gaps in between them. The reflection events represent the caves present in the slice. It is interesting to study how the lateral resolution effects affect the seismic images with different PSFs, as the 1D convolution will only have vertical effects, and there are significant gaps where the effects from the PSFs will generate lateral resolution effects from the reflections.

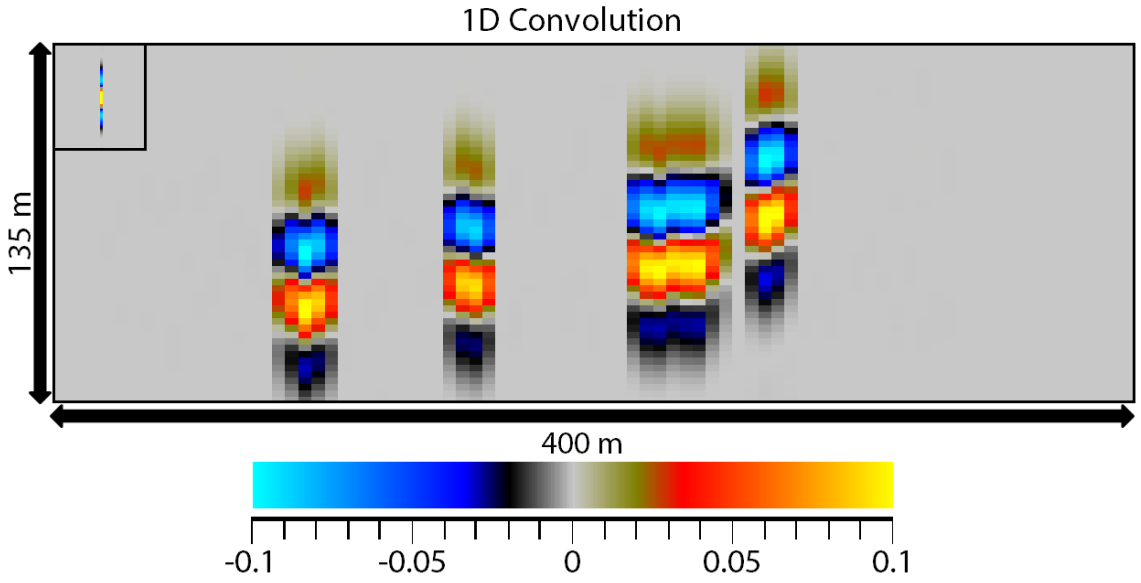

Figure 4.37: *Vertical slice from Setergrotta with 1D convolution.*

1D Convolution shows exactly where the reflectors are, with some vertical smearing. As the 1D convolution method does not have any lateral effects, the lateral resolution is the pixel-size of the wavelet, while the vertical resolution is $\lambda/4$. This means that the energy from the reflectors, in the section or nearby, has no effect on each other, which results in the abrupt cut-offs in the section.

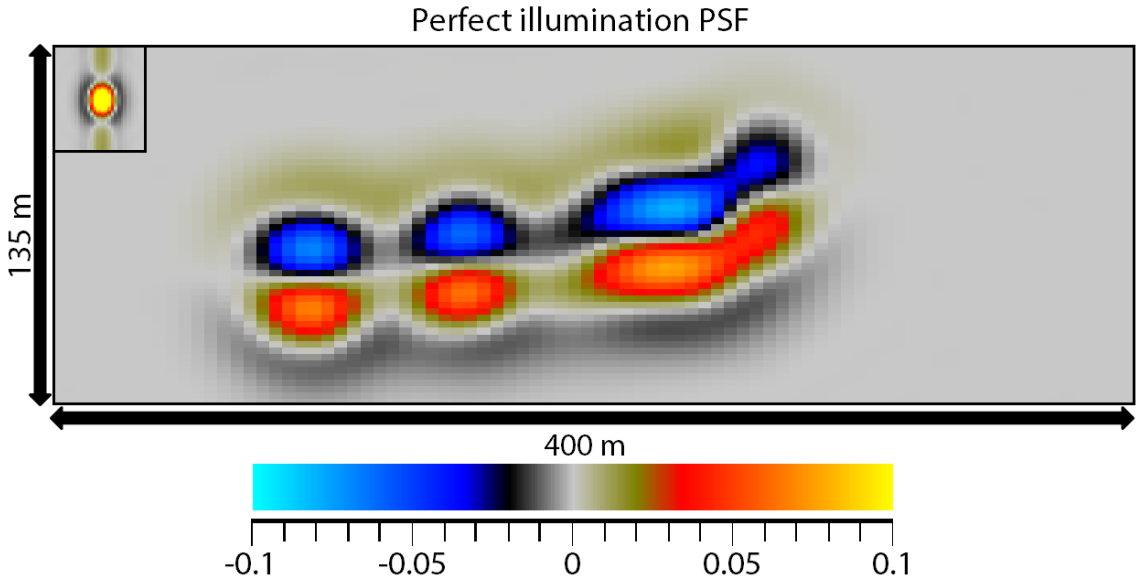

Figure 4.38: *Vertical slice from Setergrotta with a perfect illumination PSF.*

Modelling with perfect illumination PSF, Figure 4.38, there is lateral resolution effects, so the energy from the reflectors affects the surrounding seismic, which causes the nearby energy from reflection points of the cave system to interfere with the slice. Due to the relatively small size of the perfectly illuminated PSF, the lateral resolution is $\lambda/4$, which is approximately the same as the vertical resolution.

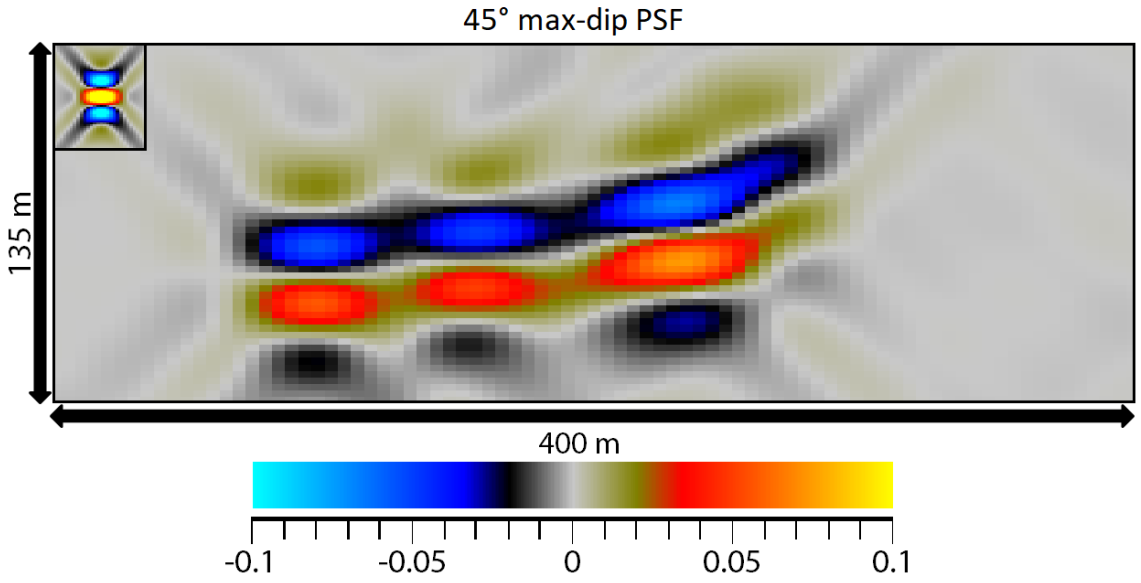

Figure 4.39: *Vertical slice from Setergrotta with a 45° max-PSF.*

Due to the cross-patterns due to limited illumination in the 45° max-dip PSF, the resulting seismic, Figure 4.39, will have significantly more resolution effects than both the perfect illumination PSF and 1D wavelet. The vertical resolution is still $\lambda/4$, but the limited illumination causes its lateral resolution to be $\lambda/2$. The nearby cave has probably influenced the seismic, causing strong seismic where there is no reflectors. This increase in 3D resolution effects complicates the interpretation, which can cause an interpreter to might see two lateral layers, not the four caves. However, this seismic is more realistic than the 1D convolution, where everything is independent.

In addition to the vertical slice, a horizontal slice was studied. The location of the horizontal slice is illustrated in Figure 4.40. It is located in the lower section of the model, chosen to study how the higher mid-section affects the seismic of the slice. In the horizontal cases, the PSFs in the figures are to scale, but not calibrated.

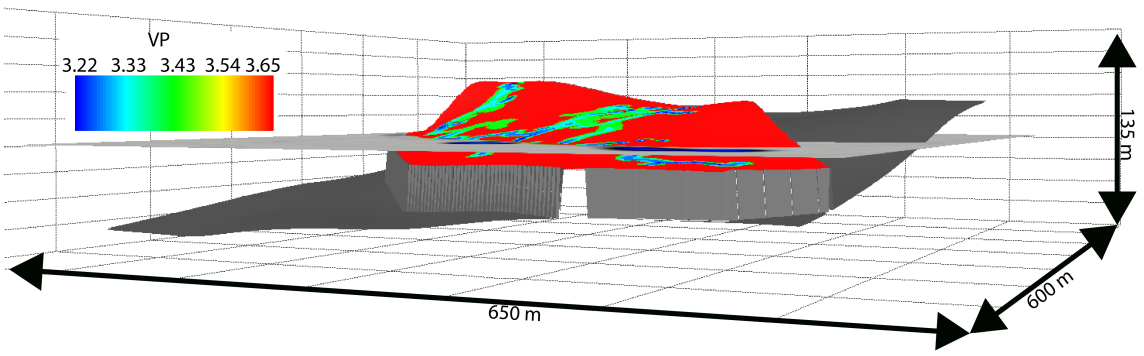

Figure 4.40: *Location of the horizontal slice (light grey) in the Setergrotta cavesystem.*

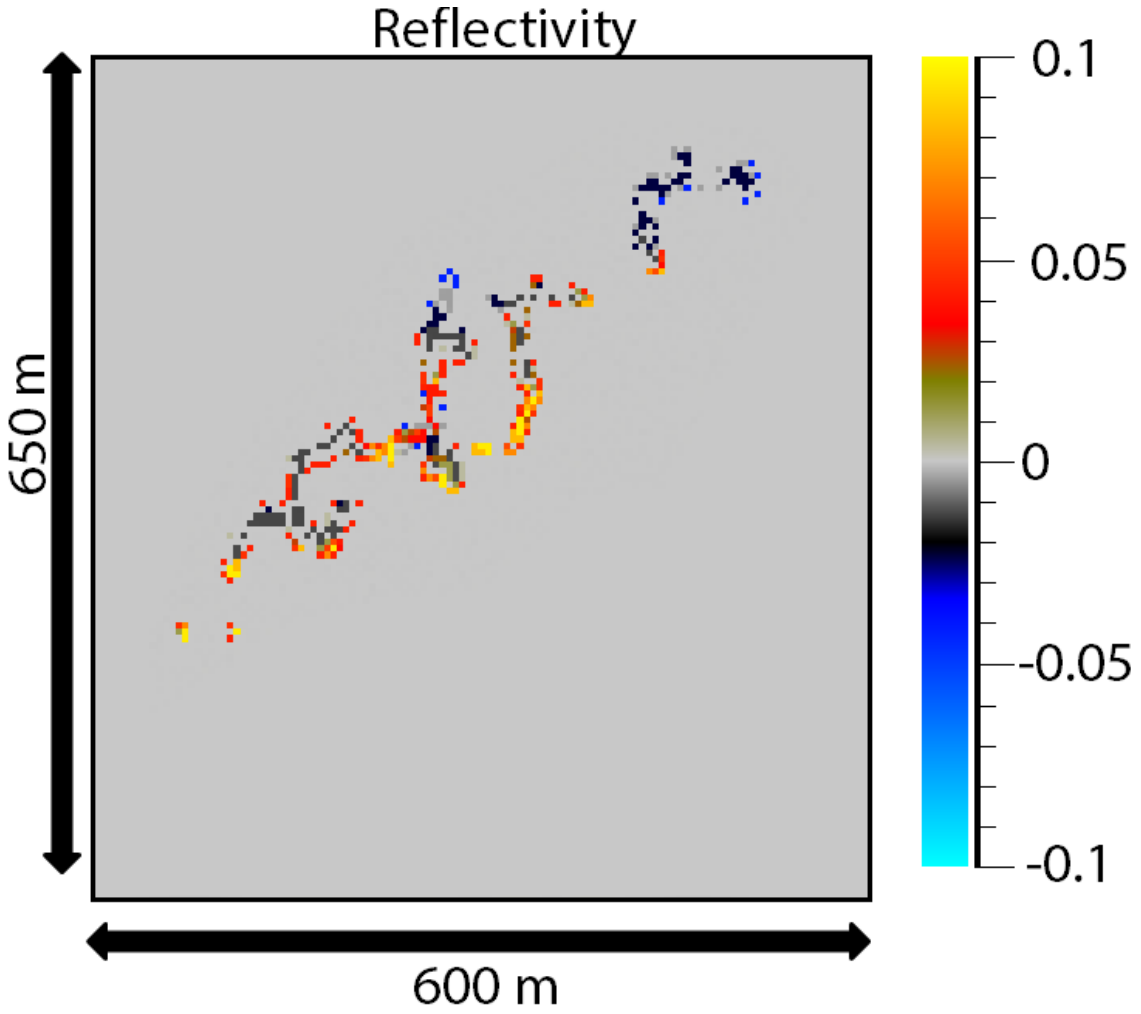

Figure 4.41: *The corresponding Setergrotta reflectivity model as seen from above.*

The reflectivity surface in 4.41 is below the low-velocity cave system in the middle of the model, and it is such not present in Figure 4.41. However, due to its strong AI, it is interesting to see how the energy from those reflections influence the seismic in the chosen slice in 4.41.

To study the differences between the reflection model and the modelling methods, the figures is in the same places in the pages, for easy comparisons, similar to the Beckwith Plateau model.

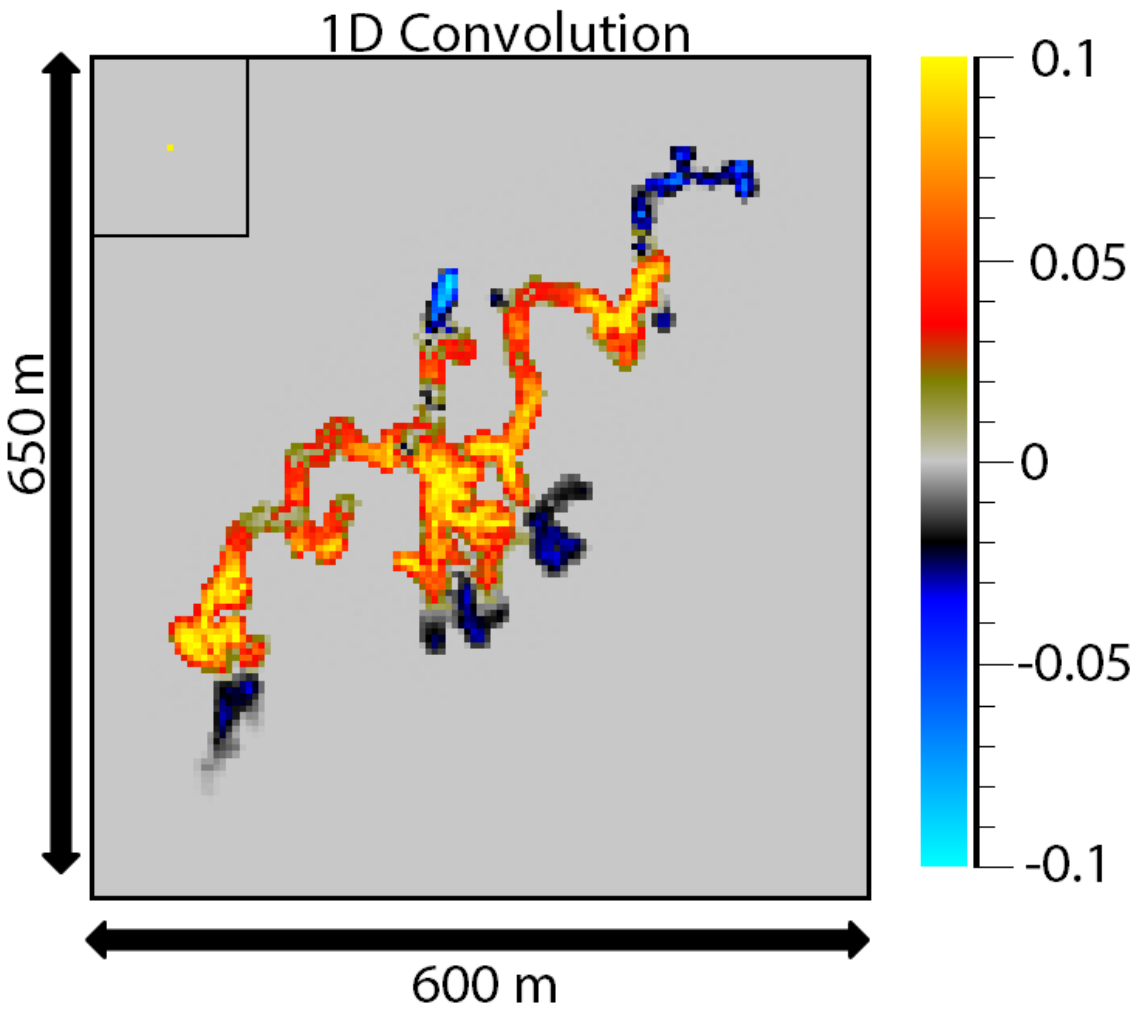

Figure 4.42: *Horizontal Setergrotta slice with 1D convolution.*

The 1D convolution captures seismic from the entirity of the cave, with high amplitudes from the low-velocity middle area of the cave, and the point of highest altitude apparent in the bottom of Figure 4.42. This is a result of vertical resolution effects, and an example of how difficult it is to differentiate between depths in seismic imaging. Since the lateral resolution effects are non-existing, the seismic is only a result of the vertical resolution effects of the layers. This causes the seismic model to have an unrealistic appearance, as the seismic merely illustrates the points of reflection in the Setergrotta cave system.

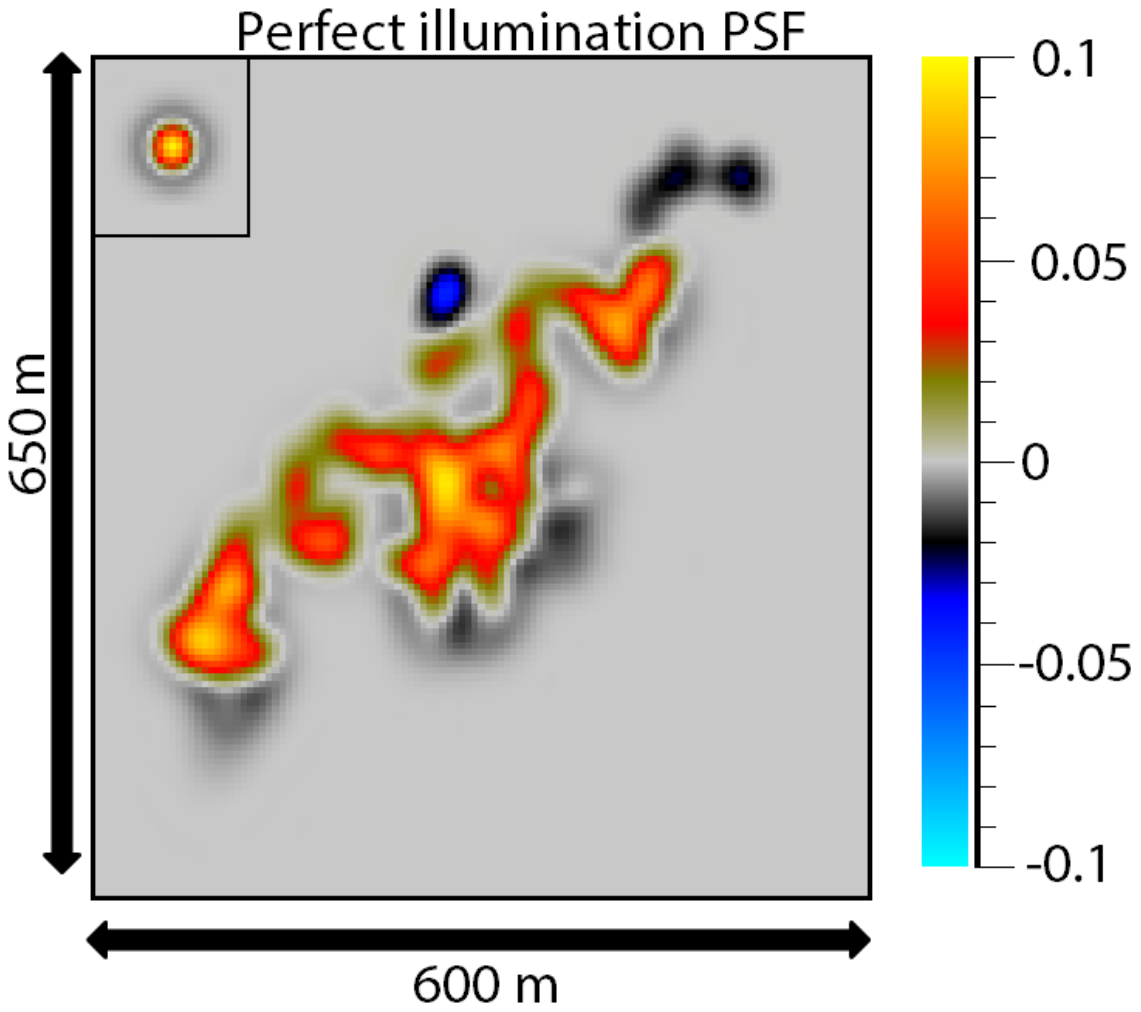

Figure 4.43: *Horizontal Setergrotta slice with perfect illumination PSF.*

Using a Perfectly illuminated PSF, the introduces lateral resolution effects is introduced in the seismic, Figure 4.43. This causes the seismic to be less precise, as the seismic is a result of interference from both lateral and vertical resolution effects at each reflection point. To interpret this layer is not an easy task, as there is lateral smearing in the seismic, in addition to the strong amplitudes from structures not present in this slice.

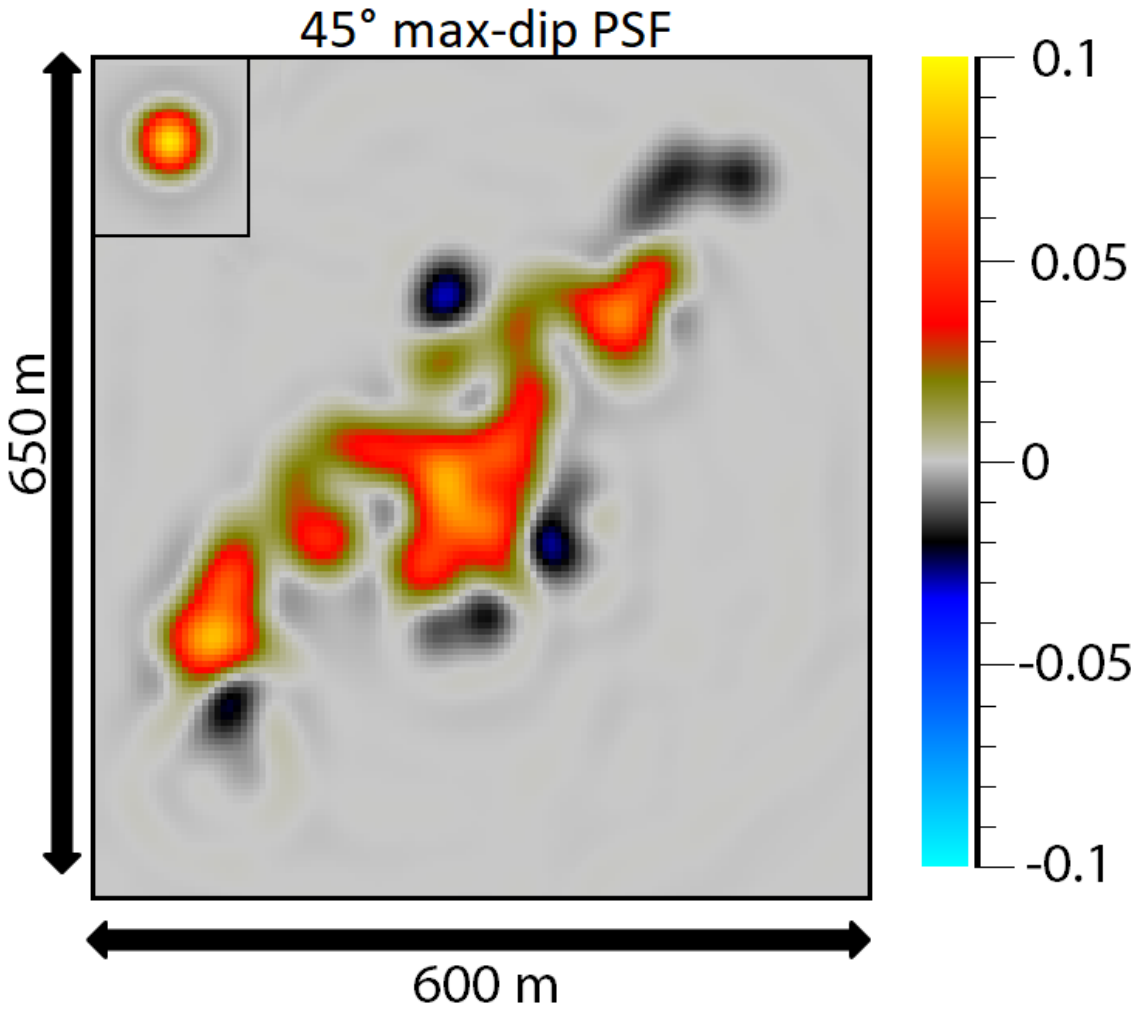

Figure 4.44: *Horizontal Setergrotta slice with 45° max-dip PSF.*

In comparison to the perfect illumination PSF, the 45° max-dip generated seismic, Figure 4.44, will cover a broader area due to the worse lateral resolution of $\lambda/2$. This lateral smearing effect causes the amplitude values to be spread more evenly in the slice.

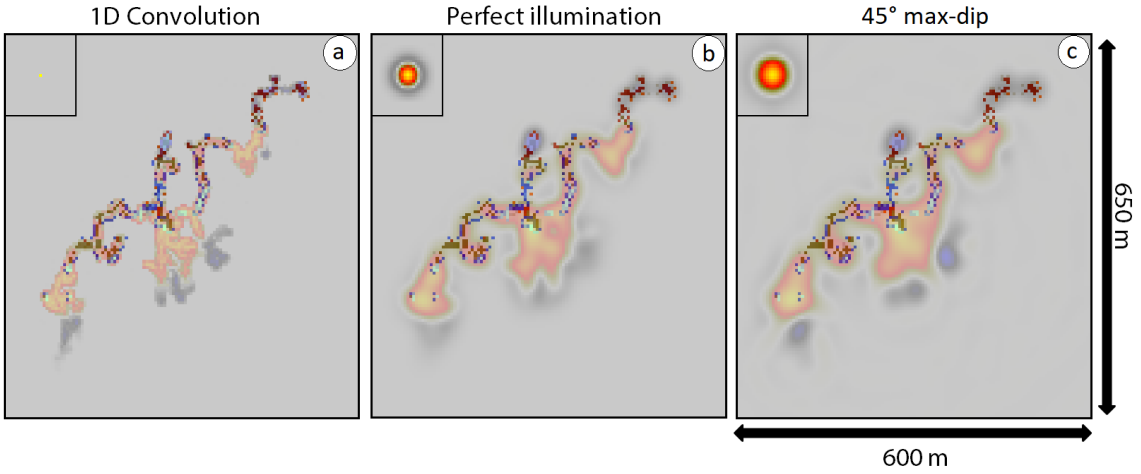

Figure 4.45: *The seismic as seen from above compared with the reflections, not calibrated.*

In Figure 4.45, the results of the lateral slices are compared, using the reflection points of the slice in a reverse-seismic colour map. Since the 1D method does not have lateral resolution effects, the 1D case is only affected by the vertical layers, causing the image to be precise and detailed at the reflection points for the nearby layers. The 45° max-dip and perfectly illuminated PSF generated seismic have lateral resolution effects, so the models are dependent on the whole 3D resolution. The difference between these two is that the 45° max-dip will have more effects due to its wider PSF and its cross patterns, causing a worse lateral resolution and thus more weak reflections is visible. This is not the case for perfect illumination, as a smaller PSF will not generate as much lateral noise, causing less weak reflections from the nearby layers to be visible.

Due to the vertical resolution, all the 30 Hz Ricker wavelet generated seismic models will include strong reflections from the surrounding cave passages, especially in the middle part, where there is a high AI structure. Modelling with two higher frequencies, 50 Hz and 80 Hz, were done to illustrate the effects of higher frequencies on the resolution but it should be noted that these may be too high for realistic seismic surveys, and is only to illustrate the vertical resolution problems when the reflection events are close together, the corresponding calibrated PSFs are included in Figure 4.47. As the resolution is dependent on the frequency, using higher frequencies will narrow down the amount of seismic energy from nearby events to be visible in the seismic.

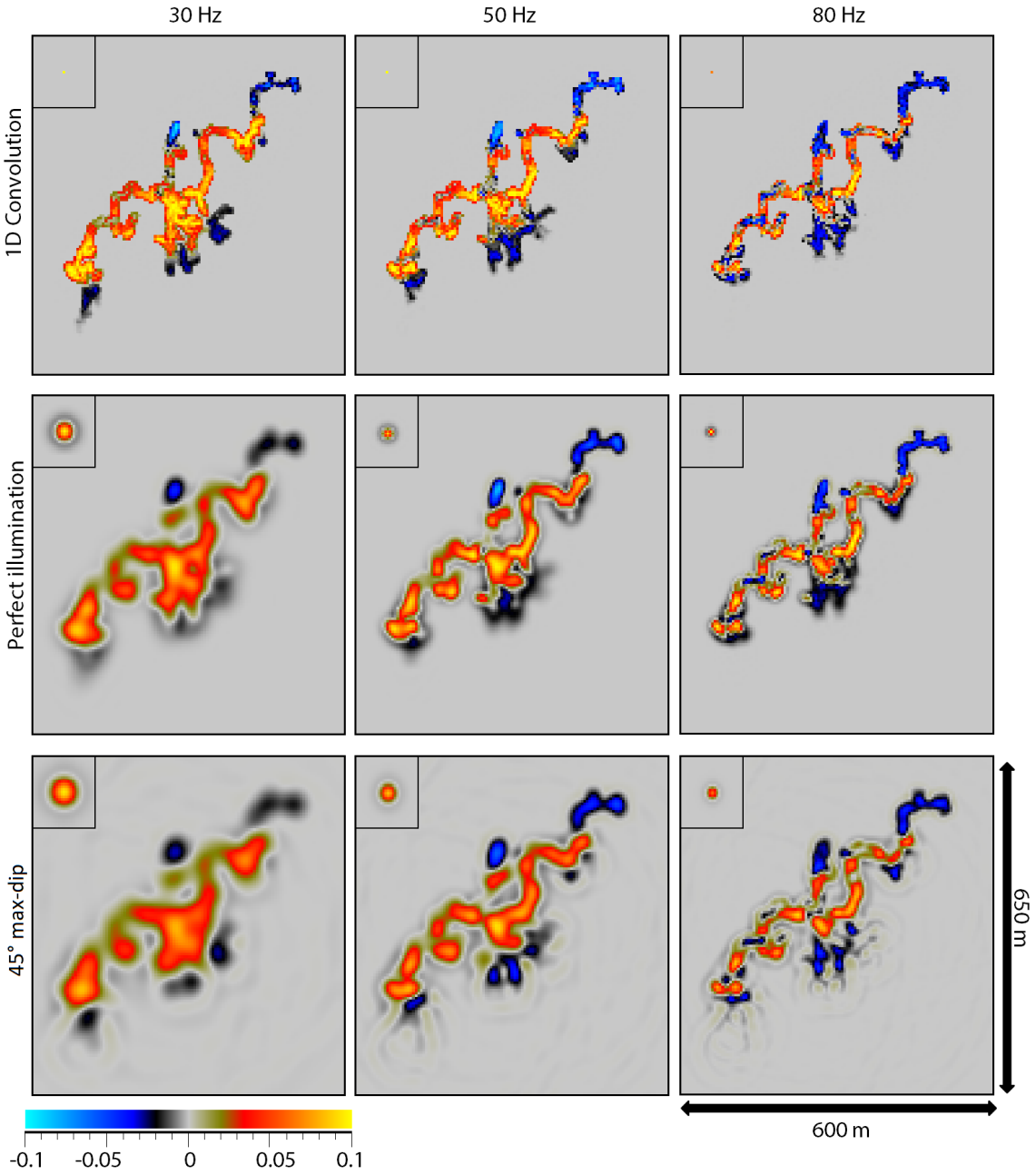

Figure 4.46: *Amplitude Calibrated seismic from 1D, 45-degree dip and perfect illumination with 30 Hz, 50 Hz and 80 Hz Ricker wavelets.*

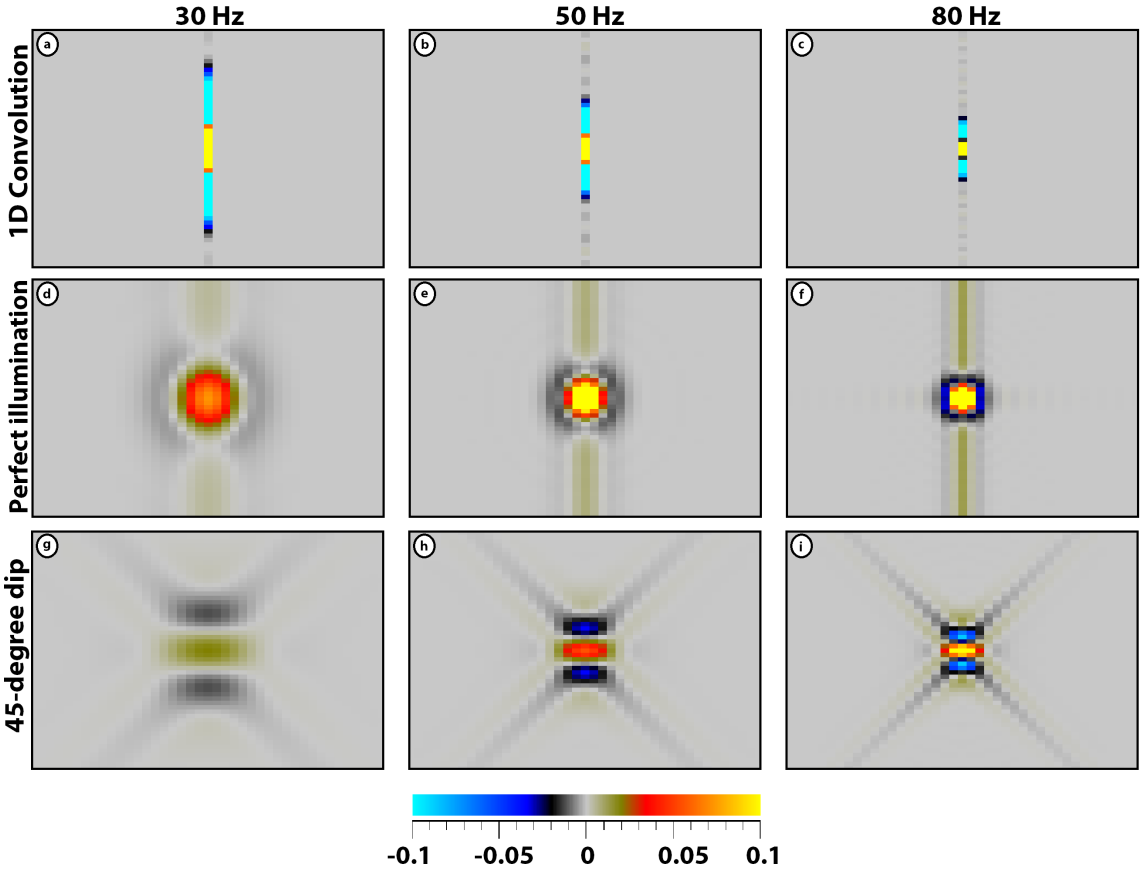

Figure 4.47: *The amplitude calibrated PSFs generated for the survey, with 30 Hz, 50 Hz and 80 Hz Ricker wavelets.*

In figure 4.46, the weak reflections (values around zero) disappears with higher frequencies. For the 1D convolution "PSF", there is no significant change in shape, but gradually the weakest reflections will be removed. For the 3D PSFs both the vertical and lateral resolution will be affected. In the perfect illumination case, the 30 Hz case already has minimal effects from the other layers, and the few effects is rapidly removed with increasing frequencies. For 80 Hz the seismic is very similar to the 1D convolution modelling, with more rounded edges. For the 45° max-dip the shape of the cave is immediately revealed with a 50 Hz Ricker wavelet, and most of the weak reflections are gone, while the seismic generated by reflection points in the slice will be stronger. Figure 4.47 also illustrates how the weak the PSFs are in the cases where they are calibrated to the values of the seismic.

I timed the modelling of the modelling methods when generating this 30 Hz, 50 Hz, and 80 Hz Ricker wavelet Setergrotta model, which is the most complex model in

this work, meaning that this should be where the differences are the most significant.

Table 4.6: Processing duration

PSF	Time (s)
1D	60
Perfect illumination	66
45° dip	66

After defining my parameters (target model, sampling, average velocity, etc.), the difference in processing time between the 1D and the 3D convolution modelling methods for the Setergrotta model is approximately 6 seconds with the 64 GB RAM computer I used for the processing in this thesis.

Chapter 5

Discussion

In this thesis, I studied two convolution modelling methods and their illumination and resolution effects. My motivation was to study if the effects of the 2(3)D convolution modelling method were so different from the 1D convolution that I would be persuaded to side with one over the other. I also included the difficulty of using the modelling methods in my assessment, as the primary features of the 1D convolution is its simplicity and speed.

In the introduction, an outcrop with a horizontal edge-detect filter is presented, Figure 1.2. This filter detects vertical differences, but cannot account for lateral differences, this is analogous to the 1D convolution. Figure 1.3 uses a blurring effect, where the lateral blur is twice the value of the vertical. This is the same relation as in the 45° max-dip PSF generated seismic, where the lateral resolution is twice as worse as the vertical resolution, which is analogous for the limited illumination of a realistic seismic survey. The perfect illumination PSF is seismic without illumination limitations, which is interesting to study due to a 1:1 ratio of lateral and vertical resolution effects, however, it is not possible for a seismic survey.

To test the robustness of the methods, the modelling cases in this work have an increasing structural complexity. However, due to time limitations, only normal incidence cases were considered, where I opted to work with several modelling cases rather than include AVO effects. They do not include noise or other complicating factors, as the modelling cases are used to study how the methods dealt with the models without outside interference.

5.1 Choice of wavelets

The models are all modelled with Ricker wavelets, except in Figure 4.9.b, where I modelled the wedge model with a generated Ormsby wavelet, with a main lobe corresponding to a 25 Hz Ricker wavelet (Ryan, 1994). This was mainly done to study how the noise of the side lobes would affect the seismic, and if I wanted to model more complex models with this noise. In Figure 5.1 the effects of the Ormsby wavelet is compared with a 25 Hz Ricker wavelet. Since the Ormsby wavelet have a bending effect on the seismic, in addition to noise around the target, I concluded that to include the wavelet further would only serve to confuse the reader.

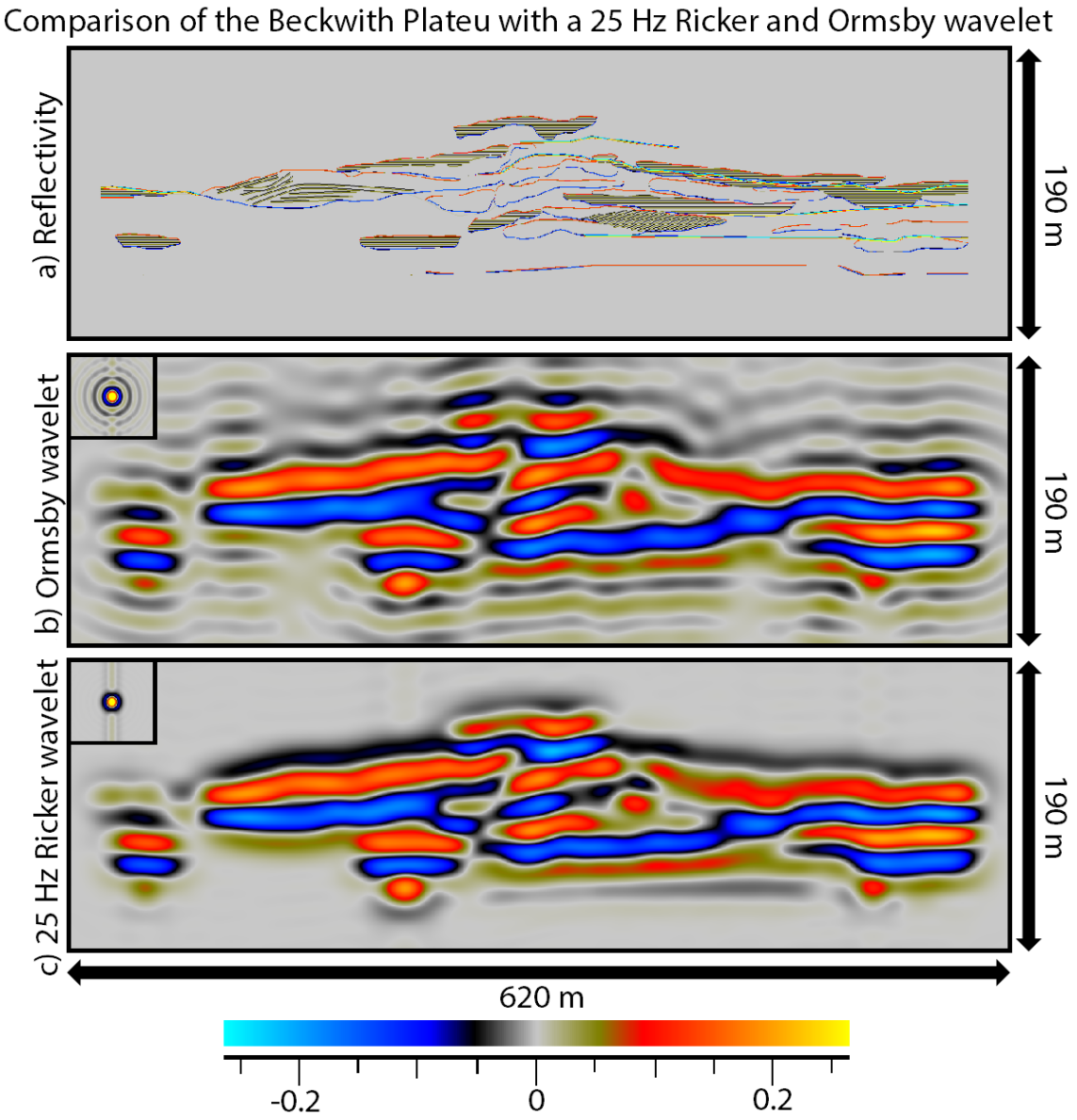

Figure 5.1: *Comparison of the Beckwith Plateu outcrop (reflectivity model (a)) with a perfect illumination PSF generated by (b) Ormsby wavelet, (c) Corresponding 25 Hz Ricker wavelet.*

Therefore, I chose to use the zero-phase Ricker wavelet going forward. After deciding on the shape of the wavelet, the next question was to decide which dominant frequencies I wanted to use. Of the three targets I wanted to model, both the Setergrotta model and Franklin Mountains model are karst reservoirs. For deep karst reservoirs, a frequency of about 25 Hz is realistic (e.g. (Zeng et al., 2011; Xu et al.,

2016)). The Beckwith Plateau outcrop consists of fluvial deposits which can be used as a potential analogy to fluvial reservoirs in the Barents Sea, where 30 Hz is a realistic frequency (e.g. (Eide et al., 2017; Klausen et al., 2017)). I then deemed 30 Hz Ricker wavelet to be a realistic frequency for the three main models, and thus easier for the reader to follow.

5.2 Models

5.2.1 Wedge model

The wedge model is still used to this day to study vertical resolution and tuning thickness (e.g. Mark et al. (2018); Eide et al. (2017)), since the simplicity of the model makes it possible to extract amplitude values from the horizontal reflector, which enables us to study when, and how the amplitudes in that reflector respond to the dipping reflector. In this case, I found that the tuning thickness increased when using the 2(3)D convolution modelling method compared to the 1D convolution method, which shows the effect of the complete resolution pattern has on the vertical resolution.

When studying the effects of the wedge I compiled a list of observations to explain how the amplitude values change in the seismic:

1) The classical effect studied with wedge models: The impact of the dipping reflector. As the dipping reflector of the opposite polarity approaches, it decreases the amplitude values of the horizontal reflector. However, this is before the interference begins, i.e., when the side lobes of the reflectors is nulled, and the amplitude values stabilize.

2) A direct contact between main lobes of opposite polarities causes an increase in amplitude values, due to the side lobes of the other reflector having a constructive interference

3) The lateral resolution effects cause the seismic from a reflection point to include amplitudes from adjacent reflection points in the 2D seismic, which in the case of a horizontal reflector results in constructive interference. This is in contrast to the 1D seismic, where the lack of lateral resolution in causes the amplitudes to be stable.

4) After the tuning thickness, the seismic has an upward trajectory, Figure 5.2. This causes the peak amplitude values in the seismic to leave the horizontal reflector where the values are extracted from. This results in a significant decrease in the amplitude values extracted at the horizontal reflector.

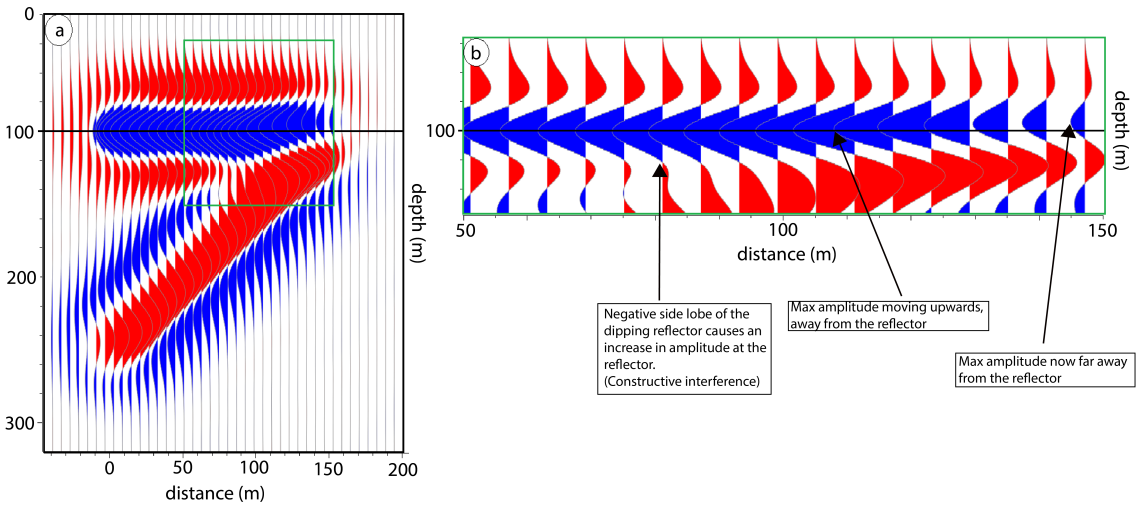

Figure 5.2: *(a) The wedge model generated with a perfect illumination PSF, with the horizontal reflector at 100 m. Green square: End of horizontal reflector, enhanced in (b) where the effects on the horizontal reflector caused by the dipping reflector are illustrated. Both with gain and clip effects, (a) to scale, (b) stretched*

I superimposed my results from the wedge models (Figure 4.15, 4.16, 4.17) in Figure 5.3, where I chose to mirror it to have the increase in amplitude and distance in the positive xz-direction. Figure 5.3 illustrates how the amplitude values differentiates due to the convolution methods, the 2D convolution methods both have significantly shorter stable parts, where there is no interference from the dipping reflector, and the reflector has its original amplitude value.

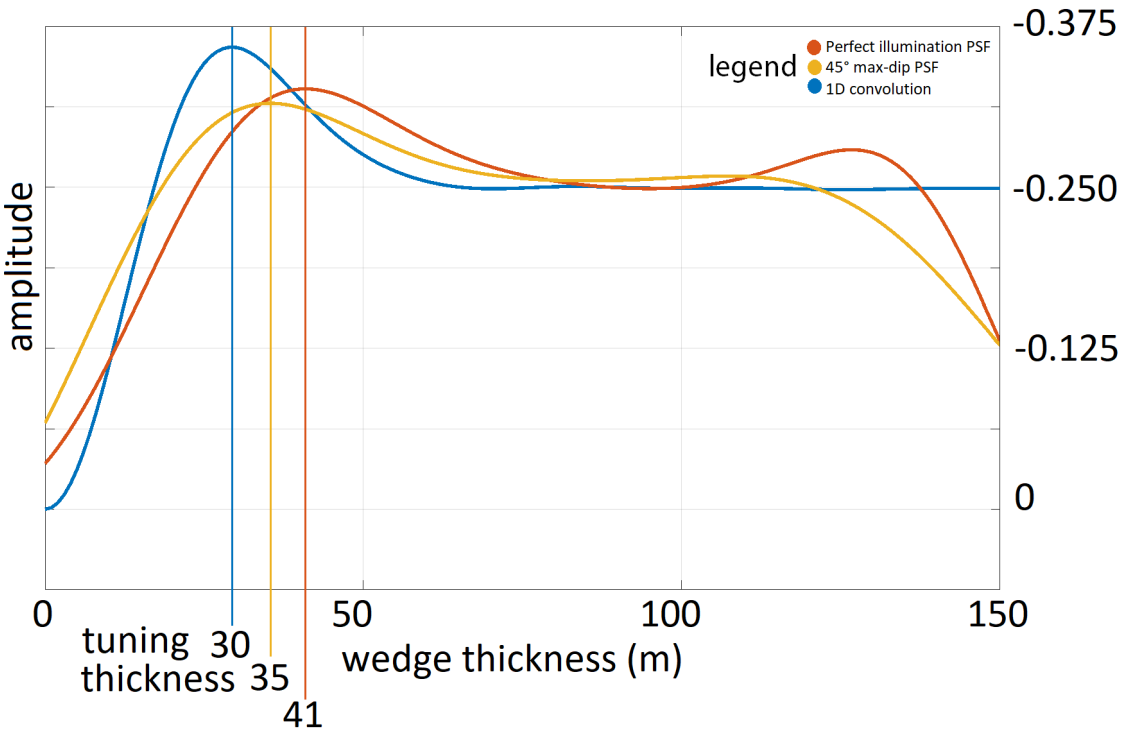

Figure 5.3: *Superimposed mirrored version of the tuning thickness figures.*

As all the values in Figure 5.3 are amplitude calibrated, the amplitude values should be at -0.250 when there is no interference. A striking feature from the 45° max-dip PSF model is that it does not stabilize at the amplitude value of the reflector. I believe the cause is that the dipping reflector may not be fully imagined, since its illumination range is 45° max-dip, which is exactly the same as that reflector.

I then modelled with a 60 ° max-dip PSF, and found that it did, indeed, reach the reflector value of -0.250 when it had no interference, and it has a tuning thickness at 41.5 m, which is thicker than the perfect illumination PSF, and the tuning thickness seems to increase with lateral resolution effects. This means that the seismic from the 45° max-dip PSF is most likely a result of a dipping reflector which is not fully illuminated. Since the dipping reflector is not fully illuminated, the effects of the wedge model are not proper, which causes the amplitude values at the reflector without interference to be higher than for the others.

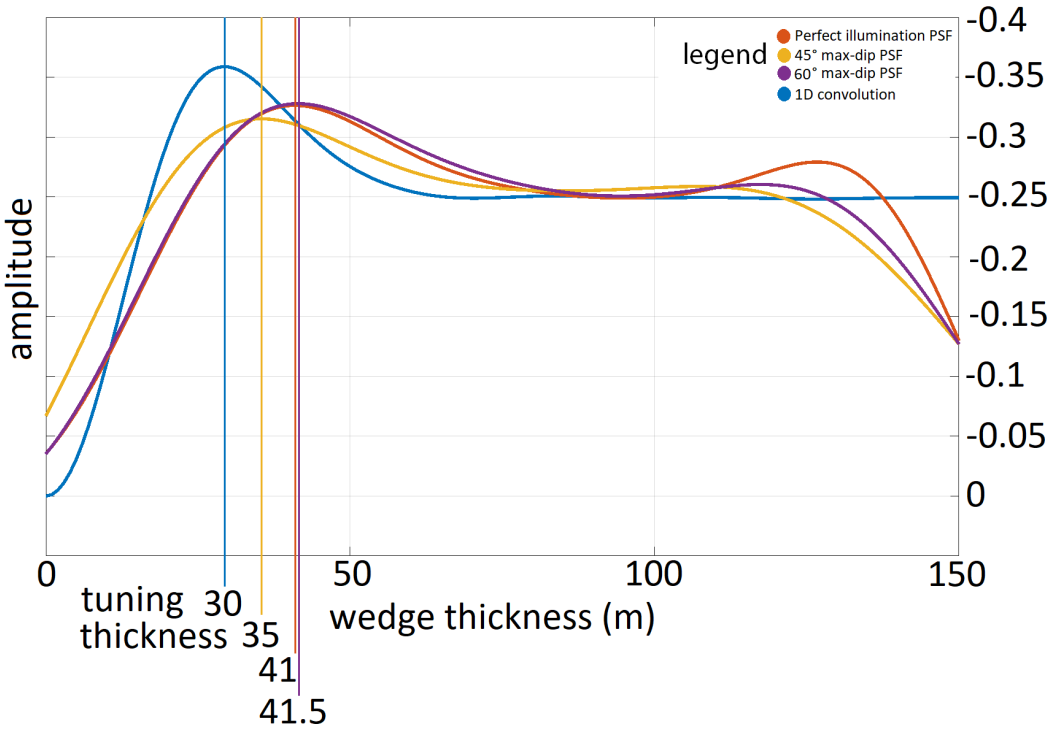

Figure 5.4: *Superimposed mirrored version of the tuning thickness figures, including a 60° max-dip PSF.*

Figure 5.4 then illustrates the amplitude values of the seismic if there is no lateral resolution effects (1D convolution), and three cases with lateral resolution effects; where two are properly illuminated (perfect illumintion PSF and 60° max-dip PSF) and one where the model is not fully illuminateed (45° max-dip PSF). These illustrates that the effect of lateral resolution causes an earlier interference between the reflectors, and a thicker tuning thickness than the case withouth lateral resolution effects.

The main reason why the wedge model was studied was to find out if the vertical resolution of the PSF-based convolution generated seismic would differ from the 1D convolution. The seismic model was made with these parameters: v=2410 m/s, dominant frequency f= 20 Hz, and the wavelength is given as λ= v/f.

Widess (1973) defines the tuning thickness as $\lambda/4$, which is a wedge thickness of 30 m. This is correct for the 1D convolution, where there is no lateral resolution or illumination effects. If these effects are included, i.e., using the 2D PSF-based convolution method, the tuning thickness increases, which means that these, often ignored, effects will influence the vertical resolution. I cannot give a definite relation between the results and the effects, as this is only one modelling case, but I

recommend to model more wedges with different parameters and wavelets to find the more systematic relations between the effects introduced in the 2D convolution modelling and a 1D convolution.

Throughout my research (and education, e.g., Kearey et al. (2002); Simm and Bacon (2014), etc.), I find that traditionally the vertical and lateral are treated as two separate entities, i.e., they do not influence each other. My results indicate that this is not the case, as there seems to be a relation between the vertical and lateral resolution.

5.2.2 Franklin Mountains

Unfortunately, the steep areas in the reflectivity model generated in SeisRoX had aliasing problems due to an intrinsic limit, which caused few reflectors in the steep "fold-like" shape in the bottom of the model, and the pipe above the GMS. This meant that these structures are not properly represented, and thus I had to study the other structures in the model, the main body of the GMS and the adjacent cave, illustrated in Figure 5.5.

The 2D modelling of Franklin Mountains further highlighted the lack of lateral resolution effects in the 1D method, where the 1D convolution struggled with the high velocities and sharp edges, Figure 5.5.b, with apparent tinning surrounding location 1, in addition to "fault-like" artefacts. This is also the case above location 2, with the dips of the fracture components. At location 3, the cave seems like a graben, with two thin faults on both sides.

These artefacts are not present in the results generated by the 2D PSFs, Figure 5.5.d.f, and they are both smoother. Interestingly, the 45° max-dip modelling case does not differ much from the perfect illumination PSF case, even though there are several steep structures in the caves. However, the amplitude values are slightly lower, as illustrated at location 3 in Figure 5.5.f.

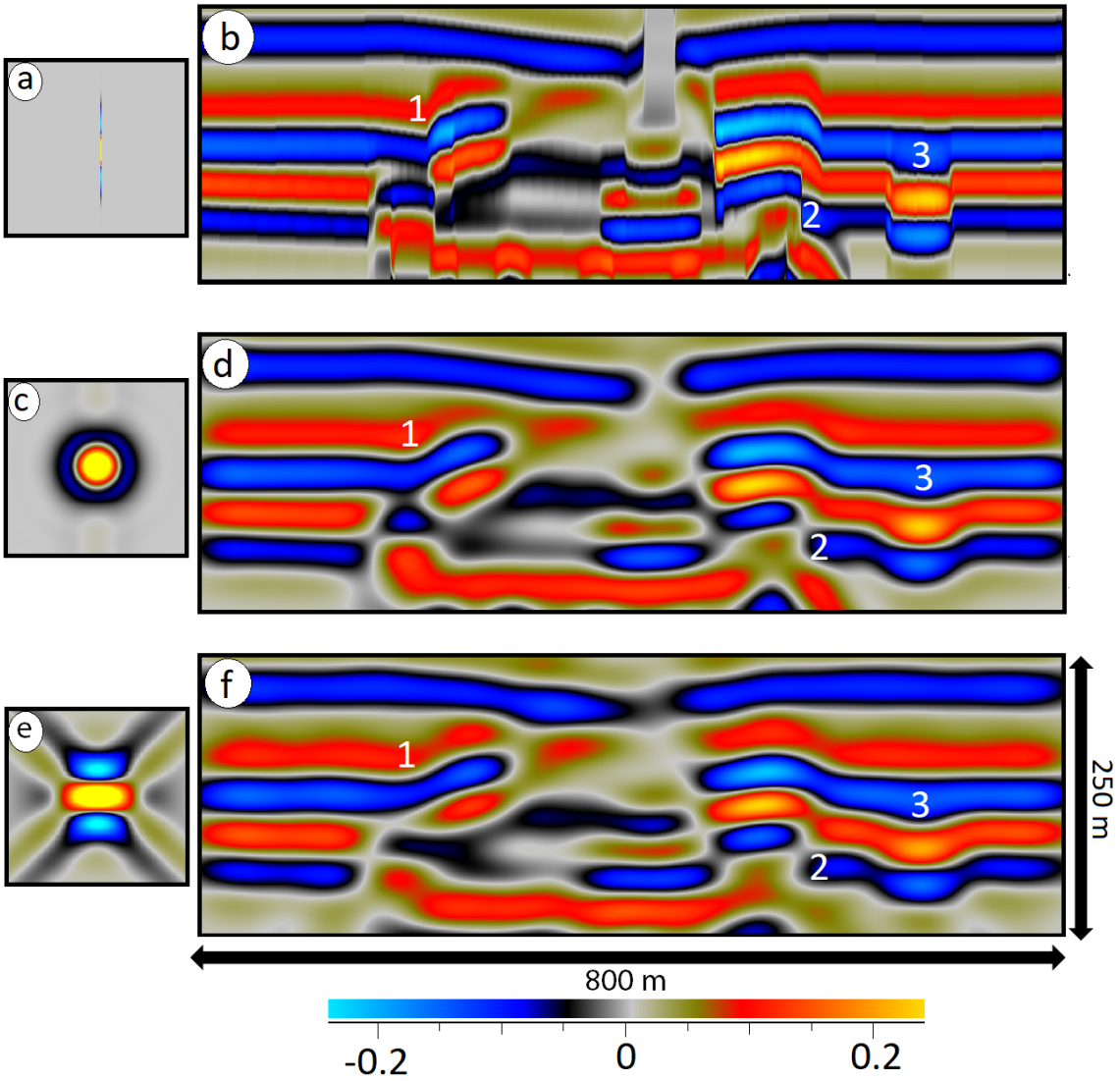

Figure 5.5: *The main body of the GMS and the adjacent cave modelled with ab: 1D convolution, cd: perfect illumination PSF, ef: 45° max-dip PSF, reference points 1,2,3 marked. PSFs in a,c,e, not calibrated.*

It is important to remember that all these seismic modelling cases are made with exactly the same parameters, the only differences are the PSFs. This illustrates how significant the illumination and resolution effects of the PSFs are, and that they should not be neglected.

5.2.3 Beckwith Plateau outcrop

Modelling an outcrop at the Beckwith Plateau with thin silt layers revealed that the 1D convolution method generated discontinuous seismic at complex areas with swift changes in amplitude or depth, whereas the 2D PSF-based PSFs generated a seismic with smoother layers and transitions between those layers. Due to the relatively small-scale size of the silt layers and low-frequency wavelets in the seismic, the layers are not visible in the seismic for any of the modelling methods. Therefore, difference plots were made, highlighting the difference caused by the silt layers. For the 1D convolution modelling method, the results revealed that the seismic would be more uneven in the two areas of dipping layers. In the PSF-based seismic, there is no significant differences in the dipping layers compared to the horizontal ones.

This raises the question whether the effect of the silt layers lies in how the effective, average velocity (or density) in the blocks which encapsulates the layers alters, or the shape of the structures. If the former is the case, the seismic is not affected by the shape of the layers, and what I am studying is not the difference in the seismic caused by the shape, but the difference in effective properties for the whole block, which only depends on the size of the silt layers. An argument for this case that we cannot observe in the difference plots if the layers are dipping or horizontal.

However, studying the results in the 1D convolution case, Figure 4.28.c, Figure 4.31.c, compiled in Figure 5.6 and Figure 5.7, I found variations in the seismic between the horizontal and dipping layers. It seems that the seismic is much more jagged for areas with dipping layers than in locations with horizontal layers. Based on this evidence, I believe that the shape of the small silt layers are influencing the seismic. If we say that this is the case, the figures studied in Section 4.5, shows that the dipping layers causes jagged edges in the 1D convolution, which is not present in seismic generated by the 2D convolution modelling method, and thus the shape of the silt layers have an effect on the seismic.

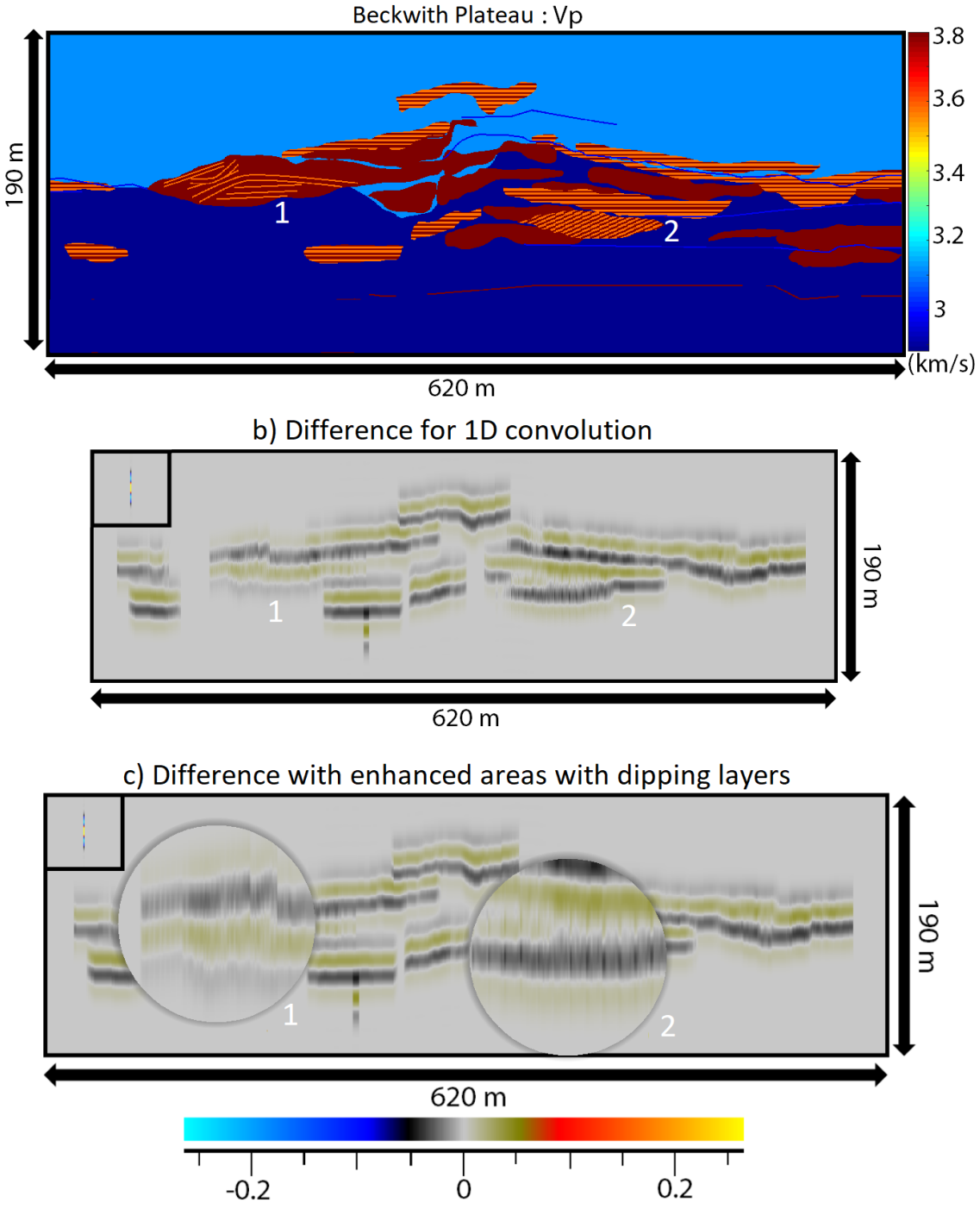

Figure 5.6: *The differences caused by the silt layers. (a) The P-velocities of the model, where the silt layers are visible, Vp=3.58 km/s, orange. Location of dipping layers marked as 1 and 2. (b) The differences in seismic caused by the silt layers. (c) Enhanced the locations of dipping layers in the difference plot.*

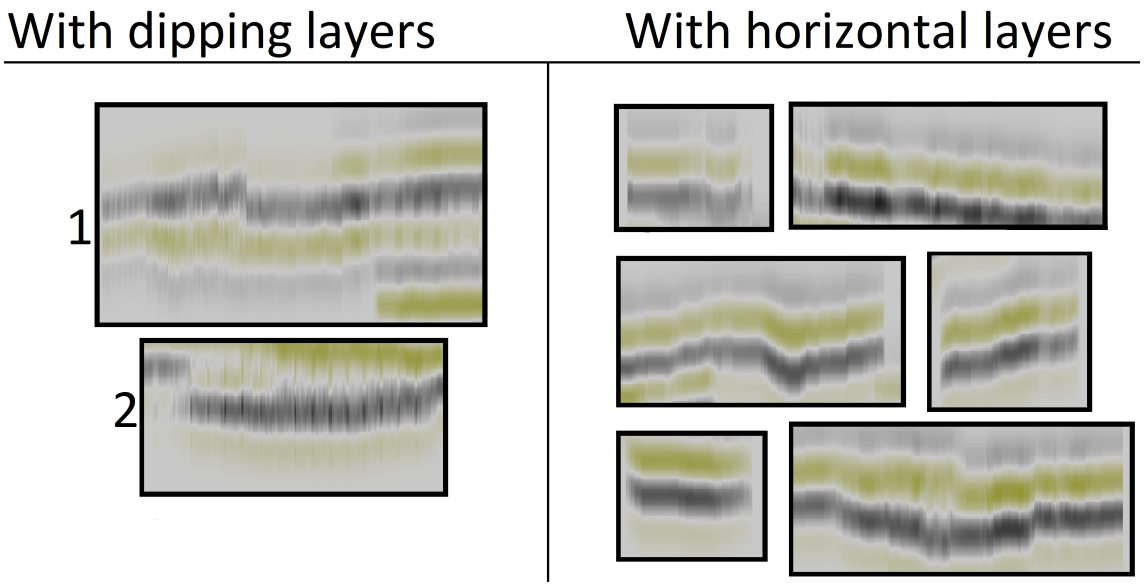

Figure 5.7: *Enhanced several locations in the difference plot for the 1D convolution. Split into two categories: Locations 1 and 2 in the section with dipping layers, most of the horizontally layered in the section with horizontal layers.*

Whether the silt layers are detected individually or not, the difference plots show that there is a change in amplitude values due to the silt layers, which means that they do have an impact. This could be interesting to model with an AVO survey, to study how the amplitudes in the dipping layers would compare to the horizontal layers.

The Beckwith Plateau outcrop also proved to be an interesting area to model, without only studying differences caused by thin silt layers. Due to its complex area, there were several differences in the seismic after modelling with 1D and 2D convolution; these differences were discussed in Section 4.5. If I had chosen a coarser sampling than 50 cm, the differences in the outcrop would have been even more eye-catching, but with a fine sampling, the smaller effects of the silt layers could be studied.

5.2.4 Setergrotta

For the final model, I did 3D modelling with data from Setergrotta. This enabled me to study resolution effects across layers in all three directions with 3D PSFs, Figure 5.8, and I found significant differences between the results of the modelling methods, especially when studying horizontal slices, Figure 5.9. Already due to the vertical

resolution effects, effects from several reflectors are added together at the slice we interpret. This causes the lateral resolution effects of each reflector to be added together with nearby reflectors, and thus have a magnified effect, which results in significant differences between the seismic of the modelling methods.

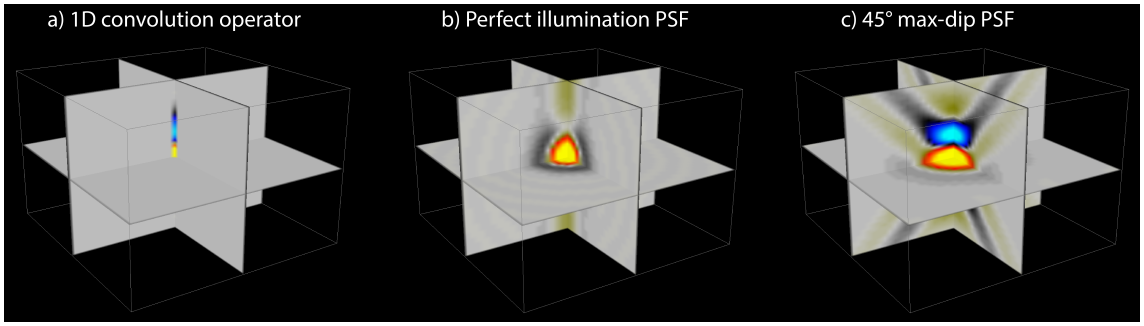

Figure 5.8: *3D view of the 30 Hz Ricker generated PSFs used in the Setergrotta modelling case. (a) 1D convolution operator, ''PSF", (b) perfect illumination PSF and (c) 45° max-dip PSF.*

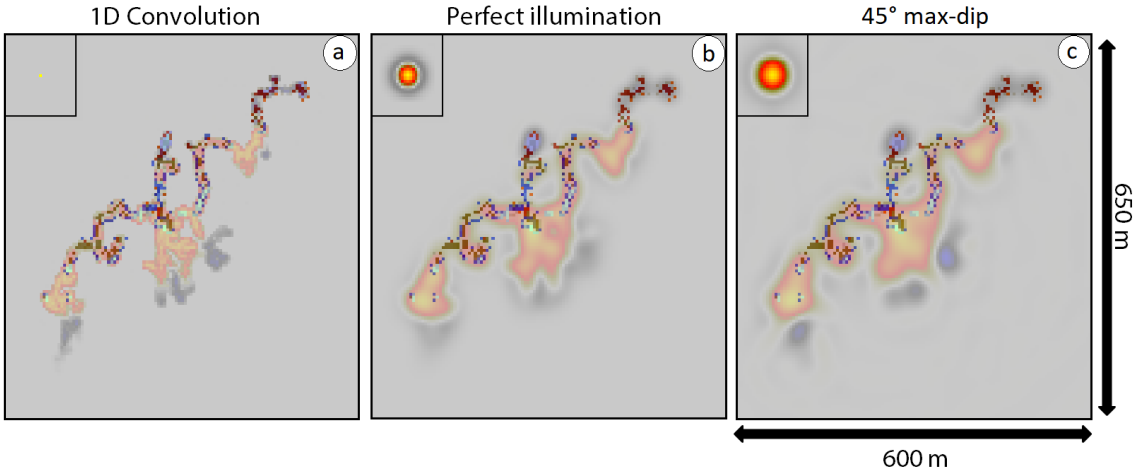

Figure 5.9: *The seismic as seen from above compared with the reflection events. (a)1D convolution, (b) Perfect illumination PSF (c) 45° max-dip PSF, not calibrated.*

The lack of lateral resolution effects in the 1D convolution modelling causes the seismic in the horizontal slices of the Setergrotta model to be unsatisfactory. With a false lateral resolution of 1 pixel the seismic is merely a map of the locations of

reflection coefficients throughout the model, while the 3D PSF-based ones generate more realistic seismic slices. As illustrated in Figure 4.35, the lateral resolution effects for the 45° max-dip PSF is twice of the from perfect illumination PSF. The lateral smearing in the PSF-generated modelling cases, Figure **??**.b.c, illustrates the effect of full 3D resolution for a 3D convolution compared with the 1D resolution for the 1D convolution, Figure 5.9.a.

5.3 Convolution modelling in practice

One advantage the 1D convolution method has over the PSF-based method is the computation speed. For each 2D model in this thesis, the modelling was done in a matter of seconds, regardless of method. After timing the 3D Setergrotta modelling method with three wavelets, 30 Hz, 50 Hz and 80 Hz Ricker wavelets, the two latter being relatively high frequencies, the difference between 1D and 3D convolution modelling was 6 seconds. This is for the most complex model I worked with, which shows that the 3D modelling method is almost as rapid as the 1D case for these models.

However, the 1D used in this thesis is not the classical 1D time-based one, which loops trace per trace. It is a depth-adapted one, which uses a 2D PSF with only one central trace which is a function of the average velocity. The code runs it the same way as a full 2D PSF, i.e., the "1D PSF" is applied at once to all traces. A pure repeated 1D convolution would be more efficient, but the run costs are still low.

I also wanted to time a modelling of a larger outcrop. In this thesis I used some outcrops from The Beckwith Plateau (Figure 1.1 and Figure 4.23). This is a part of a larger 5300 m long and 380 m high 3D outcrop. I modelled this outcrop with a 20 Hz, 30 Hz, 50 Hz and 100 Hz Ricker wavelet and 25 cm sampling in each direction to compare the time of a 1D convolution and the PSF-based convolution modelling. The results were 10 minutes, 26 seconds for the 1D and 11 minutes, 52 seconds for the PSF-based. A difference of 86 seconds using a 64 GB RAM workspace computer. This is low CPU time-costs, and far from what is needed for a complete modelling and processing, and the extra time-cost for a 2(3)D convolution modelling method is not significant.

One could argue that despite the many features of the 2(3)D convolution modelling method, and drawbacks of the 1D convolution modelling method, the 1D convolution is easier to use. However, both methods use a reflectivity model and a chosen wavelet as input, in addition to the average velocity of the velocity model to generate a survey-independent PSF in NORSAR SeisRoX. In fact, the process of generating a PSF-based convolution model is nearly as user-friendly as a 1D convolution, with possibilities to generate more advanced models if desirable.

Discarding the lateral resolution effects in seismic modelling leaves a hole in our knowledge about seismic imaging. Take the oil industry as an example, where if we drill for an oil reservoir, but due to a misjudgement drill at a wrong depth and/or lateral location, it will cost extra to drill further than planned or deviate the well. This is an example of why a modelling with complete resolution effects is so important. Another case could be if we misjudge the location of the reservoir, and miss the whole reservoir. To then either start drilling in another direction, or to abandon the well, and start drilling in another location is very expensive. This could be the result if we base the interpretation of a seismic image on results from a seismic model without lateral resolution effects.

Chapter 6

Conclusion

In this study, the main objective has been to examine the effects that lateral resolution and limited illumination have on 2D and 3D PSDM seismic images using a 2(3)D convolution method. I used 1D convolution to model the vertical resolution effects alone, a perfect illumination PSF to model with lateral resolution effects in the case of a perfectly illuminated target, and 45° max-dip to simulate a limited illumination, i.e., about equivalent to what a good 3D seismic would perform. This was done for four modelling cases; a steep wedge model, the Franklin Mountains outcrop, which is a 2D high-velocity paleo cave, a 2D complex outcrop at the Beckwith Plateau, and finally a 3D model from an actual cave, Setergrotta. After these modelling cases, my conclusions are as following:

- Introducing lateral resolution effects into the wedge model alters also its vertical resolution compared to 1D convolution, thereby increasing the tuning thickness compared to standard knowledge. These results indicate that the vertical and lateral resolution are not two independent entities. Therefore, I would move towards 2(3)D convolution modelling to include lateral resolution with a similar time-cost.
- In the 2D modelling cases of the Franklin Mountains and Beckwith Plateau, the added lateral resolution removed the artefacts at steep structures generated by 1D convolution, such as fault-like jagged edges and apparent thinning. These models also illustrated how the limited illumination causes smearing in the seismic due to an increase in lateral resolution effects.
- The 3D Setergrotta modelling case highlights the differences lateral resolution effects make on a 3D model. This is where the 1D convolution results were the most lacklustre, with significant differences in the horizontal slices. In a 3D model, the resolution and illumination effects introduced by the 2(3)D modelling method yield a significant difference from the 1D convolution modelling.

- As the aim of seismic modelling is to generate modelling cases with the highest degree of realism possible, I would highly recommend moving away from the 1D convolution modelling method, and towards 2(3)D PSF-based convolution modelling. The 1D convolution modelling has too many drawbacks to be a realistic cost-effective alternative to FD-modelling; it does not take into account illumination effects, survey effects, or lateral resolution effects. This causes a highly simplified modelling which does not reflect the state-of-the-art computer power or imaging techniques available today.

Chapter 7

Future work

When modelling, I had several ideas which could be interesting to pursue to further study resolution and illumination effects, and help seismic interpreters understand the importance of 2(3)D modelling:

- Further model with different wavelets. I mainly did my modelling with a 30 Hz Ricker wavelet, but it would be interesting to further study the effects of side lobes, e.g., using an Ormsby wavelet with less side lobes.
- It is intuitive for a first-time modeller to want a seismic result which resembles as close as possible the reflectivity model, without the complications of a real seismic image. However, to better appreciate the impact of the 2(3)D convolution modelling method, it would be beneficial to compare it to real PSDM images, which would also help readers understand the benefits of seismic modelling.
- It would be interesting to model AVO effects, as I assume that there would be significant differences in amplitude values in the steep complex structures, including the dipping silt layers of the Beckwith Plateau. This would especially be interesting with illumination limited seismic.
- I spent a significant amount of my time during this work performing amplitude calibration on every model, where there is room for human error. A solution to this could be to implement amplitude calibration in the PSF-generating code, which would be very beneficial for future modellers.
- As I found that the lateral resolution effects influence the vertical resolution of seismic, I would have liked to do a more systematic modelling of wedge models with various dipping angles, frequencies and illumination limitations to find more systematic relations between lateral and vertical resolution.

Bibliography

Carcione, J., Herman, G., and ten Kroode, A. (2002). Seismic modeling. *GEOPHYSICS*, 67(4):1304–1325.

Eide, C. H., Schofield, N., Lecomte, I., Buckley, S. J., and Howell, J. A. (2017). Seismic interpretation of sill complexes in sedimentary basins: implications for the sub-sill imaging problem. *Journal of the Geological Society*, 175(2):193–209.

Červený, V., Molotkov, I. A., and Pšenčík, I. (1977). *Ray method in seismology*. Univerzita Karlova.

Etgen, J. T. and Kumar, C. (2012). What really is the difference between Time and Depth Migration? A tutorial. In *SEG Technical Program Expanded Abstracts 2012*, pages 1–5. Society of Exploration Geophysicists.

Flesland, M. (2017). Controls on architecture and seismic imaging of igneous intrusions: Examples from LIDAR outcrop data on Traill Ø (East Greenland) and seismic data from the conjugate Møre Margin. Master's thesis.

Fliedner, M. M. and White, R. S. (2003). Depth imaging of basalt flows in the faeroe–shetland basin. *Geophysical Journal International*, 152(2):353–371.

Friestad, E. (2018). Synthetic seismic modelling of fluvial channels in the blackhawk formation as an analog to the triassic barents sea, in press. Master's thesis, Department of Earth Science, University of Bergen.

Hampson, D. and Russell, B. (2013). Joint simultaneous inversion of PP and PS angle gathers. page 7.

He, Y., Zhu, J., Zhang, Y., Liu, A., and Pan, G. (2017). The Research and Application of Bright Spot Quantitative Interpretation in Deepwater Exploration. *Open Journal of Geology*, 07(04):588–601.

Herron, D. A. (2011). *First Steps in Seismic Interpretation*. Society of Exploration Geophysicists.

Huang, J., Gao, L., and Gao, Y. (2007). Side lobes of wavelets impact identification of thin sand bodies. *Applied Geophysics*, 4(2):111–117.

Johansen, M. (2018). A modelling workflow for seismic characterization of paleokarst reservoirs, in press. Master's thesis, Department of Earth Science, University of Bergen.

Kallweit, R. and Wood, L. (1982). The limits of resolution of zero-phase wavelets. *Geophysics*, 47(7):1035–1046.

Kanasewich, E. R. (1981). *Time Sequence Analysis in Geophysics*. University of Alberta.

Kearey, P., Brooks, M., and Hill, I. (2002). *An Introduction to Geophysical Exploration*. Wiley.

Klausen, T. G., Torland, J. A., Eide, C. H., Alaei, B., Olaussen, S., and Chiarella, D. (2017). Clinoform development and topset evolution in a mud-rich delta – the Middle Triassic Kobbe Formation, Norwegian Barents Sea. *Sedimentology*, 65(4):1132–1169.

Kumar, D. (2018). Seismic Amplitude Calibration for Quantitative Interpretation. *GEOS, G&G Alumni special, Indian Institute of Technology Kharagpur*.

Lecomte, I. (2008). Resolution and illumination analyses in PSDM: A ray-based approach. *The Leading Edge*, 27(5):650–663.

Lecomte, I., Lavadera, P., Anell, I., Buckley, S., Schmid, D., and Heeremans, M. (2015). Ray-based seismic modeling of geologic models: Understanding and analyzing seismic images efficiently. *Interpretation*, 3(4):SAC71–SAC89.

Lecomte, I., Lavadera, P. L., Botter, C., Anell, I., Buckley, S. J., Eide, C. H., Grippa, A., Mascolo, V., and Kjoberg, S. (2016). 2(3)D convolution modelling of complex geological targets beyond – 1d convolution. *First Break*, 34(5):99–107.

Lindsey, J. (1989). The Fresnel zone and its interpetive significance. *The Leading Edge*, 8(10):33–39.

Magee, C., Maharaj, S. M., Wrona, T., and Jackson, C. A.-L. (2015). Controls on the expression of igneous intrusions in seismic reflection data. *Geosphere*, 11(4):1024–1041.

Mark, N., Schofield, N., Gardiner, D., Holt, L., Grove, C., Watson, D., Alexander, A., and Poore, H. (2018). Overthickening of sedimentary sequences by igneous intrusions. *Journal of the Geological Society*, pages jgs2018–112.

Målbakken, T. (2009). Paleocaves and collapse breccias in the Franklin Mountains; implications for paleokarst reservoirs. Master's thesis, Department of Earth Science, University of Bergen.

Mussett, A. E., Khan, M. A., and Button, S. (2000). Looking into the Earth by Alan E. Mussett.

Pemberton, E., Stright, L., Fletcher, S., and Hubbard, S. (2018). The influence of stratigraphic architecture on seismic response: Reflectivity modeling of outcropping deepwater channel units. *Interpretation*, 6(3):T783–T808.

Ryan, H. (1994). Ricker, Ormsby, Klander, Butterworth – A Choice of Wavelets.

Sheriff, R. E. (1975). Factors Affecting Seismic Amplitudes*. *Geophysical Prospecting*, 23(1):125–138.

Sheriff, R. E. (2002). *Encyclopedic Dictionary of Applied Geophysics*. Geophysical References Series. Society of Exploration Geophysicists.

Sheriff, R. E. and Geldart, L. P. (1995). *Exploration seismology*. Cambridge university press.

Simm, R. and Bacon, M. (Michael), a. (2014). *Seismic amplitude : an interpreter's handbook*. Cambridge Cambridge University Press.

Sobel, I. and Feldman, G. (1968). A 3x3 isotropic gradient operator for image processing. *a talk at the Stanford Artificial Project in*, pages 271–272.

Thomson, K. and Hutton, D. (2004). Geometry and growth of sill complexes: insights using 3d seismic from the north rockall trough. *Bulletin of Volcanology*, 66(4):364–375.

Widess, M. (1973). How thin is a thin bed? *GEOPHYSICS*, 38(6):1176–1180.

Xu, C., Di, B., and Wei, J. (2016). A physical modeling study of seismic features of karst cave reservoirs in the tarim basin, china. *Geophysics*, 81(1):B31–B41.

Yilmaz, Ö. (2001). *Seismic data analysis: Processing, inversion, and interpretation of seismic data*. Society of exploration geophysicists.

Zeng, H., Wang, G., Janson, X., Loucks, R., Xia, Y., Xu, L., and Yuan, B. (2011). Characterizing seismic bright spots in deeply buried, ordovician paleokarst strata, central tabei uplift, tarim basin, western china. *Geophysics*, 76(4):B127–B137.

Zoeppritz, K. (1919). VII b. Über Reflexion und Durchgang seismischer Wellen durch Unstetigkeitsflächen. *Nachrichten von der Gesellschaft der Wissenschaften zu Göttingen, Mathematisch-Physikalische Klasse*, 1919(1):66–84.